IDEAL MHD STABILITY OF TOKAMAK PLASMAS WITH MODERATE AND LOW ASPECT RATIO

THÈSE N^O 3218 (2005)

PAR

Andrey MARTYNOV

ingénieur-physicien, Institut National d'Ingénierie et de Physique de Moscou, Russie
et de nationalité russe

Lausanne, EPFL
2005

Abstract

The need of durable and abundant energy sources for future ages stimulates the studies of thermonuclear energy sources, based on hot plasma confinement by magnetic fields. The most developed concept of hot plasma trap is the tokamak, where the plasma confinement is obtained by a combination of external magnetic fields with the magnetic field of the current flowing in the plasma torus. The stability of the tokamak plasma is the main subject of the present work.

The hot plasma is approximated by the model of the ideal magnetohydrodynamics (ideal MHD) as a superconductive liquid. Being relatively simple, this model describes basic plasma stability properties and establishes necessary stability conditions.

The analytical ideal MHD theory is well developed, but some assumptions, required for analytical treatment may not be valid for the plasmas of modern tokamaks and for future tokamak-based reactors. To circumvent this numerical codes have been created. These codes are free from such limitations, but they are not as convenient in use as analytical formulae. In the present work the validity of the analytical approach for the conditions of tokamaks like TCV and MAST is examined in comparison with numerical code predictions by studying the dependence of the ideal MHD stability on plasma toroidicity and shape parameters. The experimental study of the plasma dependence on triangularity, carried out on the TCV tokamak, is consistent with the results of the numerical calculations. A new formula, describing the ideal MHD stability dependence on plasma toroidicity and shape parameters is proposed for use in modern tokamaks and future reactors. This formula could be used instead of analytical expansions, which are not valid in such conditions.

The ideal MHD stability of highly elongated TCV plasmas has been studied using numerical codes and the optimum plasma shape, which allows higher plasma performance, was found. Experimental data on the high elongation plasmas in TCV are consistent with the numerical predictions.

Advanced tokamak plasma configurations, which provide better plasma properties, are amongst the main goals of the TCV tokamak research activity. The ideal MHD stability analysis of such plasmas, using numerical codes, can be useful for optimization of plasma parameters, and designing new experiments with improved plasma performance. Reversed shear plasmas with internal transport barrier were analyzed and the influence of the plasma pressure and current profiles on the ideal MHD stability of these plasmas was examined in detail. By fine tuning of the electron cyclotron heating and current drive system of TCV it was found that it might be possible to improve the plasma performance in reversed shear plasmas, by creating the optimal current and pressure profiles.

Version abrégée

La nécessité de trouver des sources d'énergie durables et abondantes pour les siècles à venir stimule les recherches sur les sources d'énergie thermonucléaire, basées sur le confinement du plasma chaud dans un champ magnétique. Le concept le plus developpé est le tokamak, où le confinement du plasma est obtenu par une combinaison des champs magnétiques externes avec un champ magnétique dû au courant circulant dans le plasma toroïdal. La stabilité de plasma du tokamak est le sujet principal de ce travail.

Dans le modèle de la magnétohydrodynamique idéale (la MHD idéale) le plasma chaud est modelisé par un liquide supraconducteur. Relativement simple, ce modèle décrit les propriétés de base de la stabilité du plasma et établit les conditions nécessaires de stabilité.

La théorie analytique de la MHD idéale est bien developpée, mais certaines approximations, requises pour le traitement analytique, peuvent ne pas être valides pour les plasmas des tokamaks modernes et pour les réacteurs futurs basés sur le concept du tokamak. Pour circonvenir ces obstacles, les codes numériques ont été créés. Ces codes sont libres de ces limitations, mais ils ne sont pas aussi pratiques que les formules analytiques. Dans ce travail la validité de l'approche analytique dans les conditions des tokamaks comme TCV et MAST est examinée et comparée avec les codes numériques par une étude de la dépendance de la stabilité MHD idéale sur la toroidicite et les paramètres de forme du plasma. L'étude expérimentale de la dépendance du plasma sur la triangularité sur le tokamak TCV, correspond aux résultats des calculs numériques. Une nouvelle formule qui décrit la stabilité MHD idéale est proposée pour l'utilisation dans les tokamaks modernes et dans les réacteurs futurs. Cette formule peut être utilisée à la place des développements analytiques, non valides dans ces conditions.

La stabilité MHD idéale des plasmas à haute élongation sur le TCV a été étudiée avec des codes numériques, et la forme optimale permettant la meilleure performance stable du plasma a été trouvé. Les données expérimentales sur les hautes élongations sur le TCV sont en accord avec ces prédictions.

Les scénarios avancés dans les tokamaks, générant des meilleures propriétés du plasma, sont parmi les objectifs majeurs de l'activité expérimentale de TCV. L'analyse de la stabilité MHD idéale de ces plasmas peut être utile pour l'optimisation des paramètres du plasma et pour l'élaboration de nouvelles expériences plus performantes. Les plasmas avec cisaillement renversé avec une barrière du transport interne ont été analysés en détails. En ajustant le système du chauffage et la génération du courant par les ondes cyclotroniques électroniques du TCV, on peut améliorer la performance du plasma par création de profils optimaux de la densité de courant et de la pression.

Table of contents

Chapter 1. Introduction

1.1 The thermonuclear fusion: why a hot plasma in magnetic fields?

Successful control of thermonuclear fusion could provide the amounts of energy required for the future development of mankind for many centuries. Using the unlimited reserves of ocean water as the fuel, producing much less radioactive waste than the conventional fusion powered reactors, and zero emission of polluting and greenhouse gases, thermonuclear power stations could become the basis of the energy producing industry of the future, along with renewable energy sources.

The idea of thermonuclear fusion is based on the nuclear reaction between nuclei of light elements (isotopes of hydrogen and helium) which by collisions can form a single nucleus of a heavier element and release a substantial amount of energy. The most promising reaction of this type involves two nuclei of hydrogen isotopes, one of Deuterium (D) and one of Tritium (T). As a result of their collision, a nucleus of Helium can be formed and some 17.6 MeV of energy produced. The temperatures of the initial Deuterium-Tritium fuel mixture has to be at least around 10 keV to maximize the probability of undergoing such reactions and the density has to be high enough to provide the amount of released energy required for the sustainment of the plasma temperature (so-called ignition). At such temperatures the fuel is no more solid or liquid, it becomes a highly ionized gas, called plasma. It is extremely difficult to confine and control such matter in terrestrial conditions. In order to obtain the required number of fusion reactions to keep the plasma "burning", the thermonuclear reactor has to be able to confine sufficient amount of particles of high energy inside the plasma to allow them to react. Formally, this requirement of keeping high temperature and density is expressed by the Lawson criterion [1],

$$n\tau_E > 10^{21}\,\mathrm{m}^{-3}\mathrm{s} \tag{1.1}$$

where n is the plasma density in $[\mathrm{m}^{-3}]$ and τ_E is the energy confinement time in seconds (D-T reaction at the temperature of 20 keV).

Such a hot plasma confined in conventional materials will almost immediately loose all its energy and disappear, because the losses of energy and of particles will be enormous. It is only possible to deal with such matter by placing it in some kind of trap, constructed in a way that provides simultaneously the confinement of plasma and its thermal insulation. Since a small contact with solid matter can cause substantial losses of energy or destabilization and destruction of the plasma, a promising way of creating such conditions is based on the use of magnetic fields.

For this reason since the early 1950s, much effort was concentrated on the design and creation of such magnetic field configurations. After many years, two concepts are considered now as being the most prominent ones for the creation of a magnetically confined thermonuclear reactor: the tokamak (artificial word, abbreviation of the Russian phrase "Toroidal'naja Kamera s Magnitnymi Katushkami", meaning "Toroidal Chamber with Magnetic Coils"), which involves the magnetic field of the plasma current, flowing inside the plasma tore, and secondly the stellarator ("Stella", the star in Latin), where complicated shapes of magnetic coils are required to create the effective magnetic trap. The first experimental thermonuclear reactor, ITER, is based on the tokamak concept [2].

The Lawson criterion involves two basic parameters: the plasma density and the energy confinement time. The energy confinement time is mostly determined by the microscopic phenomena that occur in the plasma, i.e. by collisions and microinstabilities that are usually treated by kinetic models. The plasma density depends essentially on macroscopic equilibrium; the highest achievable density at a given temperature is determined by the stability limits that are set by the magnetic geometry. Fluid models are most relevant here and the model of ideal magnetohydrodynamics is of particular interest. Ideal magnetohydrodynamics (ideal MHD) is one of the most developed and useful models, combining the relative simplicity with a wide range of validity. Ideal MHD describes the stability limits, determined by magnetic energy, thermal pressure and inertial forces in a perfectly conducting plasma placed in an arbitrary magnetic configuration. The past years of experiments show that the magnetic configuration has at least to fulfill the restrictions set by ideal MHD to confine successfully the plasma, i.e. ideal MHD is a necessary but not sufficient test of the stability properties of the plasma configuration. The phenomena that are not described by ideal MHD only make the restrictions more rigorous. Non-ideal effects, not included in the ideal MHD model, for example finite plasma resistivity, can cause instabilities that are weaker than ideal ones, but present in ideally stable conditions. Such non-ideal instabilities can deteriorate the plasma confinement or even lead to plasma disruption. Hence another important direction of plasma physics is the development of models describing the influence of these non-ideal effects.

Ideal MHD is used presently as a general tool for the search of ways to optimize and improve magnetic trap configurations. If analytical solutions are available, they can be analyzed and the main parameters that can influence the macroscopic plasma stability can be easily found. Unfortunately, being simple in comparison with many other more elaborated theories, the model of ideal MHD is still difficult to deal with analytical solutions for the many magnetic geometries of practical interest. Moreover, the basic analytical approach, using expansions of the ideal MHD equations, is not necessarily valid for the conditions of the many modern experimental devices, because some parameters that are considered small, are not presently small any more (for example, the inverse aspect ratio ε, determined by the ratio of the minor radius of the torus to the major radius). In such cases,

numerical codes, solving the ideal MHD equilibria and stability problems for the given magnetic configurations should be used.

1.2 A short history of the MHD theory

The early concepts that can be considered as the precursors of the MHD theory appeared in the XIXth century. The famous British scientist Michael Faraday has carried out the first experiment that can be related to the MHD domain: he tried to measure the current, generated by the dynamo effect, caused by the magnetic field of Earth in the flowing water of the Thames river under the Waterloo bridge in London [3]. Unfortunately, the generated voltage was too small to be measured.

Apart from these early experiments, MHD theory has its roots in the first decades of the XXth century. Larmor supposed in 1919 that the Earth's magnetic field was generated by dynamo action within the liquid-metal of its core and Hartmann started serious studies of the behavior of the mercury in the magnetic field. In 1918 he invented the electromagnetic pump, working on principles of what he called "Hg-dynamics".

Further studies of the behavior of conducting liquids and gases in electric and magnetic fields are associated with the name of Hannes Alfvén (1908 – 1995), who has put the basis of the modern MHD theory. The proof of the possibility of propagation of electromagnetic waves in highly conducting mediums, the theory of hydromagnetic waves, called now Alfvén waves (1942), the concept of the guiding-center approximation for the motion of charged particles in electric and magnetic fields and the concept of frozen-in magnetic flux are among his achievements. The Nobel Prize in Physics in 1970 for these "contributions and fundamental discoveries in magnetohydrodynamics" was a well deserved recognition of his talent.

Until 1940, MHD theory was developed with regards to astrophysical objects like space magnetic fields, radiation belts, etc. The studies of thermonuclear fusion that begun intensively in the late 1940s gave a strong impact to the MHD theory, because the thermonuclear plasma is a unique object, where MHD theory can be implemented and where experiments can be made. The basic outlines of ideal MHD theory in its implementation to the hot thermonuclear plasmas were formulated towards 1960: the concept of the MHD equilibrium [4, 5] of magnetic traps, the concept of the Energy Principle [6, 7], basic types of ideal instabilities etc. Ideal MHD theory developed further in the ways of creation of more complicated models. In addition to the analytical approach, based on the expansion of the MHD equations on some small parameters, computer codes are widely used, allowing numerical solutions to the problems without assuming the smallness of these parameters.

Ideal MHD theory describes only a limited number of physical effects arising in thermonuclear plasmas. Other theories have been developed, partially on the basis of the ideal MHD, the resistive

MHD for example. Nevertheless, ideal MHD theory is still under development and its applications are far from being completed.

1.3 The motivation and the goals of the present work

Ideal MHD studies are used extensively, in particular for the design of new experiments, like the ITER-FEAT experiments [2]. It was also used to design the TCV experiment almost 20 years ago [8]. These studies are useful because ideal MHD is known to set the maximum achievable beta value that can be reached for given current and pressure profiles, and given plasma boundary shape. The actual beta values reached in present experiments are often below the ideal limit. This is sometimes because of the lack of heating power, sometimes because of non-ideal MHD effects and sometimes because the ideal limit is lower than expected. However there has never been a systematic study of the relevance of ideal MHD calculations for the present TCV experiments. This is useful first to qualify if the design studies had some predictive merits. It is also useful to understand the present unstable modes which limits the TCV performances. Finally it is useful to know when ideal MHD cannot explain the measurements and non-ideal effects need to be included.

The main study relates to the internal kink mode, which is responsible for periodic relaxations of the central temperature and current profile (see [9] and references therein). This cause for the trigger of this mode is also important because it can also destabilize other modes, in particular the neoclassical tearing modes [10], which can degrade the overall plasma performance [11]. The internal kink has been studied extensively, in particular with analytical work [for example in 12, 13, 14, 15, 16]. However the numerical analyses have not been systematic, in particular concerning the dependence on shaping parameters. This is why we have calculated numerically the growth rate of the internal kink mode for a wide variety of plasma elongation, triangularity and aspect ratio. We also compare with analytical results and show that they are not always applicable for present tokamak parameters. This is why we also propose a formula which is obtained by fitting the numerical results, in order to help rapid evaluation of the internal kink growth rate.

We have also calculated the effects of higher order change in the plasma shape on the external kink mode stability at high elongation. This was required because TCV experiments have shown that it is difficult to find stable plasmas for elongations larger than about 2.2-2.4. Such results are in agreement with the design studies [8]. The analysis of the current limit of highly elongated plasmas varying the triangularity and squareness has enabled the development of optimised shapes. This has allowed TCV to reach elongation of 2.8 and a normalized current of 3.9 [MA/mT]. This study confirms the predictive capabilities of ideal MHD.

Finally an important subject of experimental studies in TCV deal with advanced scenarios. These scenarios are related to obtaining internal transport barriers capable of improving both the energy and

particle confinement properties [17, 18]. These scenarios, in particular on TCV, are related to non-monotonic current density profiles [19, 20, 21, 22 and references therein]. Such scenarios are known as reversed shear plasmas. It is known that such current profiles significantly change the ideal beta limit properties [for example 23, 24, 25]. However no systematic studies of the ideal limit of TCV advanced scenarios have been performed so far. The present work has analysed specific TCV discharges and shows that the observed disruptions are due to the ideal beta limit. In addition we have analysed the variation of the beta limit on the value and position of the minimum safety factor, the pressure gradient and the total current in order to describe the expected operational domain of TCV experiments with internal transport barriers. This study is also of interest to the many tokamaks which develop plasmas with non-monotonic current density. The latter is required in order to develop steady-state scenarios for fusion tokamaks [17, 18].

1.4 The organization of the work

The present work is organized in the following way.

Chapter 2 describes the ideal MHD model, its basic assumptions, validity, main methods of analytical analysis and their applications. The tokamak equilibrium and some results on the ideal MHD stability of the tokamak plasmas are presented with the emphasis on the internal kink mode stability. The analytical expansions that consider the plasma shaping are given and the roles of various terms are discussed.

Chapter 3 is devoted to the numerical calculations of the MHD stability and to the MHD stability code KINX. The calculations schemes that were used are also discussed.

Chapter 4 describes the results obtained for the ideal internal kink stability, including the analytical and numerical studies along with the experimental TCV data on the plasma shape variations.

The theoretical and experimental results are compared and an approximative scaling for the ideal internal kink growth rate based on the numerical results is presented.

Chapter 5 presents the contribution of the ideal MHD calculations for various shapes and very high elongations to the analysis and optimization of TCV experiments.

Chapter 6 presents the TCV experiments with internal transport barrier and non-monotonic current density profiles and it is shown that the profiles at the disruption are consistent with the ideal MHD limit. The dependence of the ideal MHD limit of these scenarios on the position of the barrier (maximum plasma pressure gradient) and of the minimum safety factor is also presented.

The summary and conclusions are presented in the Chapter 7.

Chapter 2. The linear ideal MHD model

The ideal MHD model is presented in this chapter along with the basic predictions of this model on the ideal internal and external mode stability in tokamaks. The MHD system of equations is obtained by neglecting the electron inertia in the collision dominated plasma, thus providing the single fluid description of the plasma. Using the ideal MHD equations, it is possible to identify the major stability qualities of different types of plasma configurations, from purely abstract and simple models to more complicated ones, close to real experimental plasmas.

2.1 Ideal MHD: formulation, assumptions, validity

The equations that form the basis of the ideal MHD are given by the continuity equation, the momentum equation, the equation of state and the Maxwell equations:

$$\frac{\partial \rho}{\partial t} + \nabla \cdot \rho \mathbf{v} = 0 \tag{2.1}$$

$$\rho \frac{d\mathbf{v}}{dt} = \mathbf{J} \times \mathbf{B} - \nabla p \tag{2.2}$$

$$\frac{d}{dt}\left(\frac{p}{\rho^{\Gamma}}\right) = 0 \tag{2.3}$$

$$\mathbf{E} + \mathbf{v} \times \mathbf{B} = 0 \tag{2.4}$$

$$\nabla \times \mathbf{E} = -\frac{\partial \mathbf{B}}{\partial t} \tag{2.5}$$

$$\nabla \times \mathbf{B} = \mu_0 \mathbf{J} \tag{2.6}$$

$$\nabla \cdot \mathbf{B} = 0 \tag{2.7}$$

where $\mathbf{E}$ is the electric field, $\mathbf{B}$ the magnetic field, $\mathbf{J}$ the current density, ρ the mass density, $\mathbf{v}$ the fluid velocity, p the pressure, $\Gamma = 5/3$ and $d/dt = \partial/\partial t + \mathbf{v} \cdot \nabla$ is the convective derivative.

This system of equations can be derived from the Maxwell equations and the general kinetic Boltzmann equations. The full derivation of the MHD equations itself is not the matter of the present work. It can be found for example in [26]. Nevertheless it is useful to list the assumptions, relevant to the MHD equations:

- The plasma is fully ionized and consists of negative electrons and positive ions of hydrogen or isotopes (H, D, T);

- The low-frequency limit of Maxwell equations is considered, formally by letting $\varepsilon_0 \to 0$.

Thus the displacement current $\varepsilon_0\, \partial\mathbf{E}/\partial t$ and the net charge $\varepsilon_0\, \nabla\cdot\mathbf{E}$ are neglected. As a result, the phase velocities of electromagnetic waves have to be much slower than the speed of light, $\omega/k \ll c$ and the characteristic thermal velocities are limited to non-relativistic velocities, V_{Te}, $V_{Ti} \ll c$, $V_{T\alpha} \equiv (2T_\alpha/m_\alpha)^{1/2}$. The plasma is considered quasineutral

$$n_i = n_e \equiv n \tag{2.8}$$

This requires that the macroscopic charge separation that can develop in the low-frequency phenomena is rapidly compensated by electrons, keeping the plasma in local quasineutrality.

- The electron inertia is neglected formally by letting $m_e \to 0$ in the Maxwell equations. To satisfy this condition, the consideration is limited to frequencies smaller than the electron plasma frequency, $\omega_{pe} = (n_0 e^2/m_e\varepsilon_0)^{1/2}$ and the electron cyclotron frequency, $\omega_{ce} = e\mathbf{B}/m_e$ and to the scale lengths longer than the Debye length $\lambda_D = V_{Te}/\omega_{pe}$ and the electron Larmor radius, $r_{Le} = V_{Te}/\omega_{ce}$.

- The plasma is considered as a single fluid by the following formal procedures:
  - As the mass of electrons is neglected, the mass density of the single fluid becomes

$$\rho = m_i n \tag{2.9}$$

  - The momentum of the fluid is carried by the ions, so that the fluid velocity $\mathbf{v}$ corresponds to the ion velocity $\mathbf{v_i}$.
  - The current density is proportional to the difference in velocity between electrons and ions:

$$\mathbf{J} = en\,(\mathbf{v_i} - \mathbf{v_e}) \tag{2.10}$$

  - The total plasma pressure and temperature are defined as follows:

$$p = nT = p_e + p_i \tag{2.11}$$

$$T = T_e + T_i \tag{2.12}$$

- The plasma is dominated by collisions. This means that the electron and ion distribution functions are nearly Maxwellian and the pressure is isotropic. It is important to mention that this condition is sufficient for creating a closed system of equations and no other assumptions about the character of collisions is required for that. To satisfy this condition, the considerations have to be limited to macroscopic phenomena, where the characteristic times have to be sufficiently long to allow the collisions to make the distribution function nearly Maxwellian and whose characteristic lengths have to be longer than the mean free path of the plasma particles. This can be expressed as follows:

$$\omega\tau_{ii} \sim V_{Ti}\tau_{ii}/a \ll 1 \tag{2.13}$$

$$\omega\tau_{ee} \sim (m_e/m_i)^{1/2} V_{Ti}\tau_{ii}/a \ll 1 \tag{2.14}$$

where τ_{ii} is the ion-ion collision time, $\tau_{ee} \sim (m_e/m_i)^{1/2}\tau_{ii}$, at $T_e \sim T_i$, is the electron-electron collision time, $\omega \sim V_{Ti}/a$ is the characteristic frequency of the MHD phenomena, a is the characteristic plasma dimension. Since $(m_e/m_i)^{1/2} \ll 1$, it is clear that (2.14) is fulfilled if (2.13) is satisfied.

- Ideal Ohm's law has to be satisfied. This implies that:

  - the MHD frequencies are considered much slower than the ion gyro-frequency, or, similarly, the ion Larmor radius is much smaller than the macroscopic plasma dimension:

$$\omega/\omega_{ci} \sim r_{Li}/a \ll 1; \tag{2.15}$$

  - the macroscopic plasma dimension a is large enough and the resistive diffusion time is long compared to the characteristic MHD time, this implies that

$$\frac{(m_e/m_i)^{1/2}}{\omega\tau_{ii}}(\frac{r_{Li}}{a})^2 \ll 1 \tag{2.16}$$

- The energy equilibration time has to be longer than the momentum exchange time, implying that

$$\left(\frac{m_i}{m_e}\right)^{1/2}\frac{V_{Ti}\tau_{ii}}{a} \ll 1 \tag{2.17}$$

The assumptions required for the formulation of the ideal MHD equations define the formal validity range of the ideal MHD model. Generally speaking, they lead to three basic requirements:

- high collisionality;
- characteristic plasma size much greater than the ion Larmor radius;
- large plasma size, so that resistive diffusion is negligible.

These requirements are restrictive, and they are not fulfilled in all achievable plasmas. Let us consider the fusion plasmas that represent the greatest interest. The formal MHD validity conditions for deuterium plasma, formulated in terms of the density n and temperature T, ratio of plasma pressure to magnetic pressure $\beta_t \equiv 2\mu_0 nT/B^2$ and plasma size a are given by:

$$3.0 \times 10^3 \ (T^2/an) \ll 1$$
$$2.3 \times 10^{-2} \ (\beta_t/na^2)^{1/2} \ll 1 \qquad (2.18)$$
$$1.8 \times 10^{-7} \beta_t/aT^2 \ll 1,$$

when a is expressed in meters, T in keV, n in 10^{20} m^{-3}, and the Coulomb logarithm is set to 15.

Let us substitute with the characteristic parameters for the devices TCV and ITER-FEAT [2].

TCV, a typical experiment with electron cyclotron resonance heating and current drive:
$T=T_i \approx 0.5$ keV, $a = 0.24$ m, $n \approx 1.5 \times 10^{19}$ m^{-3}, $\beta \approx 0.005$ *(parameters of ohmic low density plasmas):*

$$2.1 \times 10^4 \gg 1$$
$$1.75 \times 10^{-2} \ll 1 \qquad (2.19a)$$
$$1.5 \times 10^{-8} \ll 1$$

ITER-FEAT, typical conditions: $T \approx 20$ keV, $a = 2.0$ m, $n \approx 1.0 \times 10^{20}$ m^{-3}, $\beta \approx 0.035$:

$$6.0 \times 10^5 \gg 1$$
$$2.2 \times 10^{-3} \ll 1 \qquad (2.19b)$$
$$7.9 \times 10^{-12} \ll 1$$

It is clearly seen that the requirement of high collisionality is not satisfied in present tokamak experiments and it will not be satisfied in fusion plasmas (first conditions in (2.19a) and (2.19b)). Nevertheless, during many years of fusion researches, the ideal MHD theory was successfully used to explain some important phenomena in fusion-grade plasmas. This is because different ideal MHD

equations in (2.1 – 2.7) have different validity ranges and the parts of the model that imply the high collisionality are not determinant in the description of most macroscopic plasma phenomena.

2.2 The plasma equilibrium. Grad-Shafranov equation. Tokamak

2.2.1 The plasma equilibrium: basic considerations

We consider static equilibria, where the velocity $\mathbf{v}$ and its derivative $d\mathbf{v}/dt$ are set to zero. Thus, the MHD equations become:

$$\mathbf{J} \times \mathbf{B} = \nabla p \tag{2.20}$$

$$\nabla \times \mathbf{B} = \mu_0 \mathbf{J} \tag{2.21}$$

$$\nabla \cdot \mathbf{B} = 0 \tag{2.22}$$

These equations show that the plasma pressure gradient force ∇p is balanced by the magnetic force $\mathbf{J} \times \mathbf{B}$ in the equilibrium. The magnetic trap has at least to satisfy these equations in order to be able to confine the plasma. Another important condition is the stability of the equilibrium in the trap against different kinds of distortions, as described in the next section.

According to the ideal MHD equations, the plasma particles can freely move along the magnetic field lines. If the magnetic field lines leave the plasma, the particles, following them, will also leave the plasma, thus the plasma will disappear very soon. To avoid this, the magnetic field lines have to be contained inside the plasma. The simplest configuration that has this property is the torus. In the tore, the magnetic field lines do not leave the plasma and the losses in such a configuration are due to diffusion of heat and particles across the magnetic field lines. The perpendicular thermal diffusivity could be very small, but in reality there are numerous processes, like particle drift, instabilities of different kinds, convection etc, that enhance the losses of heat and particles. To close the most important channels of leak, the particle drifts, caused by various forces, the magnetic field lines have not only to be enclosed inside the plasma, but also they have to wind around the tore, going from the outer side to the inner side, thus they are twisted in both toroidal and poloidal directions.

From equation (2.20) one can see that

$$\mathbf{B} \cdot \nabla p = \mathbf{B} \cdot [\mathbf{J} \times \mathbf{B}] = 0 \tag{2.23}$$

$$\mathbf{J} \cdot \nabla p = \mathbf{J} \cdot [\mathbf{J} \times \mathbf{B}] = 0 \tag{2.24}$$

It follows that the magnetic lines lie on the *p*=const surfaces and the current lines are also following these surfaces. The magnetic field lines are turning around the torus within a magnetic surface. If the magnetic field line closes on itself after a rational number of toroidal turns, this surface is called a rational surface, since the ratio of the number of toroidal rotations to the number of poloidal rotations after which the field line closes on itself is a rational number. If the field lines do not close, then they cover the entire magnetic surface, which corresponds to ergodic surfaces. Most of magnetic surfaces in the configurations of interest are ergodic, but the rational surfaces are of great importance for the plasma stability.

2.2.2 Equilibrium of the axysimmetric plasma tore: the Grad-Shafranov equation

The cornerstone of the MHD theory of toroidal systems is the Grad-Shafranov equation [4, 5], which describes the two-dimensional equilibrium of a toroidal axysimmetric plasma. This equation provides the basis for subsequent stability analysis. The derivation of the Grad-Shafranov equation is given here according to [26].

The following plasma configuration is considered: the plasma torus, assumed symmetric with respect to the vertical axis *Z* (Figure 2.1). (*R*, ϕ, *Z*) form a cylindrical right-handed coordinate system.
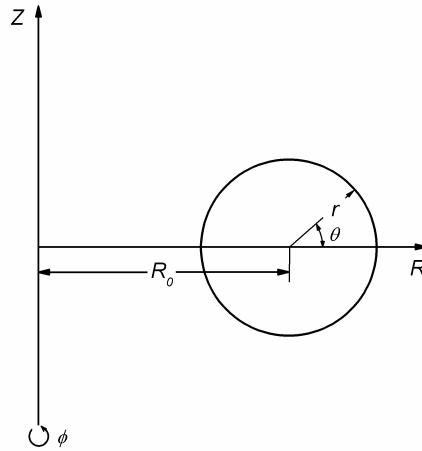
Figure 2.1: The geometry of the axysimmetric toroidal equilibrium

The axial symmetry of the system implies that $\partial S / \partial \phi = 0$, where S is any scalar. Therefore equation (2.22) can be written as

$$\nabla \cdot \mathbf{B} = \frac{1}{R} \frac{\partial (RB_r)}{\partial R} + \frac{\partial B_Z}{\partial Z} = 0 \qquad (2.22')$$

This yields a stream function ψ for the poloidal magnetic field:

$$B_r = -\frac{1}{R} \frac{\partial \psi}{\partial Z}, \quad B_Z = \frac{1}{R} \frac{\partial \psi}{\partial R} \qquad (2.25)$$

11

where $\psi = RA_\phi$ and A_ϕ is the toroidal component of vector potential. In other terms,

$$\mathbf{B} = B_\phi \mathbf{e}_\phi + \mathbf{B}_p \text{, with } \mathbf{B}_p = \frac{1}{R}\nabla\psi\times\mathbf{e}_\phi \qquad (2.26)$$

The stream function is related to the poloidal flux in the plasma, ψ_p

$$\psi_p = \int_S \mathbf{B}_p \cdot d\mathbf{S} \qquad (2.27)$$

Let us choose the integration area S as the surface, lying in the $Z=0$ plane, extending from the magnetic axis $R=R_{axis}$ to an arbitrary ψ contour defined by $\psi=\psi(R_b,0)$ as shown in Fig. 2.2. Then,

$$\psi_p = \int_0^{2\pi} d\phi \int_{R_{axis}}^{R_b} dR\, R\, B_Z(R,Z=0) = 2\pi \int_{R_{axis}}^{R_b} dR R \frac{1}{R}\frac{\partial\psi}{\partial R} = 2\pi \int_{\psi(R_{axis},0)}^{\psi(R_b,0)} d\psi = 2\pi(\psi(R_b,0)-\psi(R_{axis},0)) = 2\pi\psi \quad (2.28)$$

The integration constant is chosen such that the poloidal flux is equal to zero at the magnetic axis: $\psi_{axis}=\psi(R_{axis},0)=0$. It is convenient to label the flux surfaces by ψ.
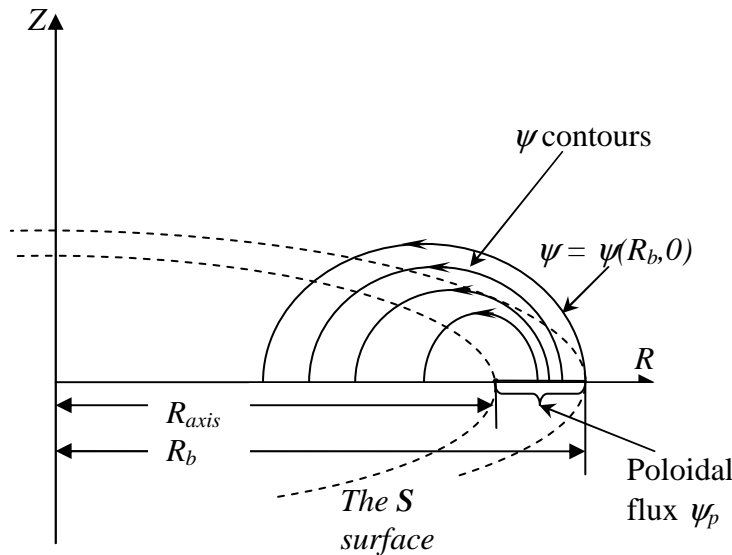
Figure 2.2: The surface through which the poloidal flux ψ_p passes (the ring in the Z=0 plane, contoured by dashed lines)

The Grad-Shafranov equation is obtained from equations (2.20-2.22, 2.26). Substituting (2.26) into (2.21), the following expression for the current density is obtained:

12

$$\mu_0 \mathbf{J} = \mu_0 J_\phi \mathbf{e}_\phi + \frac{1}{R} \nabla(RB_\phi) \times \mathbf{e}_\phi$$

$$\mu_0 J_\phi = -\frac{1}{R} \Delta * \psi \tag{2.29}$$

where the elliptic operator $\Delta*$ is given by

$$\Delta * \psi = R^2 \nabla \cdot \left(\frac{\nabla \psi}{R^2} \right) = R \frac{\partial}{\partial R} \left(\frac{1}{R} \frac{\partial \psi}{\partial R} \right) + \frac{\partial^2 \psi}{\partial Z^2} \tag{2.30}$$

Then equations (2.26) and (2.29) are substituted into the momentum equation (2.20). This equation is decomposed in three components, along $\mathbf{B}, \mathbf{J}$ and $\nabla \psi$, normal to the flux surface.
The $\mathbf{B}$ component gives:

$$\mathbf{B} \cdot \nabla p = \mathbf{e}_\phi \cdot \nabla \psi \times \nabla p = 0 \tag{2.31}$$

This implies that p is a flux surface quantity,

$$p = p(\psi) \tag{2.32}$$

For the $\mathbf{J}$ component one obtains:

$$\mathbf{J} \cdot \nabla p = \mathbf{e}_\phi \cdot \nabla \psi \times \nabla(RB_\phi) = 0 \tag{2.33}$$

and thus RB_ψ is also a flux surface quantity,

$$RB_\psi = F(\psi) \tag{2.34}$$

$F(\psi)$ is related to the net poloidal current flowing in between the plasma and the toroidal field coils. The current flowing through a surface lying in the Z=0 plane and extending out to an arbitrary ψ contour defined by $\psi = \psi(R_b,0)$, equals

$$I_p = \int \mathbf{J_p} \cdot d\mathbf{S} = -\int_0^{2\pi} d\phi \int_0^{R_b} dRRJ_z(R,Z = 0) = -2\pi F(\psi) \tag{2.35}$$

The Grad-Shafranov equation can be obtained by substitution of equations (2.32) and (2.34) into the $\nabla\psi$ component of the momentum equation, resulting in [26, p. 111]

$$\Delta^*\psi = -\mu_0 R^2 \frac{dp}{d\psi} - F\frac{dF}{d\psi} \tag{2.36}$$

$$\mathbf{B} = \frac{1}{R}\nabla\psi\times\mathbf{e}_\phi + \frac{F}{R}\mathbf{e}_\phi = \mathbf{B}_p + \frac{F}{R}\mathbf{e}_\phi$$

(2.37)

$$\mu_0\mathbf{J} = \frac{1}{R}\frac{dF}{d\psi}\nabla\psi\times\mathbf{e}_\phi - \frac{1}{R}\Delta^*\psi\mathbf{e}_\phi = \frac{dF}{d\psi}\mathbf{B}_p - \frac{1}{R}\Delta^*\psi\mathbf{e}_\phi \tag{2.38}$$

where $p(\psi)$ and $F(\psi)$ are two free functions, and $\mathbf{B}_p = \frac{1}{R}\nabla\psi\times\mathbf{e}_\phi$ is the poloidal magnetic field.

The Grad-Shafranov equation (2.36) is a second-order nonlinear partial differential equation describing axysimmetric toroidal equilibria. Different types of magnetic traps are described by this equation, depending on the choices of the two free functions $p(\psi)$ and $F(\psi)$ and of the boundary conditions.

2.2.3. The tokamak. Conception, figures of merit, aspect ratio and ordering

The tokamak is the most advanced type of magnetic plasma trap at the moment. Most experimental devices for thermonuclear plasma researches are tokamaks and the project of the first international thermonuclear experimental reactor ITER is also based on the tokamak conception.

The tokamak is a toroidal axysimmetric device, where the required confinement properties are obtained by combination of the toroidal magnetic field, produced by the toroidal coils surrounding the plasma, and the poloidal magnetic field produced by the current flowing inside the plasma torus. In the tokamak the plasma current is useful for the ohmic heating of the plasma, and it is required for the creation of a stable configuration of magnetic fields. Without the poloidal magnetic field of the plasma current the $\mathbf{E}\times\mathbf{B}$ drift would rapidly throw out the plasma to the wall. This current is usually created by the inductive effect, and the sustainment of a constant plasma current requires a constant increase or decrease of the current in the inductive coils (the primary current). Therefore, the tokamak is only able to work periodically, and breaks are required between pulses. Efforts are now devoted to the non-inductive sustainment of the plasma current, in order to increase the length of plasma discharges in tokamaks, up to steady-state operations.

The tokamak is presented schematically in Figure 2.3.
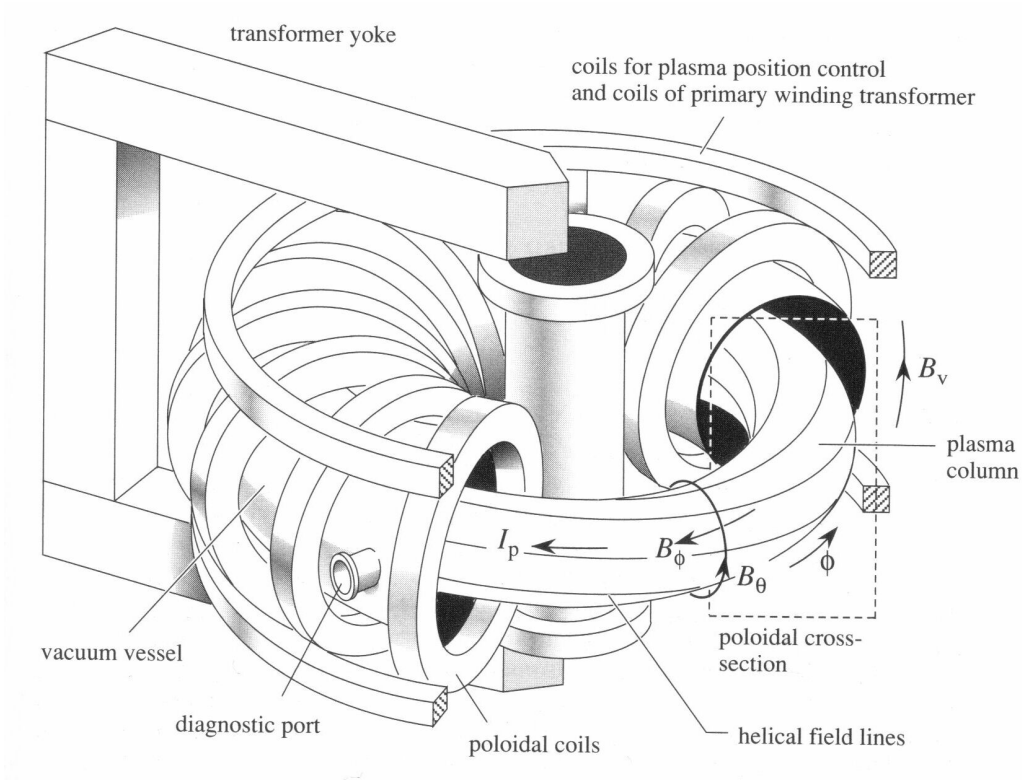
Figure 2.3 Basic elements of a tokamak

It is useful to introduce here some plasma parameters that will be used later.

The toroidal coordinate system r, θ, ϕ (Figure 2.1) is very convenient for the description of tokamak geometry, including the main shaping terms [27]

$$R = R_0 + r\cos(\theta + \delta\sin\theta))$$
$$Z = r\kappa\sin\theta$$

$$(2.39)$$

This equation defines the shape of flux surfaces, ψ = const. The trajectory of the magnetic field line is described by

$$\frac{Rd\phi}{B_\phi} = \frac{dl_p}{B_p}$$

$$(2.40)$$

where $dl_p = \{(dr)^2 + (r\,d\theta)^2\}^{1/2}$ is the poloidal arc length and

$$B_p = (B_r^2 + B_\theta^2)^{1/2} = \frac{|\nabla\psi|}{R}$$

$$(2.41)$$

is the poloidal magnetic field.

The safety factor that describes the ratio of poloidal to toroidal rotations of the magnetic field line on the magnetic surface is defined as

$$q(\psi) = \frac{d\phi}{d\theta} = \frac{F(\psi)}{2\pi} \oint \frac{dlp}{R^2 B_p} \tag{2.42}$$

where the integral is taken on the flux surface where the magnetic field lines lie, defined by (2.40). The magnetic shear is given by

$$s(\psi) = 2\left(\frac{V}{V'}\right)\left(\frac{q'}{q}\right) = \frac{\rho}{q}\frac{dq}{d\rho}\bigg|_\psi \tag{2.43}$$

where V is the flux surface volume, ρ represents the radial coordinate and the prime means differentiation with respect to ψ. The magnetic shear is very important for the plasma stability, as it will be shown later. The "toroidal beta", the ratio of the plasma pressure and the magnetic pressure is given by

$$\beta_t = \frac{2\mu_0\langle p\rangle}{B_0^2} \tag{2.44}$$

where

$$\langle p\rangle = \frac{1}{V_0}\int_0^{V_0} p(V)\,dV \tag{2.45}$$

is the volume average plasma pressure, $V_0 = V(\psi_b)$ and ψ_b is the value of ψ at the plasma boundary The poloidal beta is defined as

$$\beta_p = \frac{2\mu_0\langle p\rangle}{\overline{B}_p^2} \tag{2.46}$$

where $\overline{B}_p$ is an average poloidal magnetic field.

The so-called "beta Bussac", the key value for the stability of the ideal internal kink mode, as it will be discussed later, is given by

$$\beta_{bu} = \frac{2\mu_0(\langle p\rangle_1 - p_1)}{\overline{B}_{p1}^2} \tag{2.47}$$

where p_1 is the plasma pressure on the magnetic surface where $q(\psi_1) = 1$,

$$\langle p \rangle_1 = \frac{1}{V_1} \int_0^{V_1} p(V)\, dV = \frac{1}{V_1} \int_0^{\psi_1} p V'\, d\psi \tag{2.48}$$

is the average plasma pressure inside the $q = 1$ surface, V_1 being the volume inside the $q = 1$ surface and $\overline{B}_{p1}$ is the average poloidal magnetic field at the $q = 1$ surface.

One of the most important parameters of a tokamak is the aspect ratio

$$A \equiv \frac{R_0}{a} \tag{2.49}$$

where R_0 and a are the major and minor radii of the plasma tore, respectively. Often it is more convenient to use the inverse aspect ratio,

$$\varepsilon \equiv \frac{a}{R_0} \tag{2.50}$$

The major plasma parameters are of the following orders with respect to ε in present tokamaks:

$$\frac{B_p}{B_\phi} \sim \varepsilon \tag{2.51}$$

$$\beta_t \sim \frac{2\mu_0 p}{B_\phi^2} \sim \varepsilon^2 \tag{2.52}$$

$$\beta_p \sim \frac{2\mu_0 p}{B_p^2} \sim 1 \tag{2.53}$$

$$q \sim \frac{r B_\phi}{R B_p} \sim 1 \tag{2.54}$$

The Grad-Shafranov equation can not be solved in quadratures in the general tokamak case. There are some "standard" equilibria that can be solved analytically [10, 28] and are used, for example, for testing the computer codes that solve the Grad-Shafranov equation numerically. Analytically, this equation is usually solved by expansion of basic values on small parameters that exist in the tokamak plasma. Corresponding linearized equations are then solved analytically. The solution is thus obtained as a sum of terms, corresponding to different orders of these small parameters. The most important small parameter is the inverse aspect ratio ε. Depending on the model, expansion on other small parameters can be combined with the expansion on ε.

The early generation of tokamaks had $\varepsilon \sim 0.1$ and it was reasonable to consider this parameter as small. However, more recent tokamak experiments demonstrate the trend to increasing ε, mostly because of better confinement and stability properties that such configurations have. Tokamaks like

TCV have $\varepsilon \sim 0.3$ and the recently constructed tight aspect ratio tokamak MAST (Culham Laboratories, UK) and NSTX (Princeton Plasma Physics Laboratory, US) have inverse aspect ratios around 0.7 - 0.8, which clearly can not be considered as small anymore. The theory of many physical phenomena, nevertheless, is developed under the classical consideration of small and even moderate ε and therefore the question of the validity of these theoretical predictions in the case of high ε is important.

2.3 Ideal MHD stability

The MHD equilibrium is a state where the forces that act on the system are completely balanced. The perturbations of this state that occur inevitably in real systems change the force balance. The evolution of the equilibrium depends on the behavior of these perturbed forces that can either restore the initial equilibrium state or enhance the perturbations, leading to the partial or complete destruction of the plasma confinement. The instabilities, described by the ideal MHD theory, are very dangerous because they develop on the ideal MHD time scale, which is of the order of microseconds. Thus, the ideal MHD stability is a necessary condition of the good performance of the magnetic plasma trap. Different approaches to the task of determination of the ideal MHD stability of the plasma equilibrium will be shortly considered below.

2.3.1 Normal mode formulation. Eigenvalue problem

Following the description in [26], one can formulate the linear stability equations by assuming that the deviations from the equilibrium state are exponential and can be expressed as

$$\tilde{Q}_1(\mathbf{r},t) = Q_1(\mathbf{r})e^{-i\omega t} \tag{2.55}$$

where $\tilde{Q}_1$ represents a small perturbation about the equilibrium value Q_0, such that $\left|\tilde{Q}_1\right|/\left|Q_0\right| << 1$.

If $\mathrm{Im}(\omega) \leq 0$, the system is exponentially stable and (2.55) describes periodical oscillations around the equilibrium state. If $\mathrm{Im}(\omega) > 0$, then the initial deviation from the equilibrium increases exponentially, so the system is exponentially unstable.

Under the assumption that, as other perturbed values, $\tilde{\xi}(\mathbf{r},t) = \xi(\mathbf{r})e^{-i\omega t}$, equations (2.1, 2.3, 2.5) become

$$\rho_1 = -\nabla \cdot (\rho_0 \xi)$$

$$p_1 = -\xi \cdot \nabla p_0 - \gamma p_0 \nabla \cdot \xi \tag{2.56}$$

$$\mathbf{Q} \equiv \mathbf{B}_1 = \nabla \times (\xi \times \mathbf{B}_0)$$

18

Substitution of these expressions into (2.2) gives [26]

$$-\omega^2 \rho_0 \xi = \mathbf{F}(\xi), \qquad (2.57)$$

where

$$\mathbf{F}(\xi) = \frac{1}{\mu_0}(\nabla \times \mathbf{B_0}) \times \mathbf{Q} + \frac{1}{\mu_0}(\nabla \times \mathbf{Q}) \times \mathbf{B_0} + \nabla(\xi \cdot \nabla p_0 + \gamma p_0 \nabla \cdot \xi) \qquad (2.58)$$

The equation (2.57) gives the normal-mode formulation of the ideal MHD stability problem. This equation can be interpreted as the eigenvalue problem for the eigenvalue ω^2. This approach is often implemented in the linear stability numerical codes (see the next chapter).

It is important to note that the operator $\mathbf{F}(\xi)$ is self-adjoint, i.e. [29]

$$\int \boldsymbol{\eta} \cdot \mathbf{F}(\xi)d\mathbf{r} = \int \xi \cdot \mathbf{F}(\boldsymbol{\eta})d\mathbf{r} \qquad (2.59)$$

This property of the operator $\mathbf{F}(\xi)$ is very useful. For example, it means that the eigenvalues ω^2 of equation (2.57) are real. This can be seen by integrating the dot product of equation (2.57) with $\xi^*(\mathbf{r})$ over the plasma volume:

$$\omega^2 \int \rho |\xi|^2 d\mathbf{r} = -\int \xi^* \cdot \mathbf{F}(\xi)d\mathbf{r} \qquad (2.60)$$

Then integrating the dot product of the vector $\xi(\mathbf{r})$ with the complex conjugate of (2.57):

$$\omega^{*2} \int \rho |\xi|^2 d\mathbf{r} = -\int \xi \cdot \mathbf{F}(\xi^*)d\mathbf{r} \qquad (2.61)$$

Subtracting (2.61) from (2.60), one obtains for any displacement ξ

$$(\omega^2 - \omega^{*2}) \int \rho |\xi|^2 d\mathbf{r} = -\int \xi^* \cdot \mathbf{F}(\xi)d\mathbf{r} - \left(-\int \xi \cdot \mathbf{F}(\xi^*)d\mathbf{r}\right) = -\int \xi^* \cdot \mathbf{F}(\xi)d\mathbf{r} - \left(-\int \xi^* \cdot \mathbf{F}(\xi)d\mathbf{r}\right) = 0 \quad (2.62)$$

Thus, $\omega^2 = \omega^{*2}$ and ω^2 is real. This guarantees that ω is either purely real, when $\omega^2 > 0$ and equation (2.55) describes the oscillations around the equilibrium or ω is purely imaginary, when $\omega^2 < 0$ and (2.55) describes exponential growth. The transition from stability to instability occurs at $\omega^2 = 0$.

The solutions of equation (2.57) gives a spectrum of eigenvalues. Typically, the spectrum consists of discrete negative unstable modes, if they exist, and of both discrete modes and continua in the positive, stable range [30, 31, 32]. The most negative eigenvalue $\omega^2 < 0$, if present, is the most unstable mode. In this case $\gamma = \mathrm{Im}(\sqrt{\omega^2}) = \sqrt{-\omega^2}$ gives the mode growth rate.

2.3.2 The potential energy variation and the energy principle

The equation (2.57) has a direct relation with the change of potential energy δW of the system, associated with the perturbation ξ. δW can be obtained by integrating the dot product of equation (2.57) and ξ^* over the plasma volume:

$$\delta W(\xi^*,\xi) = -\frac{1}{2}\int \xi^* \cdot \mathbf{F}(\xi)d\mathbf{r} =$$

$$= -\frac{1}{2}\int \xi^* \cdot \left(\frac{1}{\mu_0}(\nabla\times\mathbf{B_0})\times\mathbf{Q} + \frac{1}{\mu_0}(\nabla\times\mathbf{Q})\times\mathbf{B_0} + \nabla(\xi\cdot\nabla p_0 + \gamma p_0\nabla\cdot\xi)\right)d\mathbf{r} = \omega^2 K(\xi^*,\xi) \tag{2.63}$$

where $K(\xi^*,\xi) = -\frac{1}{2}\int \rho|\xi^2|d\mathbf{r}$ is proportional to the kinetic energy of the plasma.

δW can be interpreted as the work done against the force $\mathbf{F}(\xi)$, when the plasma displaces by ξ. It can be shown accurately [6] that it is necessary and sufficient that

$$\delta W(\xi^*,\xi) \geq 0 \tag{2.64}$$

for all possible displacements ξ, for the plasma equilibrium to be stable. In other words, if for all displacements the minimum variation of the potential energy is positive, the equilibrium is stable, but if it is negative for a displacement, then the equilibrium is unstable. This is called the energy principle and is widely used for analysis of the ideal MHD stability of the plasma equilibria of different kinds.

2.3.3 Extended energy principle. Basic types of ideal MHD instabilities. External and internal kink modes

There exist a variety of ideal MHD instabilities that can be unstable in the plasma. They can be classified by the main driving mechanism and by the type of plasma displacement, especially by the presence or absence of the plasma boundary perturbation.

Equations (2.57, 2.58) describe the plasma, directly surrounded by a conducting wall or separated from the wall by a vacuum region. In the first case the boundary condition is evident: the plasma cannot move across the wall,

$$\mathbf{n} \cdot \xi \big|_{\mathbf{r}_w} = 0 \qquad (2.65)$$

where $\mathbf{r}_w$ is the wall position and $\mathbf{n}$ is the normal vector of the plasma surface. Thus, in this case $\xi\big|_{\mathbf{r}_w} = \xi_{//}\big|_{\mathbf{r}_w}$. The unstable modes in such configurations do not disturb the plasma boundary and therefore they are called *internal modes*. If there is vacuum between the wall and the plasma, then the mode can disturb the plasma boundary. Such modes are denoted as *external modes* if they become stable when the wall is on the plasma. In this case the energy principle has to be reformulated, including the influence of the vacuum and plasma-vacuum interface [26]. Another distinction is often used between pressure driven and current driven modes. Upon neglecting surface-vacuum and vacuum volume terms, this is seen by re-writing δW as follows [33, 34]:

$$\delta W = \frac{1}{2} \int d\mathbf{r} \left(\frac{|\mathbf{Q}_\perp|^2}{\mu_0} + \frac{B_0^{\,2}}{\mu_0} |\nabla \cdot \xi_\perp + 2\xi_\perp \cdot \kappa|^2 + \gamma p_0 |\nabla \cdot \xi|^2 - 2(\xi_\perp \cdot \nabla p_0)(\kappa \cdot \xi_\perp^*) - J_{0//}(\xi_\perp^* \times \mathbf{b}) \cdot \mathbf{Q}_\perp \right) \quad (2.66)$$

where $\kappa \equiv (\mathbf{b} \cdot \nabla)\, \mathbf{b}$ is the field line curvature, $\mathbf{Q}_\perp$ is the parallel component of $\mathbf{Q}$, $J_{0\|}$ is the parallel component of $\mathbf{J}_0$. The terms in (2.66) have different physical meanings and describe the various factors determining the equilibrium stability. The term $|\mathbf{Q}_\perp|^2$ is the energy required to bend the magnetic field lines. The second term represents the energy required to compress the magnetic field. The third term corresponds to the energy of plasma compression. These three terms are always positive, i.e. stabilizing. The fourth term is proportional to ∇p_0, the gradient of the plasma pressure. This term can be negative and it can be shown that generally the high pressure gradient is a destabilizing factor [34]. The modes, where this term is predominating, are called *pressure-driven modes*. They can exist even if there are no parallel currents in the plasma, because they are driven by perpendicular currents ($\nabla p_0 \sim \mathbf{J}_{0\perp} \times \mathbf{B}_0$). The most important pressure-driven modes are *interchange modes* and *ballooning modes*.

The last term is proportional to $J_{0\|}$ and is negative. The modes that are driven by this term can exist even in zero-pressure force-free plasma with parallel current. Among these *current-driven modes,* the modes with long parallel wavelengths and macroscopic perpendicular wavelengths ($k_\|/k_\perp \ll 1$, $k_\perp a \sim 1$) are the most dangerous and are called *kink modes*. Depending on the perturbation of the plasma boundary, they can be divided into *internal kink modes* and *external kink modes*.

The behavior of these modes is the subject of the present work and will be analyzed in more details below. It is important to mention that the division into pressure-driven and current-driven modes is rather academical. In realistic cases, both driving mechanisms are present and have to be taken into account.

2.4 The ideal kink mode stability: analytical approach

Here the main aspects of the stability of the internal and external kink modes, representing the greatest interest for the present work, will be discussed.

2.4.1 The internal kink mode in a cylindrical "straight" tokamak

To understand the main assumptions used to obtain an analytical formulation of the ideal internal kink mode, it is useful to use the result obtained in a straight tokamak. In such a simple geometry one can calculate the first contribution to the potential energy [26, p.340]. Since we are ultimately interested in the growth rate $\gamma \tau_a = -\dfrac{\pi}{s_1} \delta \hat{W}$ with $\delta \hat{W} = \dfrac{\delta W}{W_0}$, where

$$W_0 = \frac{2\pi^2 \xi_0^2 B_0^2 R_0 \varepsilon^2}{\mu_0} ,$$ (2.67)

and $\varepsilon = \dfrac{r_1}{R_0}$, we discuss the order of the various contributions with respect to the normalized potential energy $\delta \hat{W}$. It is important to note that $W_0 \sim O(\varepsilon^2)$ which is why $\delta \hat{W}$ terms of order $O(\varepsilon^2)$ here correspond to $O(\varepsilon^4)$ in Ref. [26] for example. The first non-vanishing term is of 0th order in this notation:

$$\delta \hat{W}_{\varepsilon^0} = \frac{1}{W_0} \frac{2\pi^2 B_0^2}{\mu_0 R_0} \int_0^a \left(\frac{n}{m} - \frac{1}{q} \right)^2 (r^2 \xi'^2 + (m^2 - 1)\xi^2)r dr$$ (2.68)

where ξ is the radial displacement. For $m > 1$ and arbitrary n both terms in (2.68) are positive and nonzero. Thus, $\delta \hat{W}_{\varepsilon^0} > 0$ and these modes are stable. With $m = 1$, the mode is also stable if q increases with r and if $nq_0 > q_0 > 1$. If a $q = 1$ surface exists in the plasma, then it is possible to construct a trial function for ξ that will reduce $\delta \hat{W}_{\varepsilon^0}$ to zero: a step function that equals zero outside the $q = 1$ surface

and equals ξ_0 inside $q = 1$ surface. It jumps from 0 to ξ_0 in a small vicinity $\delta \rightarrow 0$ of the $q = 1$ surface (Figure 2.4). This special behavior of the $m = 1$ mode is caused by the coupling between the $m = 1$ poloidal structure of the mode and the poloidal curvature of plasma.
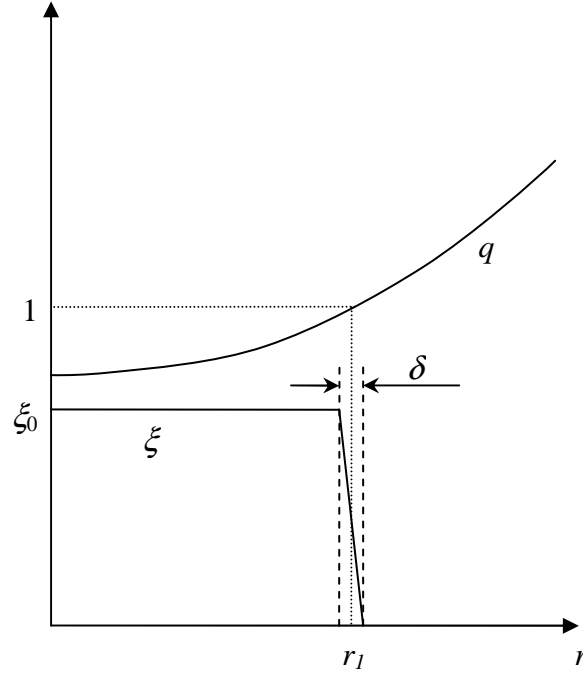

Figure 2.4: The"top-hat" radial displacement function ξ for the internal kink mode $m = 1$ in a "straight" tokamak

Since $\delta\hat{W}_{\varepsilon^0} = 0$, the higher order expansion terms determine the mode stability, the next non-vanishing term being of order ε^2 [35]:

$$\delta\hat{W}_{\varepsilon^2} = \frac{1}{\varepsilon^2 R_0^2} \int_0^{r_1} \left(r\beta' + \frac{r^2}{R_0^2}(1 - \frac{1}{q})(3 + \frac{1}{q}) \right) r dr \qquad (2.69)$$

where r_1 is the location of the $q = 1$ surface (see Fig. 2.4). It is important to mention that contributions from both pressure gradient and parallel current are present and are negative, i.e. destabilizing. Thus, in the case of the "straight" tokamak the $m = 1$ mode is unstable with $\delta\hat{W} \sim \varepsilon^2$. The "straight" tokamak model, although useful for understanding the concepts of the ideal MHD stability of a tokamak, does not include important effects, arising in the realistic toroidal configurations, where the contribution (2.69) disappears in the most important case of $n = 1$. The toroidal effects will be discussed in the Section 2.4.3.
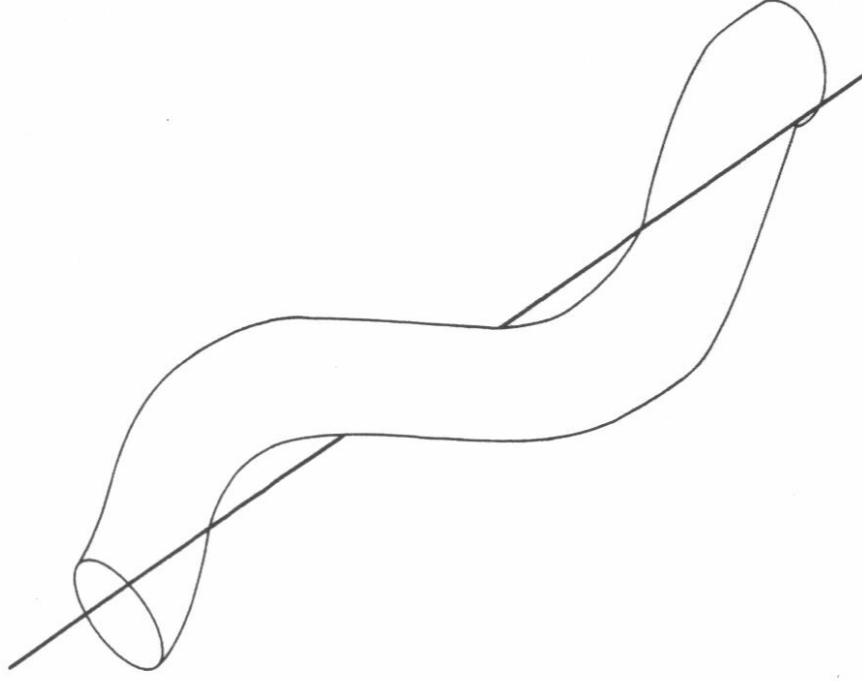
Figure 2.5 The m=1 kink mode

2.4.2 The external kink mode

The external kink modes are generally more unstable and mode dangerous than the internal modes, because their stability is determined by the ε^0 contribution to $\gamma\tau_a$ and because they alter the plasma up to the edge boundary.

In the case of the external mode, $\delta\hat{W}$ consists of the plasma, surface and vacuum terms

$$\delta\hat{W} = \delta\hat{W}_F + \delta\hat{W}_S + \delta\hat{W}_V \tag{2.70}$$

Assuming the conducting wall is at infinity, the first non-vanishing $\delta\hat{W}$ contribution is of the order ε^0 [26, p.342]:

$$\delta\hat{W}_{\varepsilon^0} = \frac{1}{W_0}\frac{2\pi^2 B_0^2}{\mu_0 R_0}\int_0^a\left(\frac{n}{m}-\frac{1}{q}\right)(r^2\xi'^2 + (m^2-1)\xi^2)rdr + \xi_a^2\left(\frac{n}{m}-\frac{1}{q_a}\right)\left[|m|\left(\frac{n}{m}-\frac{1}{q_a}\right)+\left(\frac{n}{m}+\frac{1}{q_a}\right)\right] \tag{2.71}$$

The first term, corresponding to the fixed-boundary case (2.68), is always positive and nonzero and thus, the external mode stability is determined by the second term. Considering $q_a > 0$, $m > 0$ and arbitrary n, which does not affect the generality of the consideration, one can see that the second term is positive and the mode is stable if

$$\frac{n}{m} > \frac{1}{q_a} \tag{2.72}$$

or if

$$\frac{n}{m} < 0 \tag{2.73}$$

The mode can be unstable if and only if

$$0 < \frac{n}{m} < \frac{1}{q_a} \tag{2.74}$$

In the case of q increasing with the radius, as in tokamaks, this condition implies that the $q = m/n$ surface lies outside the plasma, in the vacuum region.

In the $m = 1$ case, the first term in (2.71) vanishes if the eigenfunction in plasma is $\xi(r) = \xi_a = $ const. Such a choice is possible only for the external mode, because the internal mode requires that $\xi_a = 0$ (2.65). The minimizing eigenfunction is flat and does not depend on the q profile and thus, the stability is function of q_a only:

$$\delta \hat{W}_{\varepsilon^0} = \frac{4\pi^2 B_0^2 \xi_a^2}{W_0 \mu_0 R_0} \left(n(n - \frac{1}{q_a}) \right) \tag{2.75}$$

For the most dangerous case, $n = 1$, the stability condition becomes

$$q_a > 1 \tag{2.76}$$

This criterion, named the Kruskal-Shafranov condition [36, 37], sets the limitation to the total toroidal current that can be created in the tokamak plasma with the circular cross-section:

$$I_p < I_{KS} = \frac{2\pi a^2 B_0}{\mu_0 R_0} \tag{2.77}$$

2.4.3 The large aspect ratio tokamak: the role of toroidicity in the internal kink mode stability

The next step towards the real plasma is the model of the large aspect ratio tokamak with circular cross-section. The stability of internal kink modes in such geometry was first analytically considered in [12]. Note that in the case of the toroidal tokamak the plasma represents a tore with the major radius R_0 and the minor radius a. For the usual tokamak ordering and assuming that $\varepsilon \equiv \dfrac{a}{R_0} \ll 1$, it was found after complicated calculations that in the case of the toroidal tokamak the term $\delta \hat{W}_{\varepsilon^2}$ becomes [12]:

$$\delta \hat{W}_{\varepsilon^2} = \left(1 - \frac{1}{n^2}\right)\delta\hat{W}_c + \frac{1}{n^2}\delta\hat{W}_t \tag{2.78}$$

where $\delta\hat{W}_c$ is the contribution corresponding to the straight tokamak model, right-hand side of Eq. (2.69), r_s being the radius of the surface where $nq = 1$. In the case of $n = 1$, $\left(1 - \dfrac{1}{n^2}\right) = 0$, thus this cylindrical contribution is completely cancelled by toroidal effects, even at $\varepsilon \to 0$, so that the remaining contribution is of toroidal origin. The reason for that is the matching between the $n = 1$ toroidal mode structure with the toroidal curvature of the tokamak.

$\delta\hat{W}_t$ is the toroidal contribution and it is in general extremely complicated. It can be expressed analytically in the following particular case, assuming that $\dfrac{r_1}{a} \le \varepsilon_1$ and the shape of the q profile inside $q = 1$ surface defined as

$$q(r) = 1 - \Delta q\left[1 - \left(\frac{r}{r_1}\right)^\lambda\right] \tag{2.79}$$

where

$$\Delta q \equiv 1 - q_0. \tag{2.80}$$

For a parabolic q profile ($\lambda = 2$) δW_t becomes [12]

$$\delta\hat{W}_t = n^2\varepsilon_s^2\Delta q\left[\frac{13}{48} - 3\left(\frac{2\mu_0}{B_0^2 n^2\varepsilon_s^2 r_s^2}\int_0^{r_s} r^2\frac{dP}{dr}dr\right)\right]^2 \tag{2.81}$$

For $n = 1$, the most severe case, the term with W_c in (2.78) vanishes and (2.78) becomes

26

$$\delta \hat{W}_{\varepsilon^2} = \varepsilon_1^2 \Delta q \left(\frac{13}{48} - 3\beta_{bu}^2 \right)$$

(2.82)

Therefore the mode is stable if β_{bu} is below some critical value

$$\beta_{crit} = \sqrt{\frac{13}{144}} \approx 0.3$$

(2.83)

If $n > 1$, the picture is closer to the straight tokamak and at $n \gg 1$ it becomes identical to that model. The expression (2.82) represents a benchmark for all analytical and numerical calculations of the ideal internal kink mode stability researches. However this depends to a large part on the form of the q profile inside $q = 1$. Assuming a constant current density inside $q = 1$, it was shown in [38] that the critical β_{bu} is much lower than (2.83). Furthermore, assuming that q_0 is close to 1 such that $\Delta q \sim \varepsilon^2$, equation (2.82) becomes $O(\varepsilon^4)$. This is why the next order term of order ε^4 has been calculated in [13]:

$$\delta \hat{W}_{\varepsilon^2} + \delta \hat{W}_{\varepsilon^4} = \varepsilon_1^2 \Delta q \left(\frac{13}{48} - 3\beta_{bu}^2 \right) + \varepsilon_1^4 \left(6\beta_{bu}^3 (1 + \beta_{bu}) + \beta_{bu} \frac{(1 - 14\beta_{bu})}{32} \right)$$

(2.84)

2.4.4 The internal kink mode in a shaped large aspect ratio tokamak

The minimization procedure, discussed in the example of the "straight" tokamak model is applied to more complex models. The shaped tokamak model, analyzed by numerous authors [14, 15, 39, 40] is of great interest for the present work, because the role of plasma shaping is considered here in details. The algebraic calculations, required for solving the equations that arise in this consideration are highly sophisticated and usually are performed with computational algebraic manipulations. They are mostly omitted here. The initial considerations and the basic results on the mode stability that are of interest for us are discussed. It is important to note that only the $n=1$ mode stability will be discussed here.

The conventional notation of the shaped tokamak geometry is presented schematically on Fig. 2.6. Most important shaping parameters are the plasma elongation κ and triangularity δ. For the circular tokamak $\kappa = 1$, $\delta = 0$. It is often convenient to use a measure of elongation that equals to zero for the circular tokamak and can be used as an expansion parameter, the ellipcity:

$$e \equiv \frac{\kappa - 1}{\kappa + 1}$$

(2.85)

In most cases it has been assumed that $\kappa \sim 1$, which yields

$$e = \frac{\kappa - 1}{2} \tag{2.86}$$

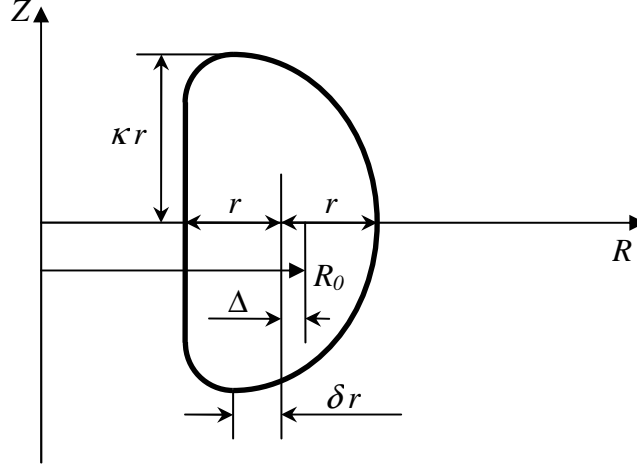We will also look at very high values of κ and this last approximation cannot be used.

Figure 2.6 The geometry of a shaped tokamak: the arbitrary flux surface

Other plasma shape parameters, like quadraticity, etc, can also be introduced. The shaped tokamak plasma is considered here, described by the following general expressions for the flux surfaces [16, 40]:

$$R = R_0 + \hat{r}\cos\omega - \Delta(\hat{r}) + \sum_n S^{(n)}(\hat{r})\cos(n-1)\omega \tag{2.87}$$

$$Z = \hat{r}\sin\omega - \sum_n S^{(n)}(\hat{r})\sin(n-1)\omega \tag{2.88}$$

where ω is the angular variable, non-orthogonal to the minor radius r and R_0 is the major radius of the magnetic axis, $n \geq 2$. Note that $\hat{r}$ is not strictly equivalent to r. The latter is usually derived as the average minor radius, as shown in Figure 2.6. However $\hat{r}$ contains information about the elongation and is related to r with

$$\hat{r} = \frac{r}{1-e} \tag{2.89}$$

where e is given by (2.85). It is important not to employ (2.86) instead of (2.85) since (2.89) would then diverge for $\kappa = 3$.

The Grad-Shafranov equation is solved assuming that the flux surfaces are described by equations (2.87, 2.88), thus the solution of the Grad-Shafranov equation gives the dependences of the Shafranov

shift $\Delta(\hat{r})$ and the shaping coefficients for the Fourier harmonics $S^{(n)}(\hat{r})$ on $\hat{r}$. According to [16] the shaping coefficients dependence on $\hat{r}$ can be described as

$$S^{(n)}(\hat{r}) \sim \left(\frac{\hat{r}}{\hat{a}}\right)^{n-1} S^{(n)}(\hat{a}) \tag{2.90}$$

The coefficients $S^{(2)}$ and $S^{(3)}$ and their relation with the conventional shaping parameters can be found in [40]:

$$\frac{S^{(2)}}{\hat{r}} = \frac{\kappa-1}{\kappa+1} = e \tag{2.91}$$

$$\frac{S^{(3)}}{\hat{r}} = \frac{\delta}{4} \tag{2.92}$$

(higher harmonics are omitted). The inverse aspect ratio is considered as a small parameter $\varepsilon \ll 1$. The plasma current profile is considered to be the same as it was in the case of the circular tokamak, i.e. the q profile is described by (2.80) with $\lambda = 2$, $\frac{r_1}{a} \sim \varepsilon$ and $\Delta q \sim \varepsilon$. The shaping parameters e and δ are considered of the order of ε.

The non-circular geometry adds new terms to the δW expansion, and some terms, existing in the circular case, are modified. For instance, the Bussac term (2.82) becomes [9]

$$\delta\hat{W}_{\varepsilon^2} \cong 3\hat{\varepsilon}_1^2 \Delta q\left((0.3-0.5\frac{\bar{r}_1}{\bar{a}}) - \beta_{bu}^2 \right) \tag{2.93}$$

where $\bar{r}_1 = r_1\sqrt{\kappa_1}$ and $\bar{a} = a\sqrt{\kappa}$, thus taking into account the volume effect in the effective minor radius.

The plasma shaping gives rise to the quasicylindrical terms [14, 16, 39], existing in the case of the shaped straight tokamak. They depend on the shaping parameters κ and δ and have the following form for our conditions:

$$\delta\hat{W}_{e^2} = -\frac{2\Delta q^3}{3}e^2 \tag{2.94}$$

$$\delta\hat{W}_{\delta^2} = \frac{\Delta q}{4}\delta^2 \tag{2.95}$$

The term (2.94) is rather small, but the term (2.95) can become important.

There are also terms arising due to the combined effects of toroidicity and shaping. They were identified for the ideal internal kink mode in [15] and in our conditions become

$$\delta\hat{W}_{\varepsilon^2 e} = \hat{\varepsilon}^2 e\left(-\frac{3}{2}\beta_{bu} + \frac{\Delta q}{12}(156\beta_{bu}^2 - 3\beta_{bu} - 12)\right) \tag{2.96}$$

$$\delta\hat{W}_{\varepsilon e\delta} = \hat{\varepsilon}e\delta\left(3\beta_{bu}^2 + \frac{\Delta q}{6}(4\beta_{bu} - 7)\right) \tag{2.97}$$

The terms $O(\Delta q^2)$ have been neglected. The terms (2.96, 2.97) are often referred to as the Mercier-like terms, because they are identical with the potential energy terms in the expression for the Mercier stability criterion [14].

Thus, the whole expression for $\delta\hat{W}$ in the shaped large aspect ratio tokamak reads [41]:

$$\delta\hat{W} = 3\hat{\varepsilon}^2\Delta q\left((0.3 - 0.5\frac{\bar{r}_1}{a}) - \beta_{bu}^2\right) + \hat{\varepsilon}^4\left(6\beta_{bu}^3(1 + \beta_p) + \beta_{bu}\frac{(1 - 14\beta_{bu})}{32} - \frac{2\Delta q^3}{3}e^2 + \frac{\Delta q}{4}\delta^2 + \right.$$
$$+ \hat{\varepsilon}^2 e\left(-\frac{3}{2}\beta_{bu} + \frac{\Delta q}{12}(156\beta_{bu}^2 - 3\beta_{bu} - 12)\right) + \hat{\varepsilon}e\delta\left(3\beta_{bu}^2 + \frac{\Delta q}{6}(4\beta_{bu} - 7)\right) \tag{2.98}$$

where $\hat{\varepsilon} = \varepsilon/(1 - e)$ and all the terms are evaluated at the $q = 1$ surface. It is important to note that according to (2.96) and (2.97) the plasma elongation is a strong destabilizing factor. The plasma triangularity δ in the term $\delta\hat{W}_{\delta^2}$ (2.95) is stabilizing both when negative and positive, but in the term $\delta\hat{W}_{\varepsilon e\delta}$ (2.97) it is stabilizing when positive and destabilizing when negative (it is assumed here that $\kappa > 1$). Thus, at given Δq, $\kappa > 1$ and β_{bu}, the dependence of $\delta\hat{W}$ on δ is a quadratic parabola, displaced slightly to the negative side (Figure 2.7).

Knowing $\delta\hat{W}$, it is possible then to find the growth rate of the mode γ, normalized to the toroidal Alfven time [42, 43]:

$$\gamma\tau_A = -\frac{\pi}{s_1}\delta\hat{W} \tag{2.99}$$

where the toroidal Alfven time is $\tau_A = \sqrt{3}R_0 / v_a$, v_a is the Alfven velocity and s_1 is the magnetic shear (2.43) on the $q = 1$ surface.

The internal kink mode with $m/n = 1/1$ is the most unstable internal mode. It has a simple physical explanation: the top-hat shape of the corresponding displacement function (Fig. 2.4) means that this mode does not cause deformations of the plasma cross-section, but only of the toroidal bending of the

magnetic lines (Fig. 2.5). Thus, less energy is involved in the development of this instability and it occurs earlier than for other modes which deform the plasma cross-section.
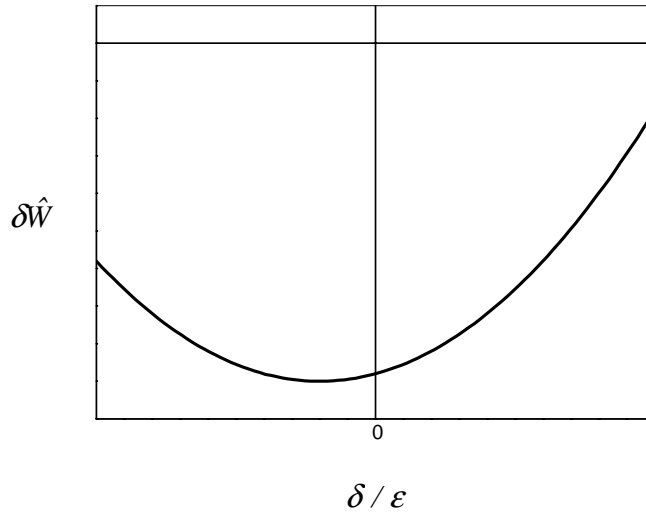

Figure 2.7 The characteristic dependence of $\delta\hat{W}$ on the plasma triangularity ($\kappa > 1$)

Experimentally, this mode is relatively benign and occurs periodically. At each crash, the profile tends to relax to flat profiles inside $q = 1$ and then builds up until it is unstable again [9, 44]. This leads to a sawtooth-like behavior of the soft X-ray measurements or of the central temperature [45]. This is why they are called sawtooth crashes. In experiments with large plasma current, the $q = 1$ radius is large and more than half of the plasma minor radius is affected by these sawtooth crashes.

2. 5 The infernal mode

Another important ideal MHD instability that can appear in the tokamak is the infernal mode, which represents the features of both kink and ballooning modes. This mode can become unstable in low shear conditions, where the q profile becomes flat or reversed in the plasma core. Such conditions are met in some prominent advanced confinement regimes, widely studied on the present-day tokamaks, including TCV. The infernal modes limit the plasma performance in these regimes. The numerical analysis of ideal MHD stability of such plasmas is presented in the Chapter 6, and here a short description of the theoretical basis of these modes is given.

The infernal modes were firstly derived from the implementation of the ballooning modes theory to the low-shear configurations. Ballooning modes are pressure-driven MHD modes with short perpendicular wavelengths, localized in the low field side of the magnetic surfaces, where the magnetic lines curvature is unfavorable for the mode stability.

The classical ballooning theory [45, 46] was developed by Connor, Hastie and Taylor on the basis of the extended energy principle (2.66), assuming $n \gg 1$. Finite (non-zero) shear was an important assumption for this theory, and the basic result was that the instability growth rate is decreasing linearly with $1/n$. The growth rate is a maximum at $1/n = 0$, so the $n \to \infty$ limit provides the stability limit for the ballooning modes.

If somewhere in the plasma the magnetic shear reaches zero, however, the theory [45, 46] does not work and modifications are required. In [47] Hastie and Taylor have presented the modified ballooning modes description of low shear plasmas, assuming as before $n \gg 1$ and showing that the growth rate dependence on n becomes more complicated, oscillations on n appear and allowing that the highest instability growth rate can occur at finite n, and not at $n \to \infty$, as in the monotonic high shear q profile case. This was also found by Dewar et al [48].

The next revision of the ballooning theory [23, 24] included the lower $n > 1$ and lower shear values into consideration. Cases were found that were unstable even if the modified ballooning theory of Hastie-Taylor predicted the complete stability. The term "infernal mode" was introduced [23] to describe these modes. It was shown that the low $n \sim 1$ modes may be also very unstable and may be more unstable than higher n modes.

Another important step was done by analyzing the stability of reversed shear modes [24], showing that at $q_{min} \sim 1$ the low n infernal modes with $n > 1$ can be the most unstable ones. The $n = 1$ mode was still classified as the kink mode, and thus identified separately from the infernal mode. Let us note that at low n, the characteristic feature of classical high n ballooning modes, namely the localization in perpendicular direction that is a clear characteristic for $n \gg 1$, vanishes and the low n modes become more global and kink mode-like. Nevertheless the mode retains prominent localization on the outer magnetic surface side with unfavorable curvature.

Subsequent work [49, 115] has also considered $n = 1$ modes in the infernal mode studies, noting that in some cases the internal $n = 1$ mode can be the most unstable one even if there is no $q = 1$ surface in the plasma.

The development of ballooning theory for reversed shear cases is also continued. Recent publications [51, 52] have shown that for reversed shear plasmas with internal transport barrier, the $n \gg 1$ mode stability is optimized at low q_{min} values. We shall see this is not the case for $n = 1$ infernal modes (Chapter 6).

Thus, historically the meaning of the term "infernal mode" has evolved, going from high, but finite n ballooning modes towards low n and even $n = 1$ modes, existing in the low or reversed shear plasma even in the absence of corresponding resonant surfaces. The latter meaning of infernal modes is referred in this work. That is, infernal modes are low n modes ($n \geq 1$) that remain unstable even in the presence of the ideal wall on the plasma boundary. They have a ballooning characteristic and yet are

similar to external kink. They are both pressure and current driven. The analysis of the reversed shear plasmas stability in the Chapter 6 is devoted to the low n infernal modes which, as it can be seen, are the most unstable modes in the cases of interest.

2.6 Conclusions

The ideal MHD equations and some important applications of the ideal MHD theory were reviewed in this chapter, for instance, the concepts of the MHD equilibrium and stability. Several approaches to the problem of the stability of the magnetically confined plasmas in the MHD equilibrium were discussed and the formulations of these problems, used in the analytical and numerical stability analysis were introduced. Some important analytical solutions of the stability problem in different plasma models were presented and discussed, including the internal kink mode stability in the straight, circular toroidal and shaped toroidal tokamak and the external kink mode stability in the straight tokamak.

The analytical approach, presented in this chapter, is based on some important assumptions, the most important of which is that ε is considered as a small parameter. As it was mentioned above, modern tokamaks have increasing ε, so the validity of these results for moderate and tight aspect ratio tokamaks has to be examined. It will be done by comparing the analytical results with the results of numerical simulations, described in following chapters.

Chapter 3. The numerical approach to the ideal MHD stability. The numerical code KINX. The organization of calculations.

In this chapter we present numerical approaches to solving the ideal MHD equations and describe the computer codes and procedures, used for calculations of the ideal MHD stability of the tokamak plasmas.

3.1. The ideal MHD stability: numerical approach.

In the previous chapter the ideal MHD equations and different formulations of the MHD stability problem were introduced. As it was also described in the previous chapter, the MHD stability can be investigated analytically, which often requires some assumptions and simplifications that are not always satisfied in real plasmas. Another approach to the stability problem is the use of numerical codes, solving the MHD equations in a more general form than it can be done analytically. Numerous computer codes, for example KINX [53], ERATO [54], GATO [55], PEST [56], PEST 2 [57], DCON [58], MISHKA [59], etc. are developed for the ideal MHD stability analysis. The numerical approach will be demonstrated here on the basis of the stability code KINX, used throughout the work.

3.1.1 The stability problem in the KINX code

The code KINX solves the ideal MHD stability problem for axisymmetric plasmas in the eigenvalue formulation, described in the Chapter 2, Sections 2.3.2 – 2.3.3:

$$\delta W(\xi^*,\xi) = \omega^2 K(\xi^*,\xi) \tag{3.1}$$

where δW is the change of potential energy of the system, associated with an arbitrary perturbation $\xi(\mathbf{r},t) = \xi(\mathbf{r})e^{-i\omega t}$ and $K(\xi^*,\xi) = -\frac{1}{2}\int \rho|\xi^2|d\mathbf{r}$ is proportional to the kinetic energy of the plasma, related to this perturbation. The sign of ω^2 (note that ω^2 is necessarily real, see Section 2.3.1) determines the stability of the perturbation: if it is positive, then the configuration is stable and the perturbation will cause harmonic oscillations with the frequency ω. If it is negative, then the plasma configuration is unstable and the initial plasma perturbation will grow with the rate:

$$\gamma = \text{Im}(\sqrt{\omega^2}) = \sqrt{-\omega^2} \tag{3.2}$$

The displacement vector $\xi(\mathbf{r})$ is projected as

$$\xi = \xi^\psi \frac{\mathbf{D} \times \mathbf{B}}{|\mathbf{B}|^2} + \xi^D \frac{\mathbf{B} \times \nabla\psi}{|\mathbf{B}|^2} + \xi^B \frac{\mathbf{B}}{|\mathbf{B}|^2} \qquad (3.3)$$

where **D** is the vector orthogonal to the magnetic field:

$$\mathbf{B} = \nabla\psi \times \mathbf{D}, \qquad (3.4)$$

B is the equilibrium magnetic field (Section 2.2.2, equation 2.37) and ψ is the poloidal magnetic flux stream function (Section 2.2.2., equations 2.25-2.28).

It is assumed that the plasma is surrounded by a vacuum region and by an ideally conducting wall outside the vacuum region (there is also a possibility to consider a resistive wall realized in the code version KINX-R, but it was not used in our work). Then δW can be represented as the sum of the plasma and vacuum contributions

$$\delta W = \delta W_P + \delta W_V \qquad (3.5)$$

and the kinetic energy is evidently present only in the plasma.

In the plasma the potential energy variation is

$$\delta W_P = \frac{1}{2} \int_{V_P} \left\{ |\nabla \times (\xi \times \mathbf{B})|^2 + 2\xi^\psi (\mathbf{J} \cdot \nabla\xi^D) + \frac{dp}{d\psi} |\xi^\psi|^2 + \frac{\nabla\psi \times \mathbf{J}}{|\nabla\psi|^2} \cdot \nabla \times \mathbf{D} |\xi^\psi|^2 + \Gamma p |\nabla \cdot \xi|^2 \right\} dV \qquad (3.6)$$

where $\mathbf{J} = \nabla \times \mathbf{B}$ is the current density, $\Gamma = 5/3$ is the adiabatic index, p is the plasma pressure, V_P is the plasma volume. The last term in (3.6) describes the plasma compressibility, which makes difference with the incompressible theory, presented in Chapter 2. This term is positively defined and therefore is always stabilizing. The plasma incompressibility condition $\nabla \cdot \xi = \mathbf{0}$ can be imposed by setting $\Gamma = 0$.

The kinetic energy K is given by

$$K = \frac{1}{2} \int_{V_P} \rho_P \left\{ |\xi^\psi|^2 \frac{|\mathbf{D}|^2}{|\mathbf{B}|^2} - 2\xi^\psi \xi^D \frac{\mathbf{D} \cdot \nabla\psi}{|\mathbf{B}|^2} + |\xi^D|^2 \frac{|\nabla\psi|^2}{|\mathbf{B}|^2} + |\xi^B|^2 \frac{1}{|\mathbf{B}|^2} \right\} dV \qquad (3.7)$$

where ρ_P is the plasma density.

In the vacuum region, surrounding the plasma the contribution to the potential energy is

$$\delta W_V = \frac{1}{2} \int_{V_V} |\nabla \times \mathbf{A}|^2 dV \qquad (3.8)$$

where V_V is the vacuum volume and $\mathbf{A}$ is the vector potential of the vacuum magnetic field perturbation $\delta \mathbf{B}_V = \nabla \times \mathbf{A}$. The pseudodisplacement ξ_v is introduced [60, 61] in the vacuum region, such that the perturbed vector potential in vacuum can be represented as

$$\mathbf{A} = \xi_v \times \mathbf{B}_{ps} \qquad (3.9)$$

where $\mathbf{B}_{ps}$ is an artificial magnetic field, which does not coincide with the equilibrium vacuum magnetic field, but ensures the correctness of the representation (3.9). In this case the field $\mathbf{B}_{ps}$ can be represented similarly to (3.3) and the problem for the vacuum region is represented in a way similar to the plasma region, providing the same convergence properties to the whole plasma+vacuum system.

The boundary condition at the ideally conducting wall reads

$$\mathbf{n} \times \mathbf{A} = 0 \qquad (3.10)$$

where $\mathbf{n}$ is the normal vector of the ideally conducting wall surface and at the plasma-vacuum interface it is defined by the tangential electric field continuity condition:

$$\mathbf{n} \times \mathbf{A} = \mathbf{n} \times (\xi \times \mathbf{B}) \qquad (3.11)$$

where $\mathbf{n}$ is the normal vector to the plasma-vacuum boundary. Imposing also the continuity of the total pressure at the plasma-vacuum interface, these equations form the stability problem, solved by the KINX code.

The displacement ξ can be represented as sum of the Fourier modes, corresponding to different toroidal wave numbers n, $\xi_n e^{in\phi}$. In axisymmetric geometry, these modes are decoupled and the stability problem (3.1) becomes a set of separate two-dimensional eigenvalue problems for each ξ_n.

It is important to mention that the code can be implemented in a wide range of plasma geometries, current density and pressure profiles, because the formulation of the stability problem does not set any condition on these parameters. In complicated geometries with separatrix or in presence of several

magnetic axis the whole plasma cross-section is decomposed into a number of nested flux domains, and the stability task is solved separately for each of these domains.

3.1.2 The numerical methods, used in the KINX code.

The code KINX uses the finite elements method. Equation (3.1) is solved by the PAMERA [62] matrix solver. Detailed description of numerical methods is given in [62, 63].

The procedure of eigenvalue computation by the KINX code consists of the following steps:

1. The grid (s, θ) of the size $N_s \times N_\theta$ is set, and the initial displacement ξ with its derivatives is discretized on this grid, forming the column vector z. The hybrid finite elements method [64] is used for this goal. The displacement components ξ^D, ξ^B, ξ^ψ and their derivatives are expanded using different basis functions, so that all terms in the potential energy functional (3.6) are constant in each (s, θ) grid mesh. The equation (3.1) then becomes an eigenvalue equation

$$Az = \lambda Bz \tag{3.12}$$

where A and B are Hermitian matrices of the potential and kinetic energy of displacement normalized to square of Alfven frequency at the magnetic axis ω_a^2 and $\lambda = \omega^2/\omega_a^2$.

2. An initial eigenvalue guess ω_0 is set and the eigenvalue shift

$$\widetilde{W}(\xi^*, \xi) - \omega_0^2 K(\xi^*, \xi) \tag{3.14}$$

is performed. This corresponds to the matrix and eigenvalue shifts $A = A - \lambda_0 B$, $\lambda = \lambda - \lambda_0$. Then (3.12) can be rewritten as

$$\widetilde{A}z = \widetilde{\lambda}Bz \tag{3.14}$$

3. Equation (3.14) is solved by inverse vector iteration [65], using the PAMERA package. The equation (3.14) is rewritten as

$$v^{k+1} = \widetilde{A}^{-1}Bz^k \tag{3.15}$$

where $z^k = \dfrac{v^k}{\left|v^k\right|}$ and the initial guess z^0=1 corresponds to the initial trial displacement.

The iterations (3.15) continue until λ converges to the eigenvalue closest to λ_0 with convergence criterion

$$\Delta\lambda < \varepsilon_{PAM}\left|\lambda_{norm} - \lambda_0\right| \tag{3.16}$$

where $\Delta\lambda$ is the change of λ between iteration steps, λ_{norm} is the normalized eigenvalue, obtained from normalization $\lambda_{norm} = 1/|z|$ and ε_{PAM} equals to 10^{-3} in our calculations.

The eigenvalue is also estimated by the Rayleigh quotient [66]:

$$\lambda_R = \frac{(z^T, Az)}{(z^T, Bz)} \tag{3.17}$$

The difference $|\lambda_R - \lambda_{norm}|$ is a measure of the round-off error by A matrix inversion. The solution ξ is the eigenfunction, corresponding to the eigenvalue λ.

4. The kinetic energy matrix B is positively definite and therefore the Cholesky decomposition [65] can be performed: $B = R^H R$, where R is an upper triangular matrix with positive real diagonal values, and H is the Hermitian operator. With the vector transformation $u=Rz$ one obtains by multiplying the equation (3.14) from the left by $(R^{-1})^H$:

$$(R^{-1})^H \widetilde{A} R^{-1} u = \lambda_u I u \tag{3.18}$$

where $(R^{-1})^H \widetilde{A} R^{-1}$ is the diagonal matrix, consisting of eigenvalues of u, λ_u. According to the Sylvester's law of inertia [67] the number of positive, negative and non-vanishing eigenvalues of $\widetilde{A}$ and $(R^{-1})^H \widetilde{A} R^{-1}$ is the same. Counting the negative entries in the matrix $(R^{-1})^H \widetilde{A} R^{-1}$, one can find the number of solutions more unstable than the initial guess. Thus, changing the initial guess, one can find the largest negative eigenvalue, the most unstable mode. The initial guess is increased gradually from a very negative value towards zero, until the most unstable negative eigenvalue is found or the maximum (closest to zero) preset initial guess value is reached, and the equilibrium is considered as stable.

The code KINX uses as input the Grad-Shafranov equation solution on a quasi-polar grid, which is set by the 2D tensor ρ_{ij}, related to the orthogonal coordinates (R_{ij}, Z_{ij}) by the mapping:

$$R_{ij} = R_{mag} + \rho_{ij}(R_{bound,j} - R_{mag})$$
$$Z_{ij} = Z_{mag} + \rho_{ij}(Z_{bound,j} - Z_{mag})$$

(3.19)

where R_{mag}, Z_{mag} specify the magnetic axis and R_{bound}, Z_{bound} define the plasma boundary. N_s elements of constant i describe magnetic surfaces and N_θ elements of constant j describe straight radial lines. Such equilibrium mapping is produced by the code CAXE [68] which can use the equilibrium, calculated by the CHEASE code [27], as input.
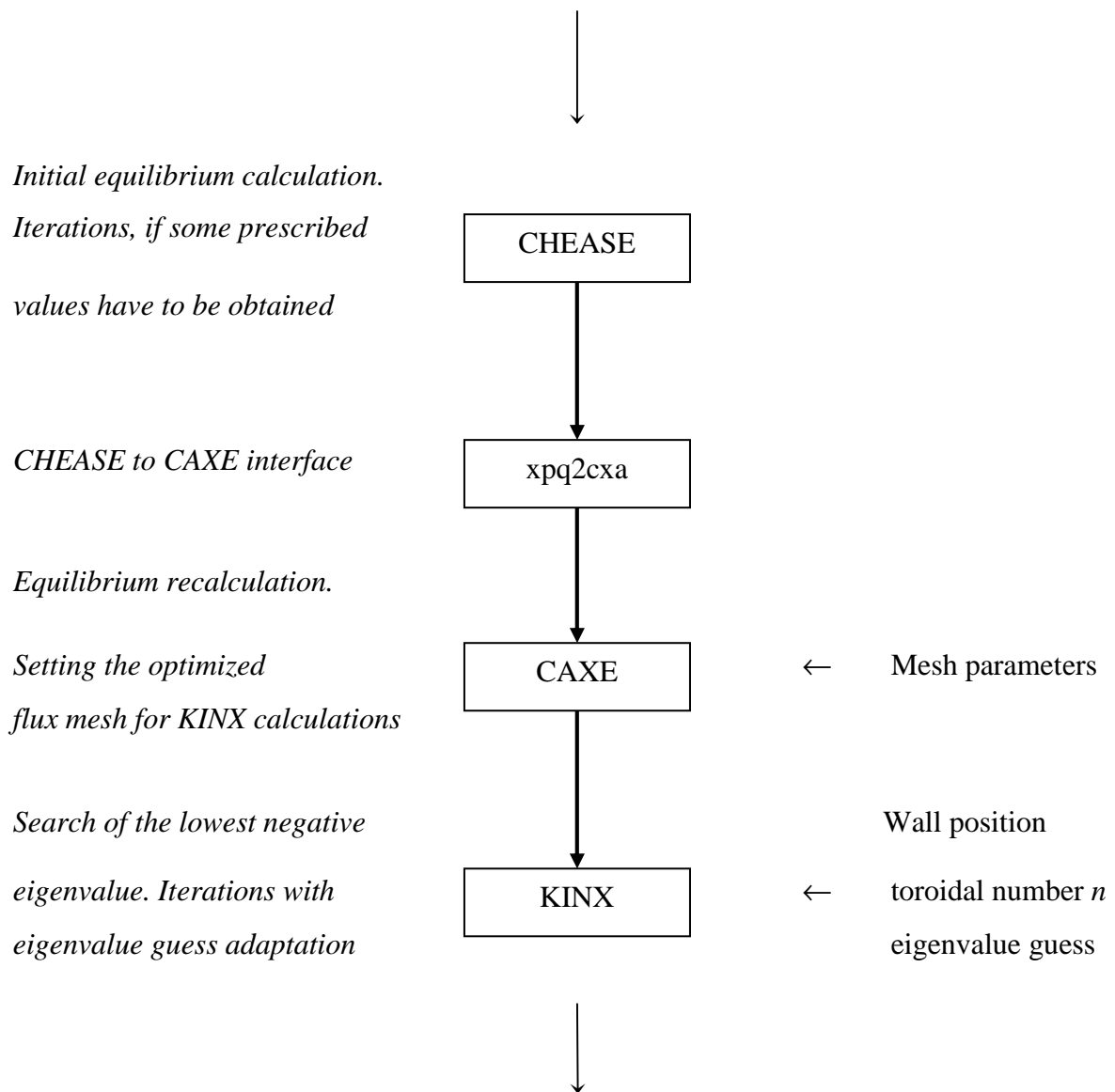
The code benchmarks are described in [53] in comparison with other numerical codes. In our work, a partial benchmarking was also carried out by comparing the growth rates of the ideal internal kink mode, calculated by the KINX code, with analytical results in the low aspect ratio case, where the analytical expansions are justified (see Chapter 4, Section 4.1.3). Good correspondence between analytical predictions and those of KINX in this important particular case confirms the correctness of the problem formulation and of the numerical method used in the code.

3.2 General organization of the calculations

The organization of the calculations is presented in the scheme 3.1. The typical task consists of scanning the plasma parameters like elongation, triangularity, aspect ratio, safety factor and beta for given current density and pressure profiles and, determining of the stability of these configurations in order to outline the influence of these parameters on the plasma stability. Other kind of tasks consisted of the analysis of experimental TCV equilibrium, reconstructed on the basis of TCV experimental measurements by the LIUQE code [69]. In both cases the plasma parameters, either set artificially or taken from the LIUQE equilibrium reconstitution, were used as input data for the CHEASE code. The CHEASE equilibrium after some mapping procedure was used as input for the CAXE code, and then the KINX stability calculations were performed by iteration on the initial guess value.

Perl and Unix shell scripts were written for controlling the plasma parameter scan and the general flow of calculations, according to the scheme 3.1. These scripts collect basic input parameters and the eigenvalue and write them to the output file. These scripts allowed for example the scans of elongation and triangularity for the internal kink mode stability studies (Chapter 4) and the scans of normalized beta and $q_{\min}$ in the studies of the stability of reverse shear plasmas (Chapter 6).

Input : plasma profiles, shape, aspect ratio (arbitrary or from TCV)

Initial equilibrium calculation.

Iterations, if some prescribed

values have to be obtained

| CHEASE |

CHEASE to CAXE interface

| xpq2cxa |

Equilibrium recalculation.

Setting the optimized

flux mesh for KINX calculations

| CAXE | ← Mesh parameters

Search of the lowest negative Wall position

eigenvalue. Iterations with | KINX | ← toroidal number *n*

eigenvalue guess adaptation eigenvalue guess

Output: plasma parameters and the lowest negative eigenvalue, if unstable solution was found, stable otherwise.

Schema 3.1 General calculations flow

The calculations were performed on the IBM pSeries 650 server of CRPP. Typical calculation cycle CHEASE – CAXE – KINX takes 10-30 minutes, depending on the grid sizes and stability of the mode: stable configurations required more computing time, because in this case the initial eigenvalue guess has to pass all the way from initial value to the lowest absolute preset value. In unstable cases iterations were aborted, when the most unstable eigenvalue was found.

Chapter 4. The internal kink mode stability dependence on plasma shape parameters and inverse aspect ratio

In this chapter the numerical studies of the internal ideal kink mode stability are presented and discussed. The dependence of the internal kink growth rate on beta Bussac, aspect ratio, plasma elongation and triangularity, according to the KINX calculations is analyzed in comparison with analytical formulae. The experimental studies of the sawtooth period dependence on plasma triangularity on TCV, inspired by numerical predictions, are presented. An empirical scaling formula is proposed, describing the dependence of the growth rate as obtained by KINX, on basic plasma parameters. Most of the results presented in this chapter can be found in [41].

4.1 Internal ideal kink mode stability: comparison of numerical and analytical predictions.

4.1.1 Important plasma parameters

According to the analytical theory (see equations 2.98 - 2.99), the ideal internal kink mode stability depends on following plasma parameters (the range of variation of these parameters in our simulations is also presented):

- β_{bu}: "beta Bussac", the poloidal beta inside q=1 surface, see equation (2.49); $0 < \beta_{bu} < 2$
- ε_1 : inverse aspect ratio at the $q=1$ surface; $0.001 < \varepsilon_1 < 0.3$
- $\Delta q = 1-q_0$: q_0 being the value of the safety factor on the plasma axis; $0.05 < \Delta q < 0.3$
- s_1: the magnetic shear at the $q = 1$ surface $0.01 < s_1 < 1.4$;
- $e_1 = (\kappa_1-1)/(\kappa_1+1)$ the ellipcity of $q = 1$ surface $-0.1 < e_1 < 0.6$; usually the elongation κ_1 is used instead of e_1, $0.8 < \kappa_1 < 2.2$;
- δ_1 the triangularity of the $q =1$ surface $-0.3 < \delta_1 < 0.3$;
- $\bar{r_1} = r_1\sqrt{\kappa_1}$ and $\bar{a} = a\sqrt{\kappa_a}$ average minor radius of the $q = 1$ surface and the plasma boundary.

It is important to note that the formula (2.98) was obtained assuming parabolic q profile, expressed by (2.80) with $\lambda = 2$ and $r_1/a << 1$. Different shape of $q = 1$ profile will lead to expression for the growth rate different from (2.98). In our numerical calculations, the parabolic profiles as well as other q

profiles were analyzed in order to estimate the role of the q profile shape on the ideal internal kink mode stability.

The above parameters, determining the ideal internal kink mode stability, are internal plasma parameters, i.e. they are defined at the $q = 1$ surface or at the plasma axis. In experimental conditions these parameters are in most cases not measured and not known exactly, but they are reconstituted on the basis of the available experimental measurements. These parameters cannot be controlled directly. On the contrary, the external plasma parameters are well known, because they can be directly measured and controlled.

To be able to compare our numerical results with the experimental data and to study the role of these external parameters, we have also saved these parameters with the growth rate in the output file:

- β_p the total poloidal beta $0 < \beta_p < 1$;

- ε_a : inverse aspect ratio on the plasma boundary $0.012 < \varepsilon_a < 0.8$;

- $e_a = (\kappa_a\text{-}1)/(\kappa_a\text{+}1)$ the ellipcity of the plasma boundary; usually the plasma edge elongation was used, $1.0 < \kappa_a < 3.0$;

- δ_a the triangularity of the plasma boundary $-1.0 < \delta_a < 1.0$;

- q_a the edge plasma safety factor $2.2 < q_a < 100$ (in some exotic cases);

The role of these parameters was studied with an emphasis on those that can be controlled in experimental conditions: edge aspect ratio ε_a, edge safety factor q_a or the total plasma current I_p, current density profile, plasma boundary elongation κ_a and triangularity δ_a. These parameters determine the plasma equilibrium and, consequently, the values of other parameters.

It is important to mention that while the input parameters of the plasma equilibrium can be changed independently, corresponding variations of the output parameters are correlated. For example, at constant edge plasma triangularity the value of δ_1 evolves with elongation, and so does the value of shear at $q = 1$ surface, the aspect ratio at $q = 1$ surface and other parameters. Therefore, this contrasts with the analytical approach described in Chapter 2 where the role of each parameter can be analyzed independently. The latter is evidently less representative of experimental conditions.

4.1.2 The dependence on β_{bu}

The "beta Bussac", β_{bu}, is the most important value determining the ideal internal kink mode stability. According to the analytical formula (2.34), the increase of β_{bu} causes the increase of the destabilizing

effect of toroidicity, so the growth rate becomes more unstable with β_{bu}. If the mode is stable at low β_{bu}, it is destabilized at higher β_{bu}. The value of β_{bu}, at which the mode becomes unstable, is called the critical beta Bussac and is denoted as β_{bu}^{crit}. The mode can also be unstable at low or even at zero β_{bu} – usually in cases of high plasma elongation. Zero β_{bu} means, according to the definition (2.49), that either the pressure profile is flat inside $q = 1$ surface or the plasma pressure equals to zero.

The dependence of the ideal internal kink mode growth rate on β_{bu} was studied for different plasma configurations. Some examples of this dependence are shown in Figure 4.1.
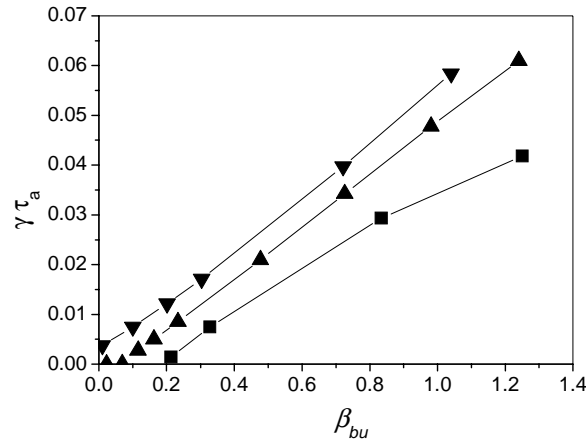
Figure 4.1 Different kinds of dependence of the ideal internal kink mode growth rate on β_{bu}: β_{bu}^{crit} is negative (downward triangles), β_{bu}^{crit} is slightly positive (upward triangles), $\beta_{bu}^{crit} \sim 0.2$ (squares). The dependence on β_{bu} is essentially linear for β_{bu} of interest.

It was found that this dependence can be well described by the following formula

$$\gamma \tau_a = A(\beta_{bu} - \beta_{bu}^{crit})^C \tag{4.1}$$

The correspondence between this formula and the calculated growth rates is shown in Figure 4.2. The formula (4.1) is a significant simplification – as compared to (2.98), for example. Evidently, this formula outlines the leading term in the dependence, which generally is more complicated. But from a practical purpose it is very convenient (and sometimes more accurate) to analyze the elements A, β_{bu}^{crit} and C of the simple formula (4.1), because such analysis can give important information on the mode stability.
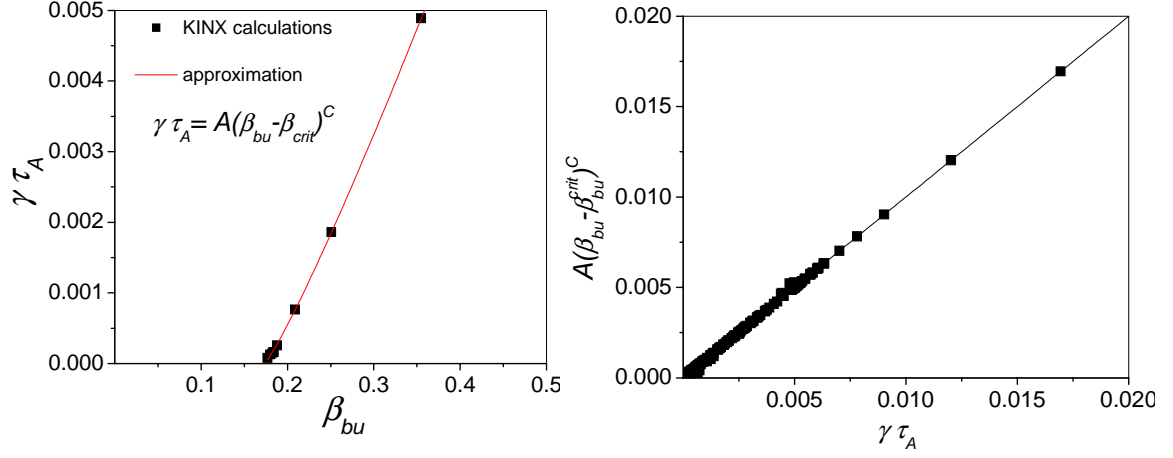
Figure 4.2 a) An example of the growth rate dependence on β_{bu} and of the corresponding approximation by the formula (4.1); b) The correspondence of the whole set of the calculated growth rates and of the formula (4.1), with different A, β_{bu}^{crit}, C for each β_{bu} scan.

4.1.3 The inverse aspect ratio.

The inverse aspect ratio at the $q = 1$ surface, ε_l, is one of the most important values in the analytical theory of the ideal internal kink stability. Usually it is considered as a small parameter, $\varepsilon_l << 1$, and the potential energy variation is expanded in terms of ε_l (see Section 2.4.1). In our numerical simulations we have looked at high values of ε_l, corresponding to realistic geometries of TCV and tight aspect ratio tokamaks, like MAST, where $\varepsilon_l \sim 0.1 - 0.3$. It turns out that such ε_l can not be considered as a small parameter anymore. It is interesting to compare the numerical and analytical predictions for different values of ε_l and thus to determine the validity region of the analytic approach. Such comparison is presented in Figure 4.3 for parabolic current profile, corresponding to the profile used for (2.98).

It can be seen in Figure 4.3, that at the lowest $\varepsilon_a = 0.012$ the KINX results correspond well to the analytical ones, especially in the case of circular cross-section and at moderate elongation. Up to $\varepsilon_a = 0.28$ ($\varepsilon_l \sim 0.1$) this correspondence remains good. This is assisted by the form of the δW_{ε^2} term (2.98), taking into account the volume effect in the effective minor radius. At high elongation ($\kappa_a \sim 2.0$), however, this correction is too strong and analytical predictions are different from numerical ones for most values of ε_a. At larger β_{bu}, corresponding to higher growth rates, the analytical predictions roll over and the difference between them and numerical calculations becomes significant. This saturation is caused by the stabilizing term δW_{ε^4} and by the term $\delta W_{\varepsilon^2 e}$ which become too stabilizing at large β_{bu} and ε. Note however that these cases are beyond the expected range of validity of Eq. (2.98): $\varepsilon_l \leq \sim 0.1$, $\kappa_l \leq \sim 1.4$, and beyond these limits the overstabilizing term δW_{ε^4} may not be applied.
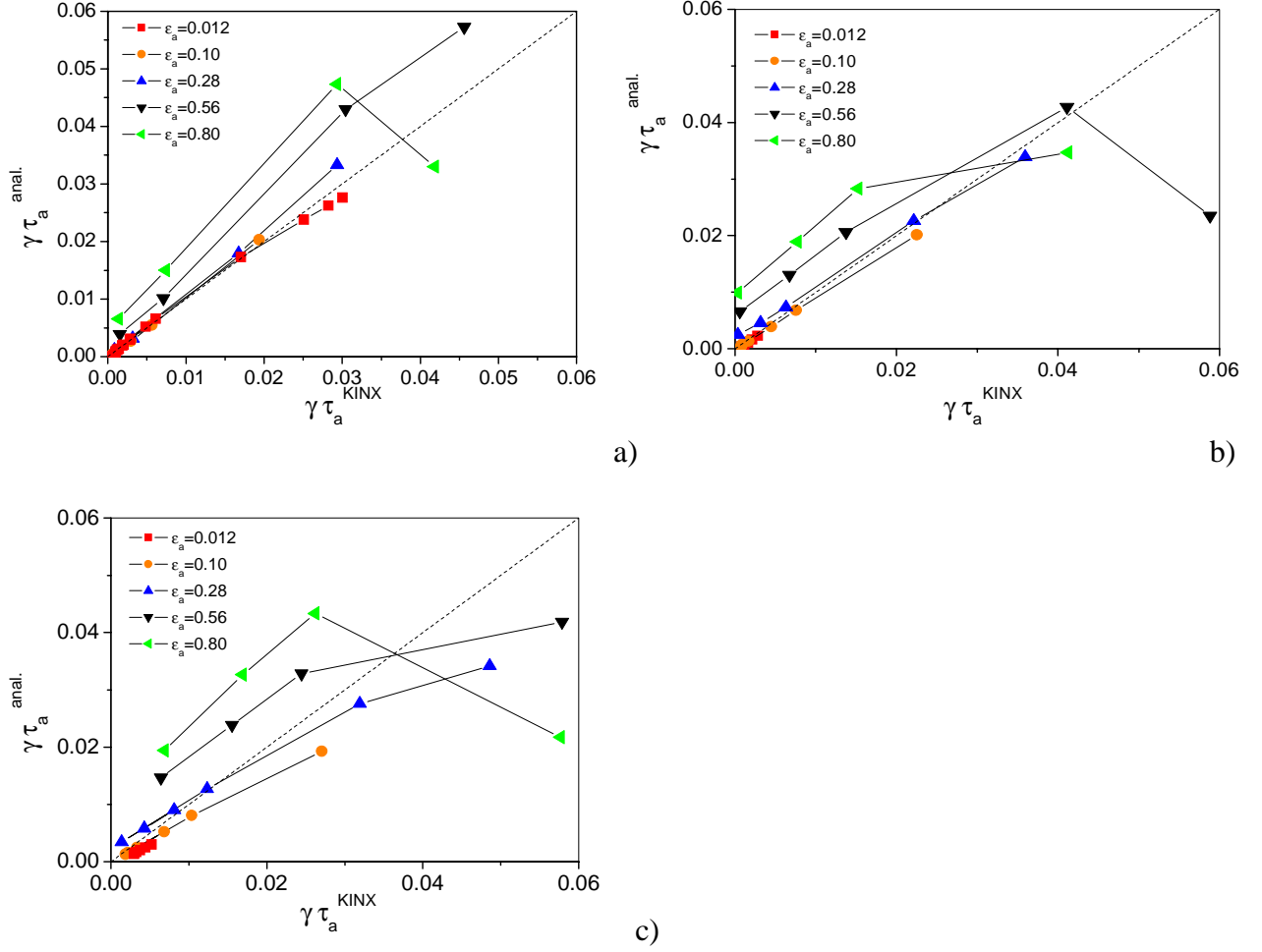
Figure 4.3 The internal ideal kink mode growth rate, calculated with the analytic formula (2.98) at different inverse aspect ratios and β_{bu}, compared with corresponding KINX results for a) circular plasma cross-section and for b) $\kappa_a=1.4$ and c) $\kappa_a=2.0$

The aspect ratio influences the dependence of the growth rate on β_{bu}. In Figure 4.4 analytical and numerical calculations are presented for $\varepsilon_a = 0.28$ ($\varepsilon_l \sim 0.1$) and $\varepsilon_a = 0.8$($\varepsilon_l \sim 0.2$). The character of this dependence varies with aspect ratio: at high ε_a the dependence has the tendency to roll over, while at lower ε_a the dependence is constantly increasing. The values of β_{bu}^{crit} are not so dependent on the inverse aspect ratio and stay approximatively the same. The analytical predictions are substantially higher than the numerical predictions in the case of $\varepsilon_a = 0.8$. The roll over of the analytical formula which has been seen already in Figure 4.3, can occur at relatively low β_{bu} for high values of $\hat{\varepsilon}_1$, in particular for high κ. This is mainly due to the δW_{ε^4} term, which should not be applied at these values of $\hat{\varepsilon}_1$.

a)   b)
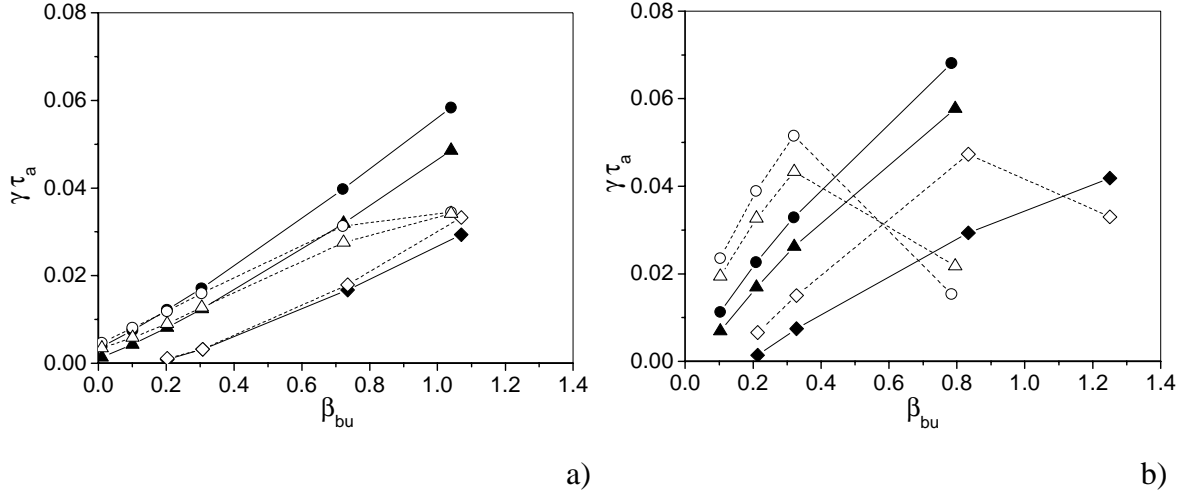
Figure 4.4 The internal ideal kink growth rate versus β_{bu} for different plasma elongations and parabolic q profile at a) $\varepsilon_a = 0.28$ and b) $\varepsilon_a = 0.8$. Open symbols correspond to analytical prediction (2.98), solid symbols are KINX calculations. Shown are $\kappa_a=1$ (diamonds), $\kappa_a=2.0$ (up triangles) and $\kappa_a=2.6$ (circles).

The role of the inverse aspect ratio can also be seen on the dependence of the coefficient C of the scaling (4.1) on ε_a, presented on the Figure 4.5.

a)   b)
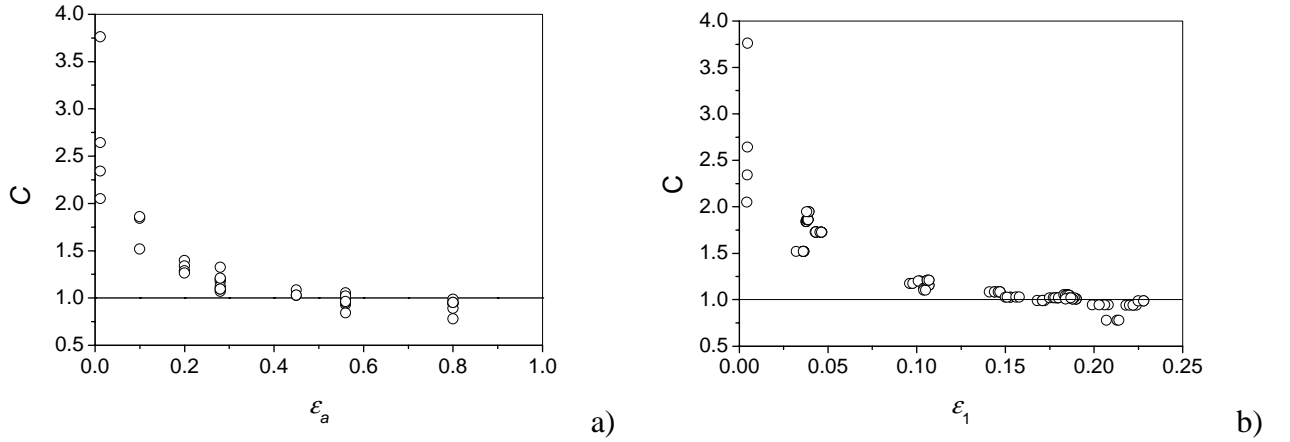
Figure 4.5 Dependence of the coefficient C on a) ε_a and b) on ε_1

The coefficient C decreases with ε_a, going from values ≥ 2 at low ε_a as expected from analytical predictions to 1 and below 1 at high ε_a. This corresponds to the results shown in Figure 4.4, more convex for small ε_a ($\gamma\tau_a'' > 0$) and concave for large ε_a ($\gamma' < 0$). Thus, in the case of high ε_a, it is not legitimate to use the usual analytical approach, $\gamma\tau_a \propto (\beta_{bu}^2 - \beta_{bu}^{crit\,2})$[9]. Instead, the approximation $\gamma\tau_a \propto (\beta_{bu} - \beta_{bu}^{crit})$ looks more reasonable for high ε_a values, corresponding to modern tokamaks like TCV or MAST.

4.1.4 The plasma elongation.

The plasma elongation is the most important shape factor influencing the internal kink mode stability. It modifies mainly the critical beta Bussac, as it can be seen in Figure 4.4, where the dependence of the growth rate on β_{bu} at different elongations and inverse aspect ratios is shown. The plasma elongation is a strong destabilizing factor, and it is expressed in the decrease of β_{bu}^{crit} with elongation, as seen in Figure 4.6. When β_{bu}^{crit} becomes negative, it signifies that the internal ideal kink mode is unstable at $\beta_{bu} = 0$ (as mentioned before this means a flat pressure profile). For finite ε_a values, $\beta_{bu}^{crit} \sim 0$ typically at $\kappa_a \geq 1.6$.
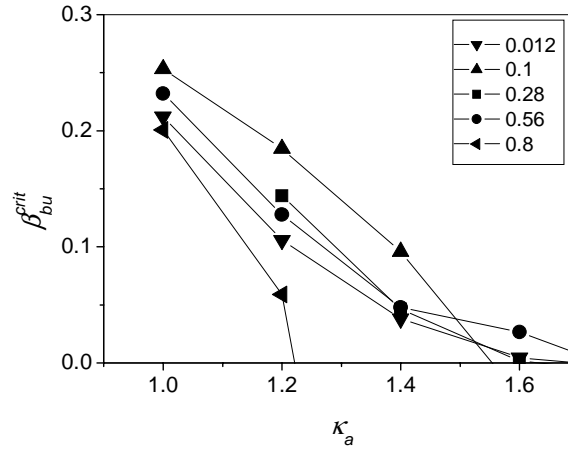
Figure 4.6 The dependence of β_{bu}^{crit} on the plasma elongation at different inverse aspect ratios.

4.1.5 The plasma triangularity.

The influence of triangularity on the internal kink mode growth rate is illustrated in Figure 4.7. The trend, discussed in Section 2.4.4 (Figure 2.7) is reproduced qualitatively on these plots: the growth rate decreases with increasing triangularity, both positive and negative, with the maximum growth rate shifted at negative triangularity. The effects of elongation and triangularity on β_{bu}^{crit} can be seen simultaneously in Figure 4.8 [70] as obtained with the KINX code over a wide range of κ and δ. Note that at $k_a=1$ the dependence on δ_a is different from the dependence at higher elongation. This is because the Mercier term $\delta W_{\varepsilon e \delta}$ equals to zero for circular plasma shape.

The stabilizing effect of the negative triangularity was reported in [70, 71] in the initial stage of the present work and has motivated a series of experiments on the TCV tokamak, presented in the next Section. The effect can be partially understood examining the quasi-cylindrical term δW_{δ^2} in (2.98) which is clearly stabilizing for positive and negative δ.
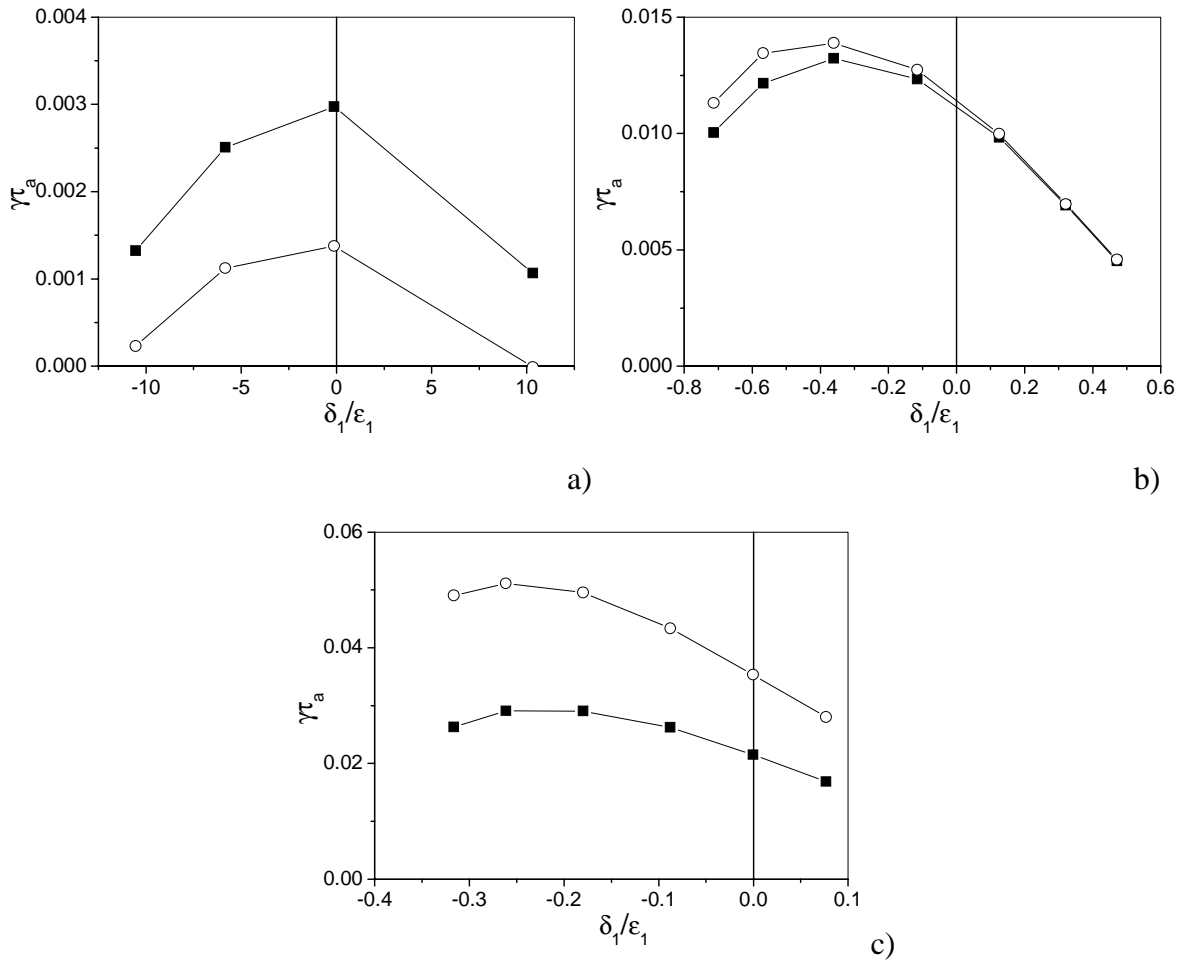
a)

b)

c)

Figure 4.7 The ideal internal kink growth rate versus triangularity by KINX calculations (solid squares) and according to equation (2.98) (open circles) for $\kappa_a = 1.7$, $\beta_{bu} = 0.35$ and a) $\varepsilon_a = 0.012$, b) $\varepsilon_a = 0.28$, c) $\varepsilon_a = 0.8$
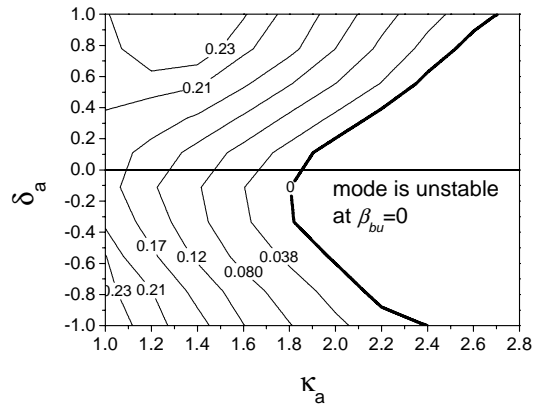

Figure 4.8 The dependence of β_{bu}^{crit} on plasma elongation and triangularity.

4.2 Experimental studies on the TCV tokamak

4.2.1 The TCV tokamak

The TCV tokamak at CRPP in Lausanne, Switzerland was designed especially for studies related to the shaping effects [72, 73, 74]. The design of this tokamak allows control of plasmas with various shapes, and even allows changing the plasma shape and position during shots. In Figure 4.9, some plasma shapes obtained on the TCV tokamak are presented.
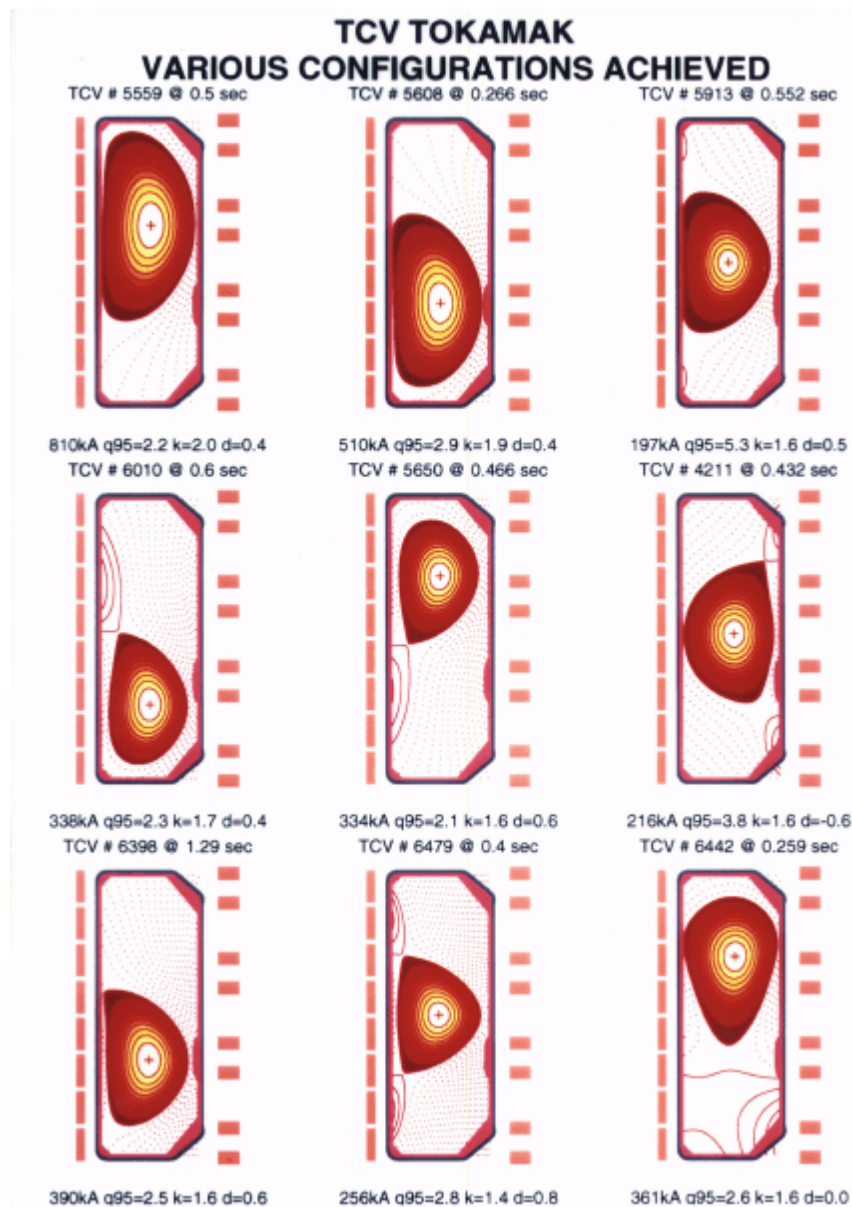
Figure 4.9 Some examples of plasma shapes obtained on the TCV tokamak

The main parameters of the TCV tokamak are:

- Major radius $R = 0.9$ m
- Minor radius $a = 0.25$ m
- Toroidal field $B_t = 1.5$ T
- Plasma current I_p up to 1 MA
- Elongation κ_a up to 2.8
- Triangularity δ_a between –0.7 and +0.9
- Aspect ratio $A = 3.6$
- Inverse aspect ratio $\varepsilon_a = 0.28$. ε_1 up to $0.15 - 0.2$ have been obtained.

The unique flexibility of the TCV tokamak makes it the best machine for the studies of the dependence of the internal kink mode stability on plasma triangularity. The growth rate of the ideal internal kink mode can not be measured directly, so in experimental studies other phenomena which are presumably triggered by this mode are studied: the sawtooth oscillations and in particular the sawtooth period. Another very important feature of the TCV tokamak is its very powerful and flexible electron-cyclotron plasma heating and current drive system. Six launchers on the low field (external) side of the tokamak, independently controlled in toroidal and poloidal directions, can inject into the plasma each up to 450 kW of power at the frequency of 82.7 GHz (second harmonics of the electron-cyclotron resonance at 1.4T). Added to this from the top of the tokamak is 1.14 MW of the EC-power on the 3rd electron-cyclotron resonance harmonics (118 GHz). Using this system, arbitrary configurations of the power deposition and current drive can be created in the TCV plasmas.

4.2.2 Sawtooth oscillations and the internal ideal kink mode.

Sawtooth oscillations were discovered in 1974 on the ST tokamak [75]. These are periodic relaxation oscillations of temperature and density in the plasma center. The sawtooth oscillations are best seen on the traces of the soft X-ray emission from the plasma center. A typical sawtooth trace is presented in Figure 4.10.
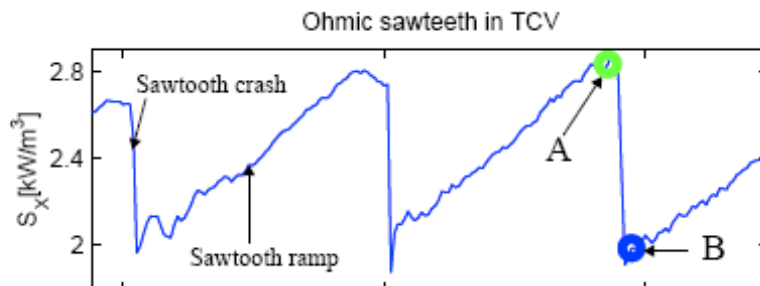

Figure 4.10 An example of the sawtooth oscillations in the TCV tokamak. Central soft X-ray trace. A is at the top of the sawtooth crash, B is the end of the crash and the beginning of the slow ramp-up phase

A sawtooth crash is the fast drop of central temperature and density which occurs when $q_0 < 1$. At this moment a fast instability process displaces the hot central part of the plasma out to the plasma periphery. After the crash the q value on the plasma axis can be above 1. Then the plasma is slowly recovering the initial profile, increasing the density and temperature at the plasma center, until the crash condition is met again and a new crash occurs. The condition $q_0 < 1$ is necessary, but not sufficient for the sawtooth crash. The plasma has to accumulate enough energy within the $q = 1$ surface to trigger the instability mechanisms, causing the crash.

Several theoretical models were proposed for the explanation of the sawtooth crash mechanism and of the crash trigger conditions, for example [9, 44, 76, 77]. Although there is no complete agreement about this question, there is evidence that the $m/n=1/1$ MHD mode has a direct relation with the causes of the sawtooth crash.

The sawtooth crash model, proposed in [9], relates the sawtooth crash occurrence with the development of the ideal or resistive internal kink mode. The sawtooth crash occurs when the kink mode growth rate overcomes the stabilizing ion and electron diamagnetic effects. Thus, in the situations where the ideal kink mode growth rate is higher than half of the ion diamagnetic frequency, the value of the ideal internal kink growth rate has a direct influence on the sawtooth crash conditions [9]: the higher is the growth rate, the sooner the sawtooth crash occurs and the shorter is the sawtooth oscillation period, which is easily measured by the soft X-ray emission traces. Thus, the sawtooth oscillations can presumably be used for analysis of the ideal internal kink mode growth rate dependence on the plasma shape.

4.2.3 The TCV experiments

First experimental studies of the dependence of the sawtooth behavior on plasma shape on the TCV tokamak [78, 79, 80] were performed in 1999 and their results are presented in Figure 4.11.

These results confirm the trends discussed in the previous Section: the increase of the sawtooth period, corresponding to a decrease of the kink mode growth rate, occurs when triangularity increases (Figure 4.11 a). The sawtooth period decreases with elongation, and this corresponds to an increase of the growth rate of the mode (Figure 4.11 b).

When these experiments were performed, the fact that the negative triangularity has a stabilizing effect on the ideal internal kink mode was not yet realized, so the negative triangularity was really not explored.
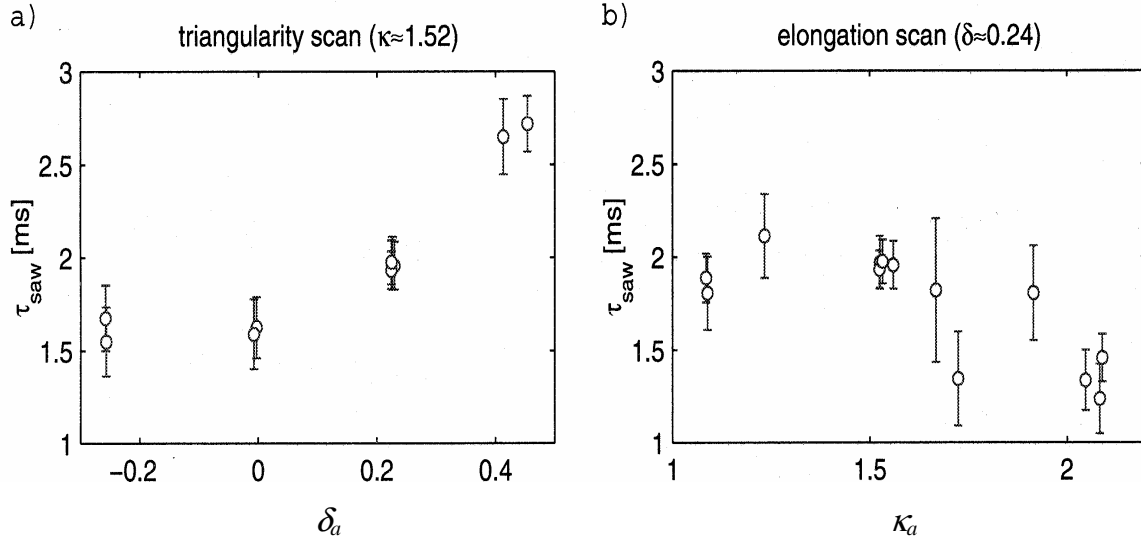
Figure 4.11 The sawtooth oscillations period dependence on plasma shape parameters. Ohmic discharges, results averaged over the stationary phase.

A new series of experiments was performed in September - October 2003, and now the attention has been focused on the negative triangularity region. The edge triangularity δ_a was modified between -0.6 and 0.3, thus the triangularity at $q = 1$ was between -0.1 and 0.06. Two sets of experiments were carried out. In the first set the total plasma current was kept fixed, and in the second set the q_{95} value was fixed in order to keep the $q = 1$ radius nearly constant [81]. Only a few shots have been performed in the second set because of difficulties with obtaining the required plasmas. Therefore the results of the first set will be mainly discussed here.

The first set of experiments was carried out at the following plasma parameters: $\kappa_a \approx 1.5$, $I_p \approx 280$ kA, $r_1/a \approx 0.4$. There are no current density profile measurements in the TCV tokamak, so the q profile shape, s_1 and Δq are not well known. The reconstruction of the experimental equilibria was carried out using the LIUQE code [69], yielding $\Delta q \approx 0.2$, $s_1 \approx 0.5 - 1$. The value of q_{95} was between 2.8 and 3.6 in these shots. The scenarios were typical for ohmic L-mode plasmas.

The dependence of the sawtooth period on edge triangularity is shown in Figure 4.12. It is known from experiments [82] that the sawtooth period in ohmic plasmas is in general linearly proportional to the plasma density. Some theoretical models were proposed that explain this feature [83] and it was also recovered in transport simulations using a sawtooth trigger model [84]. The normalization of the sawtooth oscillation period is a standard procedure used in the TCV experimental studies in order to compensate the influence of the plasma density on the sawtooth period:

$$\tau_{saw}^{normalized} = \frac{\tau_{saw}}{\overline{n}_e[10^{19}\,\mathrm{m}^{-3}]} \tag{4.2}$$

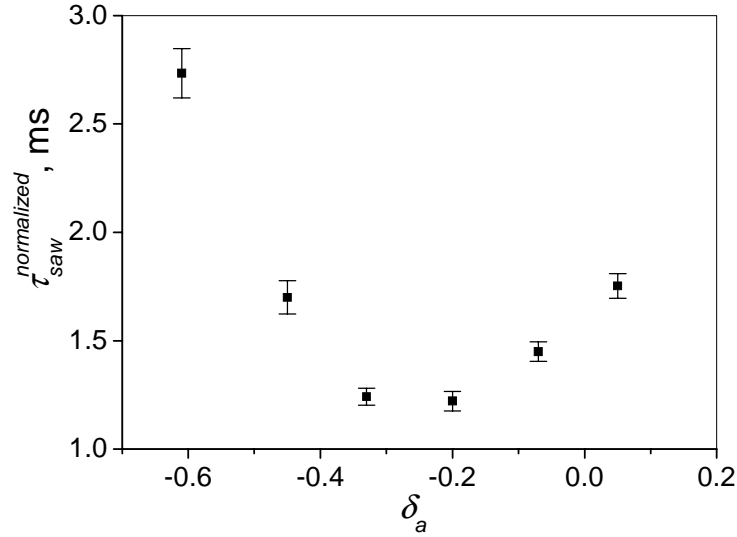where $\overline{n}_e$ is the line-averaged electron density, obtained by the laser interferometer.

Figure 4.12 The sawtooth oscillation period normalized as in Equation (4.2), averaged over the steady-state discharge phase versus edge triangularity in TCV experiments with $I_p \approx 280$ kA.

This normalization is confirmed in TCV for different elongations (κ_a = 1.6 - 2.2), at similar measured inversion radii (r_{inv}= 0.40 - 0.45) for densities ranging from $2 \cdot 10^{19}$ to $5 \cdot 10^{19}$ m^{-3}.

The minimum of the sawtooth oscillation period in Figure 4.12, corresponds to the maximum of the ideal internal kink growth rate versus triangularity for TCV conditions (Figures 4.7b, 4.8) at $\kappa_l \approx 1.3$. The ideal kink growth rates were calculated using the experimental equilibria of the discharges shown in Figure 4.12 and the result is presented in Figure 4.13. The analytical predictions, according to equation (2.98), are also presented. The contributions of different terms of this equation are also shown in order to clarify the role of these terms.

The maximum of the ideal kink mode growth rate is observed in the KINX results, but slightly less clearly on the analytical formula predictions. This is because, as it was mentioned above, not only the shape changes with triangularity but other plasma parameters, like pressure and current profiles, are also modified [85] in the self-consistent equilibrium solutions based on experimental data. For example, the shear at q =1 changes between 0.5 and 0.8 in these equilibria (Figure 4.14), although it is relatively constant for δ_a > -0.5. It is important to note, however, that in the absence of q profile measurements, the equilibrium reconstructions can give only approximate results. In these L-mode ohmic plasmas, though, this reconstruction should be relatively accurate.
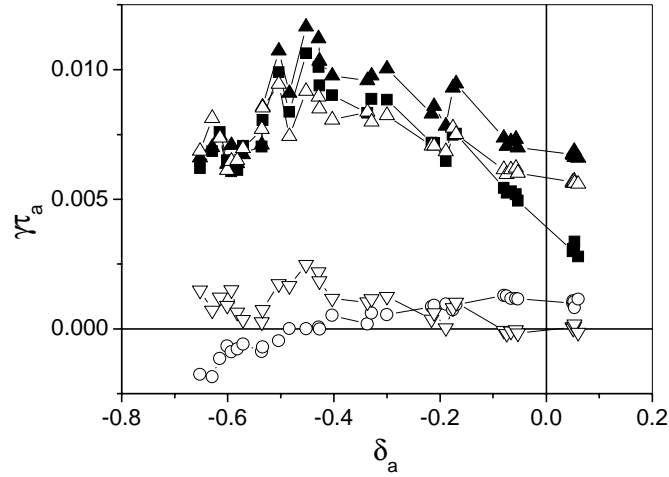
Figure 4.13 Normalized growth rate $\gamma\tau_a$ of the ideal internal kink for the discharges shown in Fig. 4.12. The following results are shown: KINX calculations (solid squares), analytical predictions, according to equation (2.98) (solid triangles) and its contributing terms: toroidal terms $\delta W_{\varepsilon^2} + \delta W_{\varepsilon^4}$ (downwards open triangles), quasi-cylindrical terms $\delta W_{e^2} + \delta W_{\delta^2}$ (open circles), Mercier terms, $\delta W_{\varepsilon^2 e} + \delta W_{\varepsilon e \delta}$ (upwards open triangles).
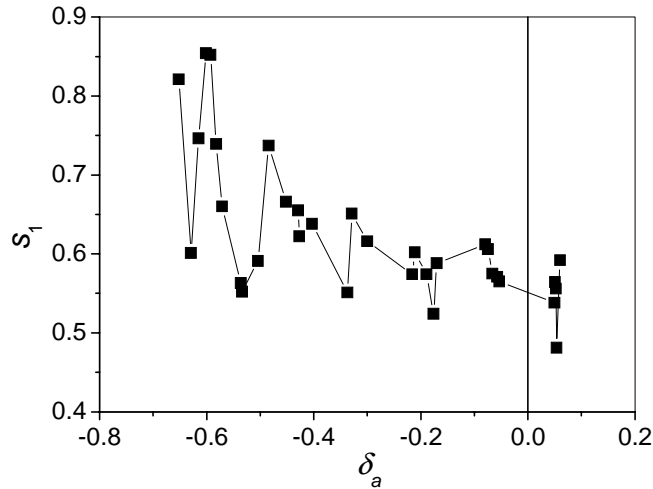
Figure 4.14 Variations of the magnetic shear at q = 1 in the reconstructed equilibria, for the shots, shown on the Figure 4.12

In the second set of experiments only 3 shots were performed, because it proved to be very difficult to create plasmas with negative triangularity and the required parameters. The normalized sawtooth period in these shots is presented in Figure 4.15. We see that a similar dependence is obtained for these discharges as well.
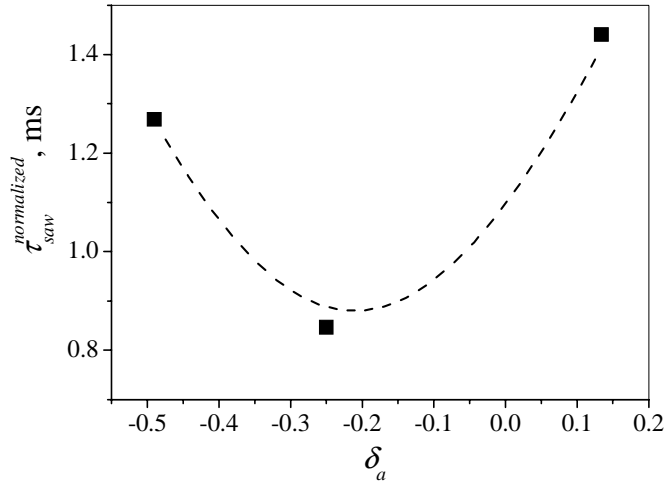
54

Figure 4.15 The normalized sawtooth period versus edge triangularity for the second set of shots with fixed $q_{95} \approx 2.4$. I_p = 405, 414, 395 kA for shots with δ_a = -0.5, -0.25, 0.14 respectively.

The qualitative agreement between the sawtooth period dependence on the plasma triangularity with the behavior of the ideal internal kink growth rate could be a coincidence. The ideal internal kink can be stabilized by diamagnetic effects, when $\gamma < 0.5\omega_{*i}$ [9]. In our cases $\gamma \approx 0.5\omega_{*i}$, but in scenarios with positive triangularity in the TCV tokamak the ideal growth rate is usually lower than $0.5\omega_{*i}$. In these cases the sawtooth crash is triggered by the onset of the resistive kink mode, for which two formulas are used, depending on the regime [9, 86, 87]. It is important to estimate the resistive kink growth rate in order to check whether it can trigger the sawtooth crash in our cases as well. The estimations of these two formulas are given in Figure 4.16.
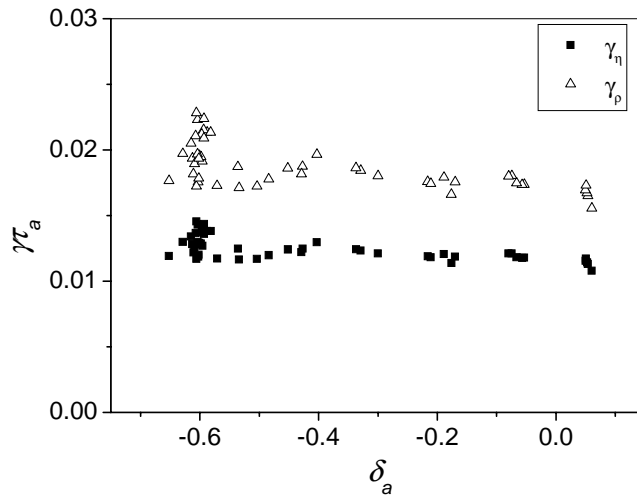

Figure 4.16 Resistive internal kink mode growth rates, estimated in two ways, for the regimes, usually relevant for TCV [83]

There is no evident dependence on the plasma triangularity, so the resistive kink mode cannot explain the observed experimental dependence of sawtooth period on triangularity.

On the contrary, the remarkable correspondence between the behavior of the ideal internal kink mode growth rate and the sawtooth period allows us to conclude that the sawtooth crash is triggered by the ideal internal kink mode in our experiments. It is seen from Figure 4.13 that increasing triangularity to positive values leads to a rapid decrease of $\gamma\tau_a$, according to KINX calculations. Thus, at positive triangularity, usual in many present experiments, the ideal internal kink mode growth rate is too small to be able to trigger the sawteeth and instead of the ideal mode, the resistive kink mode triggers the sawtooth crash.

4.3 Shape, aspect ratio and pressure scaling of the ideal internal kink growth rate

4.3.1 General considerations

The utility of an empirical fit of the numerical data can be seen from the evident discrepancies between the analytical predictions and the numerical calculations, demonstrated in Figures. 4.3, 4.4, 4.7. As it was also shown in the previous Section, the numerical predictions correspond qualitatively better to the experimental results than analytical results. But the numerical calculations are time-consuming and in many cases the time required for the ideal MHD code to run is too long for the task to solve. For example, in the simulations of sawtooth oscillations by transport codes like PRETOR [88] and ASTRA [89] the sawtooth crash trigger condition includes the ideal kink mode growth rate. However it is not possible to wait a few minutes for the ideal MHD code to run at each time step, because the simulations of time evolution require usually tens of thousands of time steps. For such kind of tasks a fit of numerical results can be useful, and simple formula can be used for estimating the ideal internal kink mode growth rate instead of long computations.

The scaling has been built on the basis of the approximation (4.1). The practical modification to this formula was done using the dependence of the coefficient C on the inverse aspect ratio (Figure 4.5), where it can be seen that at ε_a of interest for us ($\varepsilon_a > 0.2$), C is close to 1. Therefore this coefficient was fixed to $C = 1$ for simplicity and the scaling formula is chosen as

$$\gamma\tau_a^{fit} = A(\beta_{bu} - \beta_{bu}^{crit})$$

(4.3)

where for coefficients A and β_{bu}^{crit} separate scalings are constructed and then they are joined to form the resulting formula.

4.3.2 The scaling for the critical beta Bussac β_{bu}^{crit}

The dependence of β_{bu}^{crit} on $\varepsilon_1/\varepsilon_a$ and κ_1 is presented in Figure 4.17. It shows a small decrease of β_{bu}^{crit} with increasing values of $\varepsilon_1/\varepsilon_a$, which has motivated the correction to the term δW_{ε^2}, proposed in [9], equation (2.93). The latter also includes a small dependence on $\sqrt{\kappa_1/\kappa_a}$ since $\bar{r}_1/\bar{a} = \varepsilon_1/\varepsilon_a\sqrt{\kappa_1/\kappa_a}$.
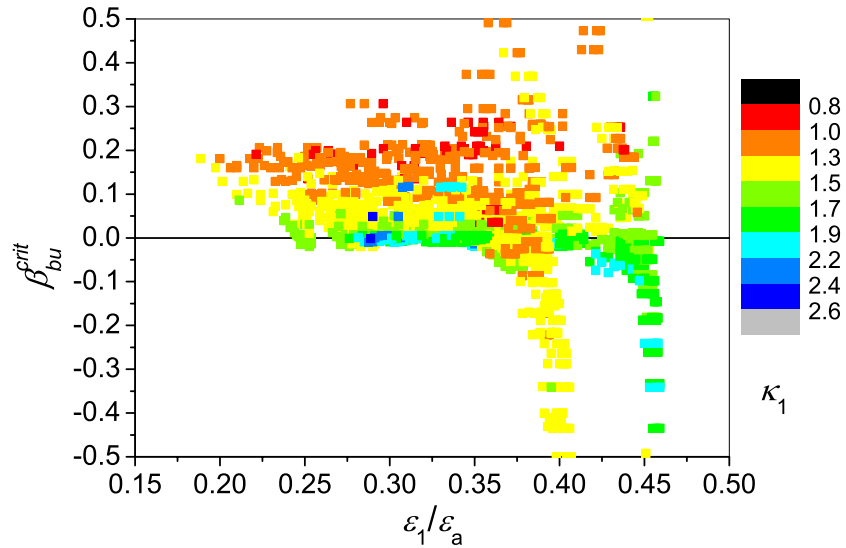
Figure 4.17 Dependence of the critical beta Bussac β_{bu}^{crit} , obtained from fitting the numerical results, on κ_1 and $\varepsilon_1/\varepsilon_a$.

Another kind of approximation for β_{bu}^{crit} was proposed in [71], describing the dependence on plasma elongation and triangularity, presented in Figures. 4.6, 4.7, 4.8 and 4.17:

$$\beta_{bu}^{crit} \approx 0.5 - \frac{\varepsilon_1}{\varepsilon_a}(\kappa_1 - 1.5|\delta_1 + 0.04|) \tag{4.4}$$

However, Figure 4.17 shows that the main dependence is clearly on the value of κ_1. In order to simplify as much as possible the formula, an even simpler expression was chosen, which describes this main feature of β_{bu}^{crit} , the dependence on κ_1 (the validity of this choice will be discussed later):

$$\beta_{bu}^{crit} \approx 0.7 - 0.5\kappa_1 \tag{4.5}$$

This reproduces the color coded horizontal lines in Figure 4.17 with $\beta_{bu}^{crit} = 0.2$ for $\kappa_1 = 1$ and $\beta_{bu}^{crit} \approx 0$ for $\kappa_1 = 1.4$. The latter is consistent with the results shown in Figure 4.6 that the value of κ_1, such that $\beta_{bu}^{crit} = 0$, does not depend much on ε, except at very small ε.

4.3.2 The scaling for the coefficient A

The coefficient A depends mainly on ε_1, as presented in Figure 4.18.
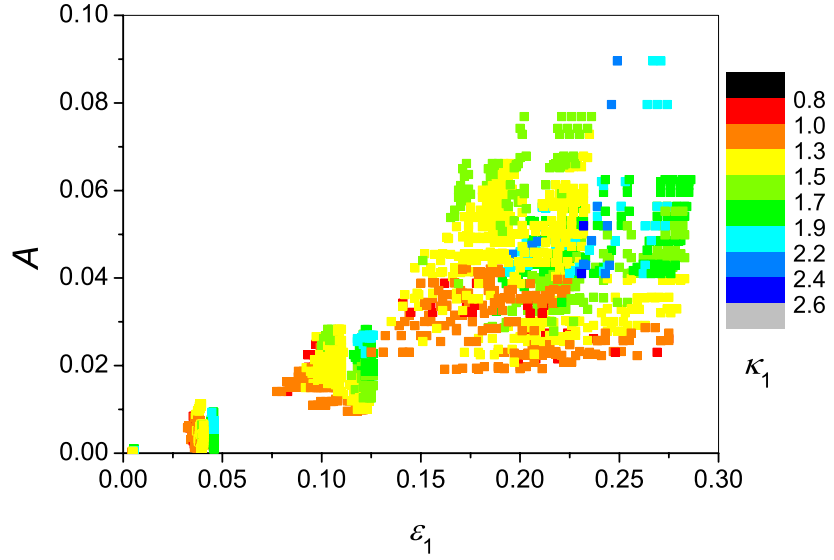
Figure 4.18 Dependence of the coefficient A on κ_1 and ε_1.

In Ref. [71] we have proposed the following approximation for A:

$$A \approx 0.5\varepsilon_1(\kappa_1 - 0.5) \tag{4.6}$$

However, when combining equations (4.5) and (4.6) to fit the actual growth rates calculated by KINX, a better fit is obtained using:

$$A \approx 0.45\frac{\varepsilon_1\kappa_1}{1+0.7\varepsilon_1 s_1} \tag{4.7}$$

4.3.3 The general scaling for $\gamma\tau_a$

Expressions (4.5) and (4.7), combined to the single formula (4.3), give

$$\gamma\tau_a^{fit} = 0.45\frac{\varepsilon_1\kappa_1}{1+0.7\varepsilon_1 s_1}\left[\beta_{bu}-(0.7-0.5\kappa_1)\right] \tag{4.8}$$

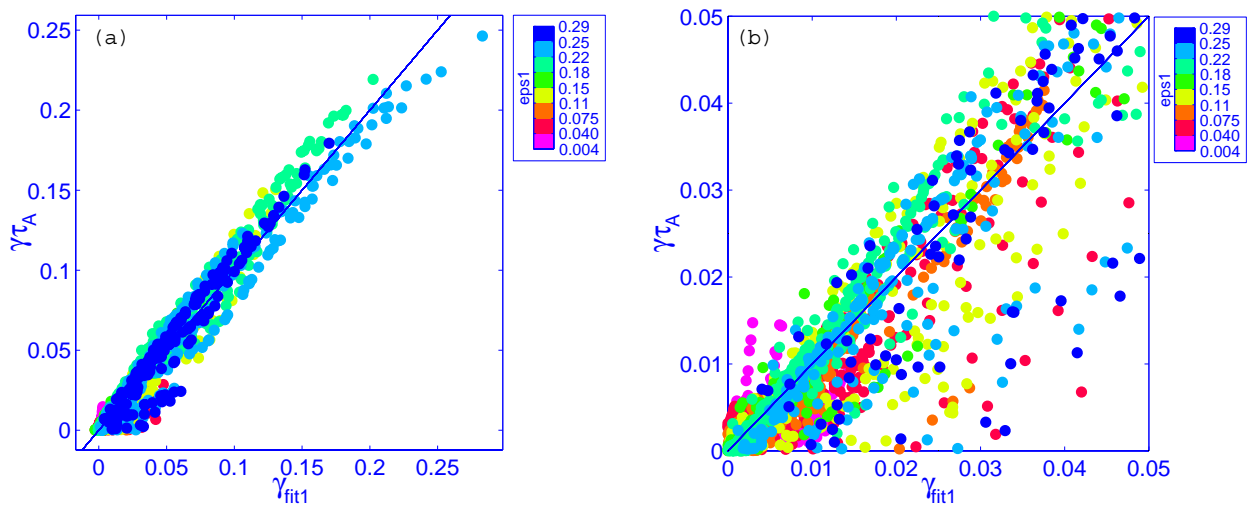The Figure 4.19 compares the fit with the whole set of the calculated data.

Figure 4.19 a) Global scaling obtained from fitting the numerical KINX results for the ideal internal kink versus the KINX results, b) Zoom of the scaling for $\gamma\tau_a\leq0.05$.

About 300 equilibria were used for the fitting, with the following parameter limits: $0.02 < \varepsilon_a < 0.8$, $1< \kappa_a<2.8$, $-0.6 < \delta_a <0.9$, $0.02 < s_1 < 0.75$. Note that these results were obtained assuming an ideally conducting wall on the plasma boundary. Without the wall the results would be up to two times larger. The fit (4.7) describes well the set of KINX results, with the exception of some cases with low ε_a and small growth rate. These cases, however, are not of practical interest because low ε_a is not realistic for modern tokamaks and low growth rate means that the mode is likely to be stabilized by non-ideal effects.

The fit has a functional form which is different from (2.98, 2.99). There is no dependence $1/s_1$, as predicted by (2.99): we did not find a good fit with such a functional dependence. Figure 4.20a shows the dependence of the growth rate on s_1.
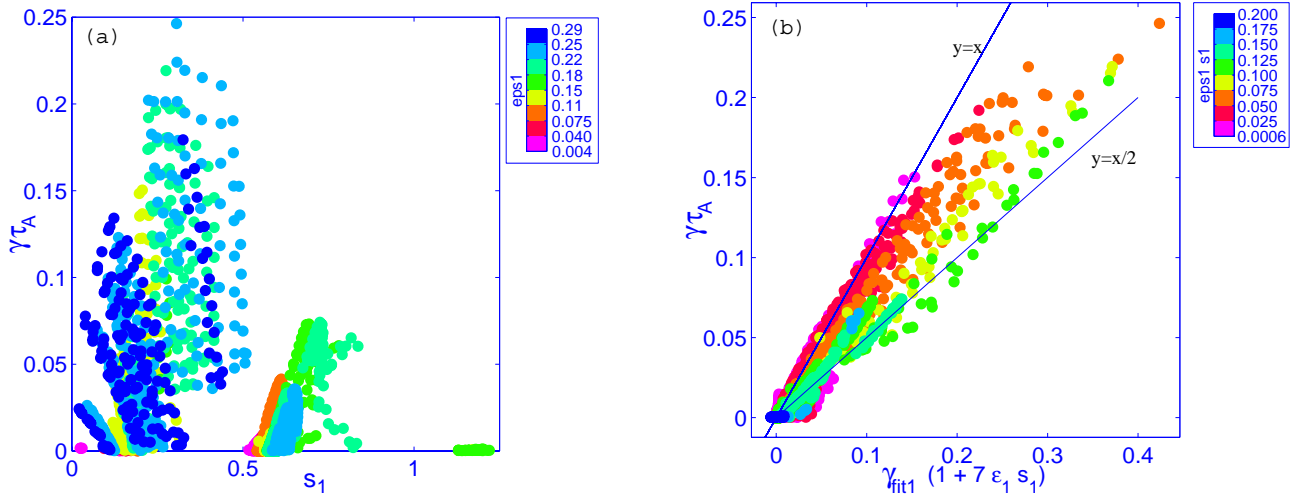
Figure 4.20 a) The growth rate dependence on s_1, b) same as in Figure 4.19, but without correction $1 / (1 + 0.7\varepsilon_1 s_1)$

Two distinct groups of points are seen in Figure 20a, corresponding to two different current density profiles used in our calculations: one with low shear and one with higher shear. It is seen that there is no pole characteristics, $1/s_1$, for small values of s_1. If one removes the denominator $1 / (1 + 0.7\varepsilon_1 s_1)$ from the formula (4.8), the remaining fit gives the results presented in Figure 20b, spanning the values between one and two times the KINX results. The discrepancy increases with increasing $\varepsilon_1 s_1$ and the color groups are well "aligned", confirming that the combination $\varepsilon_1 s_1$ is a good choice.

The comparison of the analytical predictions (2.98-2.99) with the KINX results is presented in Figure 21. It is clearly seen that the analytical formula describes the KINX data much worse than our fit. The analytical formula works much better than the fit for the case of low inverse aspect ratio, as shown on the Figure 21b, but at realistic ε_a it overestimates the growth rate. Therefore we argue that the fit (4.7) should be used instead of formulae (2.98-2.99) for realistic plasmas.

The absence of a dependence of β_{bu}^{crit} on triangularity in the fit (4.5) is astonishing at first, since it was present in the earlier version of the fit (4.4), and it was important to explain the experiments presented in Section 4.2.3. It can be explained by the fact that the role of triangularity in β_{bu}^{crit} is a relatively small effect, especially at large $\gamma\tau_a$, even if in some cases it is important, as the above described experimental studies have shown.
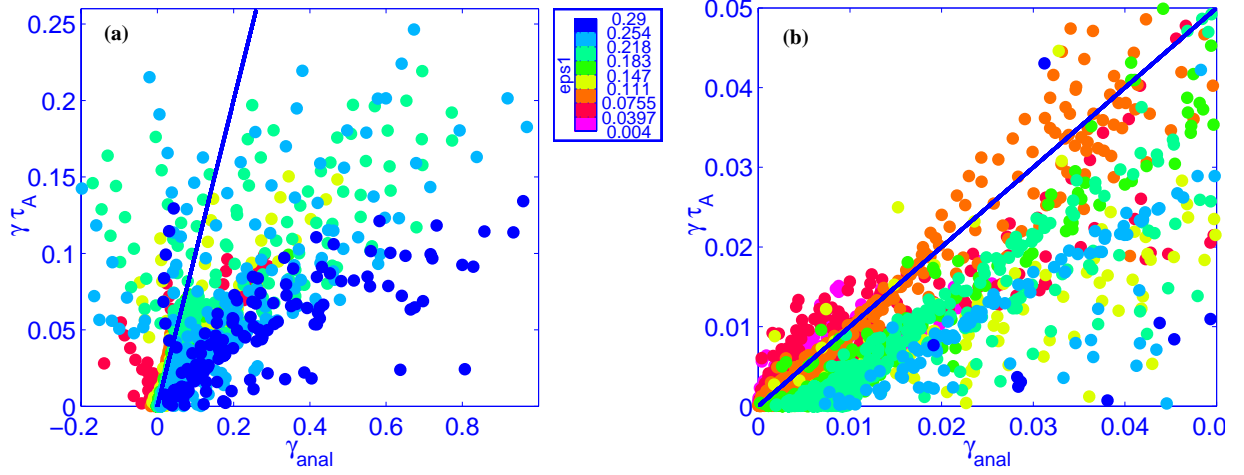
Figure 4.21 a) Analytical formulae, (2.98-2.99) versus the KINX results, as in Figure 4.19. (b) Zoom for $\gamma\tau_a \leq 0.05$.

In real experiments the edge elongation and triangularity are usually controlled, and the internal values self-adjust, following the variations of the edge geometry. The penetration of elongation into the plasma depends substantially on the triangularity: at high triangularity the elongation penetrates the plasma much less than at low or zero triangularity. Therefore the effect of triangularity on the ideal kink mode growth rate can partially be explained by variations of κ_1 with δ at the same κ_a. Figure 4.22 illustrates this. The growth rate dependence on δ_1 is presented there for two cases: one with fixed $\kappa_a = 2.4$ (dash-dotted line) and another with fixed $\kappa_1 \approx 1.4$ (solid line). It is seen that in the second case the growth rate is higher, because κ_1 is larger. The current profile is the same and the shear at $q = 1$ surface varies only slightly. For high triangularity, $\delta_a > 0.4$, the edge elongation required to keep κ_1 constant, increases substantially (Figure 4.22b), in particular for $\delta_a > 0$. On the other hand, at fixed κ_a the elongation at $q = 1$ decreases at high triangularity. This effect has the same trend as discussed in the previous Section and explains a substantial part of the stabilizing effect of positive and very negative triangularity, although not the whole effect: the solid line in Figure 22a still shows the tendency to stabilization at constant κ_1 with increasing negative or positive triangularity.

This shape effect is illustrated by the fit (4.8), shown in Figure 4.22a for both cases. They both reproduce the triangularity stabilization trend, even if it is not introduced explicitly in the formula. This trend is also seen in Figure 4.23, where the fit (4.8) is compared with the KINX results for our experiments. Even without an explicit triangularity term in the formula for β_{bu}^{crit}, the Figure 4.8 reproduces much better the KINX results than the analytical fits (see Figure 4.13).
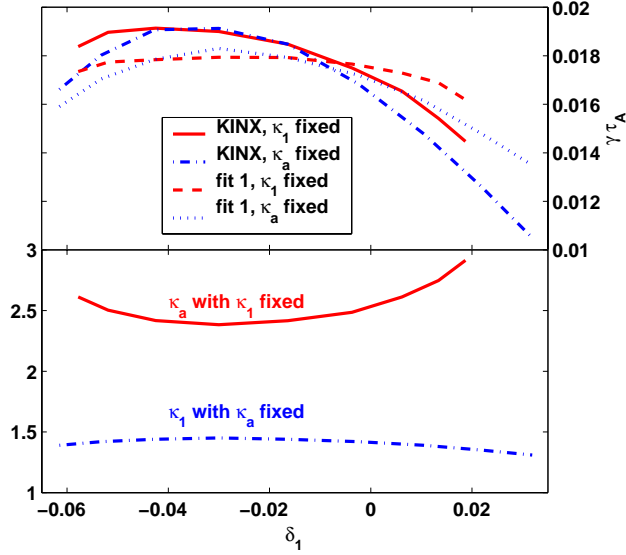
Figure 4.22 Dependence of the ideal growth rate on triangularity, varying δ_a between -0.6 and 0.8 by steps of 0.2, with standard parabolic profiles and $r_1/a = 0.5$. At larger positive δ, one needs a much larger κ_a to keep κ_1 fixed and elongation penetrates much less, leading to a 40% larger growth rate

It should also be noted that the penetration of elongation into the plasma depends substantially on the shape of the q profile. For example, in the case of low shear the elongation penetrates the plasma much better and higher κ_1 values are obtained for the same κ_a. In this case the fit (4.8) can overestimate the growth rate. The following correction to the fit is proposed in order to minimize this effect:

$$\gamma\tau_a^{fit} = 0.44\frac{\varepsilon_1\kappa_1}{1+7\varepsilon_1 s_1}\left[\beta_{bu} - \left(0.9 - \left(0.6 + 0.1s_1\right)\kappa_1\right)\right] \qquad (4.9)$$

This small correction improves the fit at very large elongation and at decreasing l_{i1}, where the sawtooth oscillations disappear [90], as well as in the case of experiments described above (Figure 4.23, upward triangles).

As follows from the discussion, the important feature of the fits (4.8) and (4.9) is that in order to obtain valuable results, one has to modify not only a single parameter to find its influence on the mode stability, but to modify in a self-consistent way the other parameters in the sense that they correspond to an equilibrium which can be obtained in experimental conditions. Thus, these fits are very convenient for the transport codes, where the equilibrium needs to be re-calculated at each time step [86] and these self-consistent parameters are readily available.
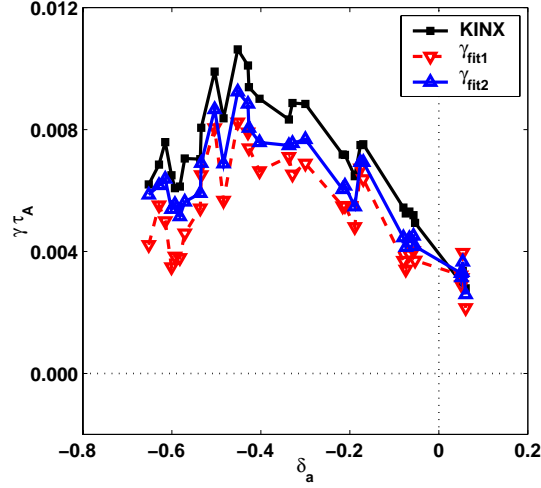
Figure 4.23 KINX results as in Fig. 4.13 and the corresponding values using the fits (4.8) (downward triangles) and (4.9) (upward triangles). The non-monotonic dependence on δ is very well reproduced and it is consistent with the minimum in sawtooth period shown in Fig. 4.12.

4.4 Conclusions

- At low inverse aspect ratio the numerically calculated ideal internal kink growth rate corresponds well with analytically predicted values. The correspondance remains good until the aspect ratio of the TCV tokamak, $\varepsilon_a \le 0.28$, in particular for small and moderate β_{bu} values, even up to $\kappa_a \sim 2.0$. At higher ε the agreement deretiorates and at $\varepsilon_a \sim 0.8$, which corresponds to the modern tight aspect ratio tokamaks like MAST, NSTX etc. the analytical formula (2.98) is not useful anymore, even if $\varepsilon_1 < 0.3$ ($\hat{\varepsilon}_1 < 0.6$).

- At moderate and high ε_a the dependence of the ideal internal kink growth rate on basic plasma parameters is different from that analytically predicted: the growth rate is linearly and not quadratically proportional to ε_1 and the dependence on β_{bu} is essentially linear and not quadratic.

- The behavior of sawtooth oscillations in the TCV experiments with varying negative triangularity correlates very well with the dependence of the ideal internal kink growth rate on triangularity, and not with the behavior of the available formulae for the resistive kink mode growth rate. It is thus possible to conclude that in these experiments the sawtooth crash was triggered by the ideal internal kink mode.

- A new approximate fit of the numerically calculated ideal growth rates for the wide variety of plasma conditions is proposed. This fit (4.9) should be used for the prediction of the ideal internal kink mode behavior instead of the analytically derived formulae in case of moderate and high inverse aspect ratio. Note that the effect of removing the wall on the plasma boundary can

increase $\gamma\tau_a$ typically by up to a factor of two. This also shows that the eigenmode is not a top-hat and explains the discrepancy with analytical predictions.

- When using the analytical formulae or the fit of numerical data for the kink mode growth rate, it is important to remember that in real plasmas the plasma parameters are interconnected. Thus by modifying only one parameter, leaving others intact, one can come to wrong conclusions regarding the effect of this parameter. When modifying one plasma parameter, one should change other values in a self-consistent way, as it happens in real plasmas or in equilibrium calculations. For example, the stabilizing role of the plasma triangularity can be partially explained by the weakening of the plasma elongation penetration from the plasma edge to the plasma core at increasing positive or negative triangularity. The proposed fit can be used in the transport codes, where the equilibrium is re-calculated at each time step. The transport codes can also be used for providing the "self-consistent" equilibria to be used for the MHD stability analysis when a given parameter is modified.

Chapter 5. The ideal stability of highly elongated TCV plasmas: shape optimization

This chapter deals with the stability of ideal external kink mode for highly elongated TCV plasmas and with possible ways of obtaining the maximum possible plasma elongation with better confinement properties by plasma shape optimization [72, 73].

5.1 First numerical estimations of the ideal MHD stability of high κ_a plasmas

One of the most important missions of the tokamak TCV is to study the influence of the plasma shape on various plasma properties, and in particular plasmas with very high elongation (κ_a up to 3.0). The predictions of the ideal MHD stability of such plasmas by numerical simulations were used for the TCV tokamak design [8]. Two different plasma shapes, the "racetrack" and D-shaped plasma were analyzed against the $n = 1$ external kink mode stability with different q profiles.
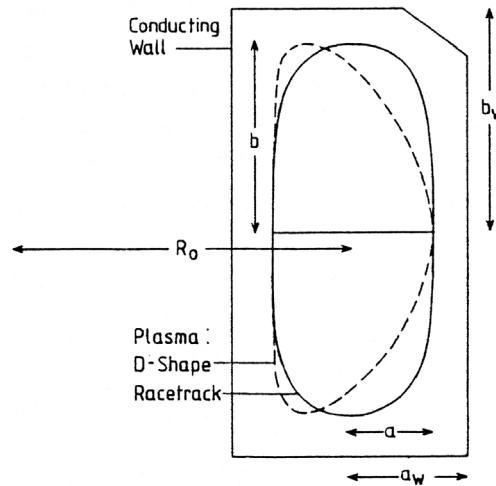
Figure 5. 1 (Figure 1 in [8]) TCV geometry showing the racetrack and D-shape cross-sections

The current limitations for these plasmas were established and expressed as the operating diagrams in the $q_a - q_0$ space. The beta optimization was also carried out for these two plasma shapes with elongation 2.5 and the maximum achievable β_t was plotted versus the normalized current

$$I_{NA} = \frac{\mu_0 I}{a B_0} \qquad (5.1)$$

where $\mu_0 = 4\pi \cdot 10^{-7}$ Hm^{-1} is the free space permeability, I_p is the plasma current [A], a is the plasma minor radius [m] and B_0 is the vacuum toroidal field [T] in the plasma center. It is important to note

that a different and more practical notation of the normalized plasma current is used more widely than (5.1):

$$I_N = \frac{I[\text{MA}]}{a[\text{m}]B[\text{T}]} \cong 0.8 I_{NA} \tag{5.2}$$

As the stability measure, the "normalized beta" is usually used:

$$\beta_N = \frac{100\beta_t}{I_N} = \frac{\beta_t[\%]}{I_N} \tag{5.3}$$

where β_t is the toroidal beta (2.44), which is often expressed in %. It was shown in [91] by Troyon *et al* that in different tokamaks and different plasma configurations the ideal MHD modes become unstable when β_N exceeded some critical value. This led to the formulation of the Troyon limit:

$$\beta_N \leq 3.0 \tag{5.4}$$

which can be expressed in terms of β_t and I_N:

$$\beta_t[\%] \leq 3.0 I_N \tag{5.5}$$

Numerous experimental studies have confirmed (Ref. [92] for example) the existence of the Troyon beta limit and it is widely used as a reference for the search of better plasma configurations. The normalized beta is a convenient measure of the state of stability of the plasma relative to the Troyon beta limit. Furthermore it was shown that the effect of the current profile changes the actual limit, so that the following formula is often used:

$$\beta_N \leq 4 l_i \tag{5.6}$$

The optimized beta corresponded to very flat q profiles in the plasma center, very close to 1 at the plasma axis. The value of q_0 was set on purpose above one to avoid the internal kink mode discussed in the previous Chapter, since the operation limit set by the external kink mode was a goal of the study. The Figure 5.2 shows the results of the calculations of the operation range for D-shaped plasma and for the racetrack. The highest achievable normalized current is $I_N \approx 3.4$ in the racetrack configuration and $I_N \approx 2.8$ for the D-shaped plasma. The elongated plasmas allow to achieve much

higher β_t than the circular ones, as seen from the comparison with the beta limit for the circular plasma, shown in Figure 5.2 (dashed line). Another important result is that the β_t limit is lower than the Troyon limit, indicated by the solid lines in Figure 5.2 for high values of I_N, $I_N \geq 2.5*0.8 \approx 2.0$.
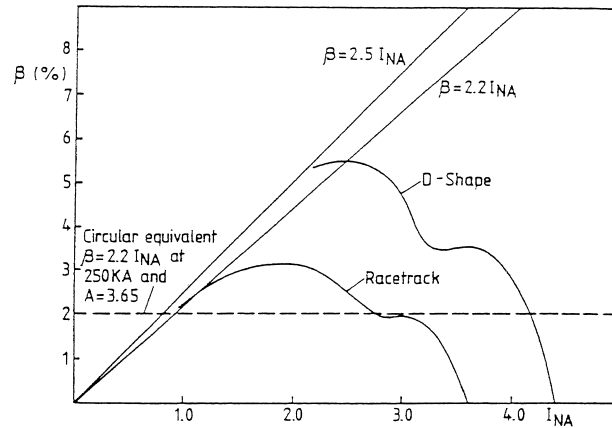

Figure 5.2 (Figure 4 from [8]) Beta limit scaling with normalized current (5.1) for the racetrack and D-shape configurations

5.2 The experimental studies of highly elongated plasmas on TCV

a) t, s   b)
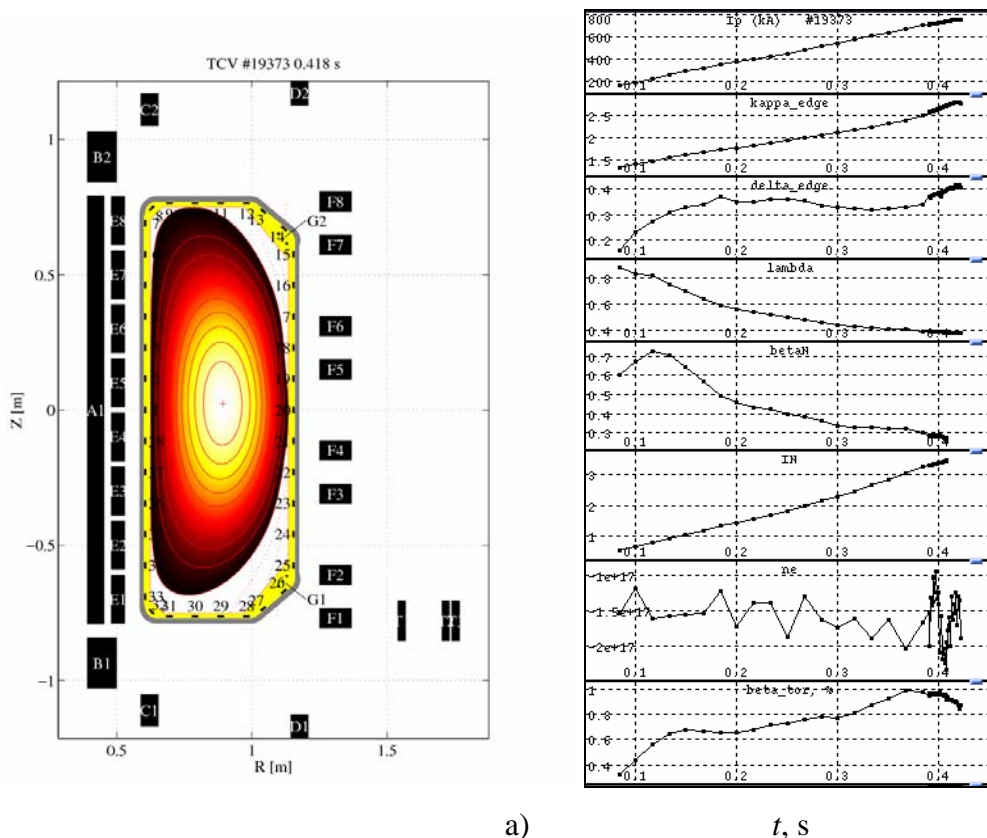
Figure 5.3 The plasma with record elongation (#19373), obtained in TCV: I_P = 750 kA, B = 0.8T, κ_a = 2.80, δ_a=0.3, λ_a=0.38, I_N = 3.9: a) the plasma shape, b) the time traces: plasma current I_P, edge elongation κ_a, edge triangularity δ_a, edge squareness λ_a, normalized beta β_N, normalized current I_N , plasma density n_e and toroidal beta β_t in %

During the TCV experimental activity much effort was devoted to the extension of the TCV operating limits towards higher elongation and higher normalized current. The highest elongation, obtained on TCV is $\kappa_a \approx 2.8$ [72, 73], a world record and the maximum normalized current, obtained in these experiments, is $I_N = 3.9$ ($I_{NA} = 4.9$), presented in Figure 5.3. These record values were obtained in conditions of off-axis plasma heating by the second harmonics ECCD, by the optimization of the vertical position system and by plasma shape optimization with respect to the ideal MHD stability.

5.3 The TCV plasma shape optimization

The plasma shape optimization was carried out in a way similar to the preliminary stability calculations. But instead of finding the dependence of the optimized β_t on I_N, only the maximum achievable current at constant $\beta_t = 1\%$ was looked for. This value corresponds to the typical value obtained in these experiments with mainly ohmic heating, as in the shot presented in Figure 5.3. The $n = 1$ kink mode stability in plasmas of different shapes with very flat q profiles just above 1 in the center was studied.
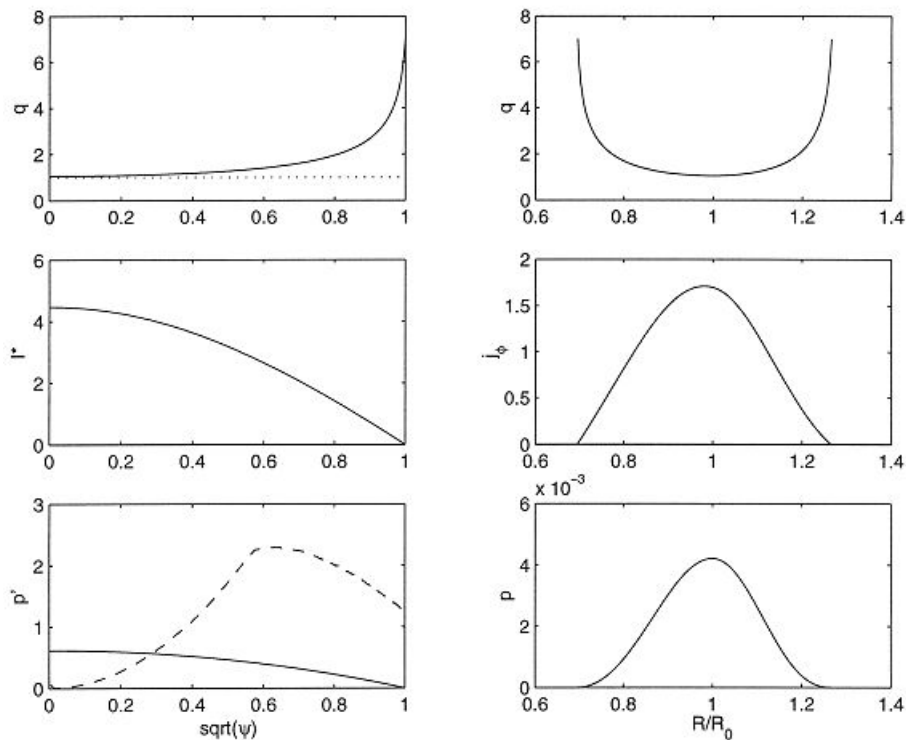

Figure 5.4 The q, current and pressure profiles, used in the plasma shape optimization studies. j* is the surface averaged current density, j_ϕ - the toroidal current density.

A number of plasmas with standard shapes, described by equations (5.4) with high elongation $\kappa_a = 2.7$ and different edge triangularity δ_a and squareness λ_a were studied in order to define the dependence of the current limit on λ_a and δ_a, and to find the optimum plasma shape.

$$R = R_0 + a[cos(\theta + \delta \sin\theta - \lambda \sin 2\theta)]$$
$$Z = Z_0 + a\kappa \sin\theta \tag{5.4}$$

In Figure 5.5 the results of these studies for $\kappa_a = 2.7$ are shown together with the $n = 0$ mode stability analysis of these plasmas, at the $n = 1$ current limit, by the code DPM [93], performed by F. Hofmann.
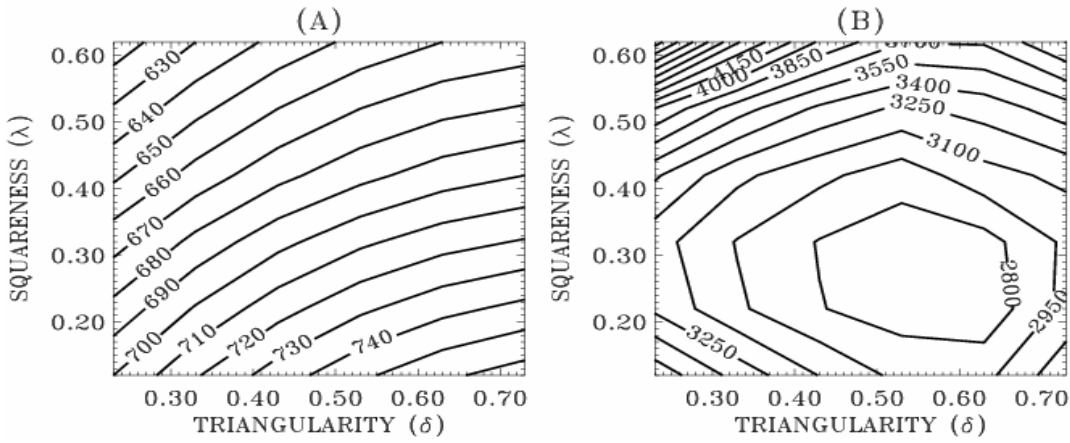
Figure 5.5 a) The ideal MHD current limit in kA due to $n = 1$ mode; b) the growth rate of $n = 0$ mode in s^{-1} at the current limit.

It is seen that the current limit increases with the triangularity and decreases with the squareness, but the $n = 0$ growth rate has a minimum around $\delta_a \approx 0.6$ and $\lambda_a \approx 0.25$. These optimal conditions correspond to the TCV experimental results. In most cases the plasmas with $\kappa_a > 2.5$ were performed with almost the same shape parameters: $0.50 < \delta_a < 0.63$ and $0.22 < \lambda_a < 0.25$. The deviations from this shape did not lead to improvement of the plasma stability. It is important to note that the optimum plasma shape depends to a large extent on the plasma wall shape. The conclusions about the plasma shape are not universal, but are valid for this particular tokamak. For example, the rectangular shape of the TCV vacuum vessel, serving as the stabilizing wall, implies the relatively high squareness of the plasma for better $n = 0$ mode stability. In tokamaks with a D-shaped vacuum vessel the optimum shape conditions would be different (lower λ_a and higher δ_a).

5.4 New plasma shapes

In addition to the usual plasma shapes, described by equations (5.4), several alternative plasma shapes were also studied, as in Figure 5.6.

The current and pressure profiles were the same, as in the previous Section (Figure 5.4). The parameters of these plasmas and the corresponding current limits at $\beta_t=1\%$ are presented in Table 5.1.
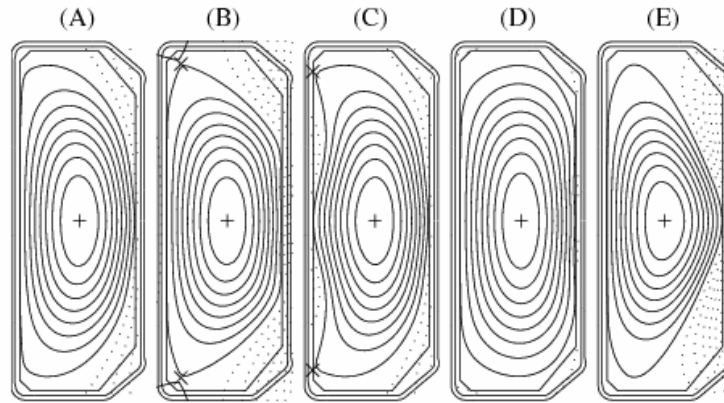

Figure 5.6 Classical D-shaped plasma (a) and alternative shapes: (b) trapezoid, (c) peapod,   (d) racetrack, (e) triangle

	D-shaped	Trapezoid	Peapod	Racetrack	Triangle
Elongation κ_a	2.7	2.7	2.7	2.7	2.7
q_{95}	2.36	2.35	2.47	2.51	2.26
I_N	3.65	3.25	3.39	3.25	3.54
$\gamma_{n=0}$, s^{-1}	2507	1327	>10000	3080	>10000

Table 5.1 Parameters and current limits of various plasma shapes

The trapezoidal plasma is the only configuration, having $\gamma_{n=0}$ better than the classical D-shaped plasma, although its $n = 1$ current limit is lower. Thus, the trapezoidal plasma can be an interesting target for experimental studies.

The comparison of trapezoidal and D-shaped TCV plasmas is presented in Figure 5.7. In both cases $\kappa_a = 2.6$, $\beta_t \approx 1.1\%$. The current limit manifested itself by the appearance of MHD modes, thus leading to the plasma disruption. The D-shaped plasma current limit is $I_N = 3.35$, which is close to the calculated one (Table 5.1). In the case of the trapezoidal plasma shape, the highest achievable current was $I_N = 2.77$. The growth rates $\gamma_{n=0}$ were 2730 and 2118 s^{-1}, respectively. These results are consistent with the numerically calculated limits in Table 5.1. Although higher elongations were not obtained in the trapezoidal plasma shape, it is possible that by further shape and current profile optimization higher elongations could be reached.
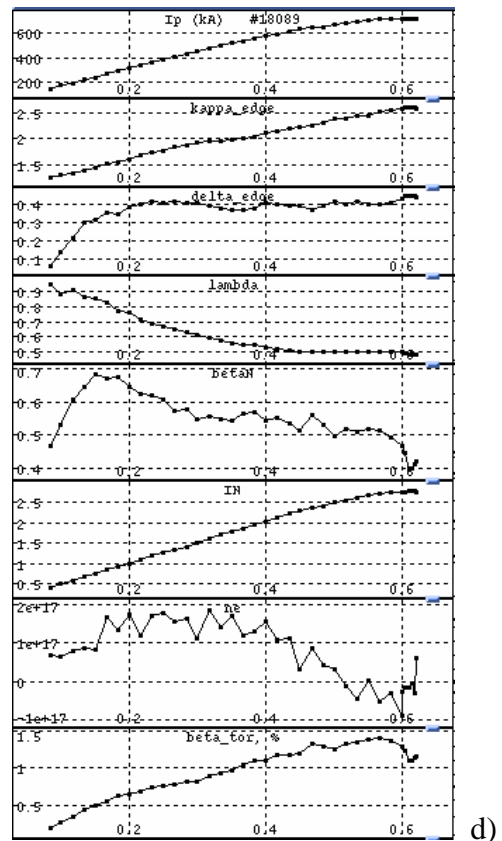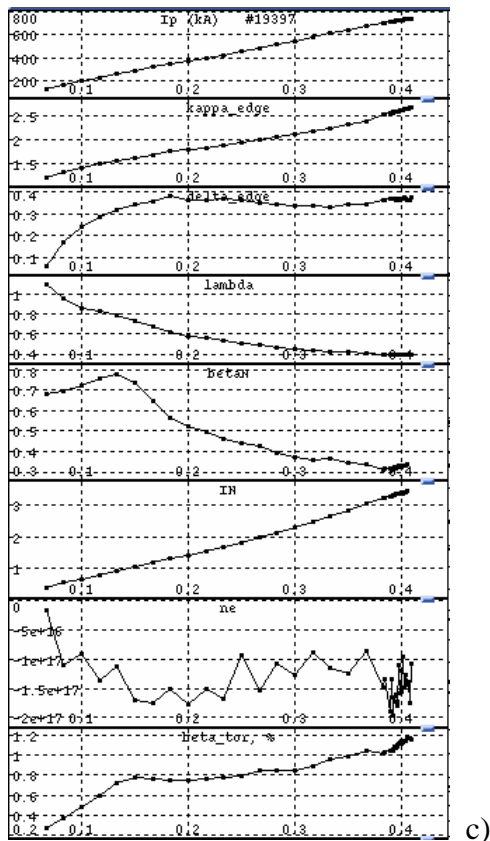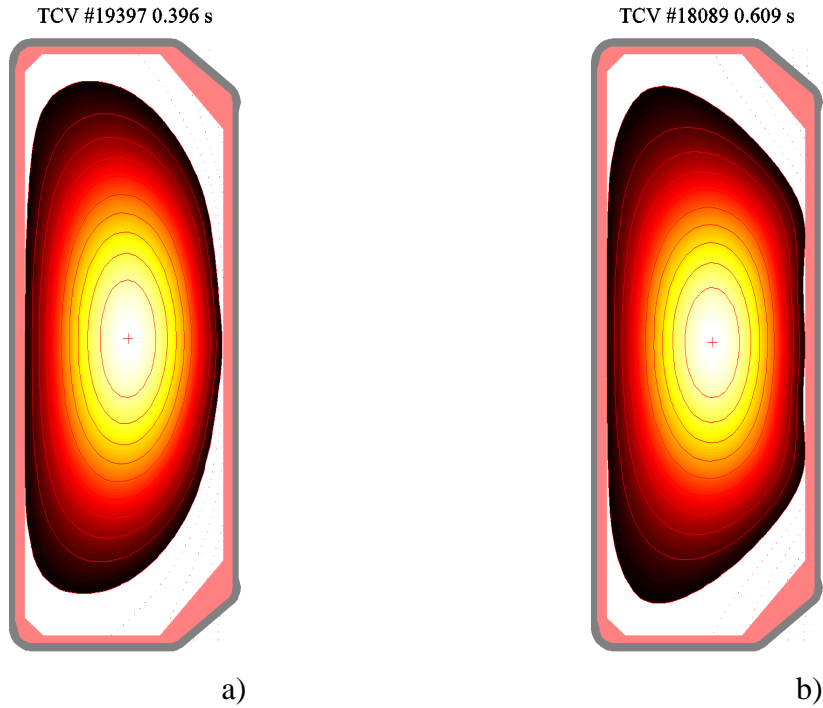
Figure 5.8 D-shaped and trapezoidal plasmas in TCV: plasma shapes (a,b) and (c.d) the time traces: plasma current I$_P$, edge elongation κ_a, edge triangularity δ_a, edge squareness λ_a, normalized beta β_N, normalized current I$_N$, plasma density n$_e$ and toroidal beta β_t in %

5.5 Conclusions

- For TCV conditions, the analysis of the ideal MHD stability dependence on plasma triangularity and squareness revealed that the optimum conditions are met at $\delta_a \approx 0.6$ and $\lambda_a \approx 0.25$.

- The plasma shape, optimized with respect to the ideal MHD $n = 1$ and $n = 0$ modes, corresponds well to the experimental plasma shape, with which record elongated plasmas were obtained in TCV.

- The current limits experimentally obtained with the alternative plasma shape (trapezoid), compared with the D-shaped plasmas are consistent with the numerically predicted values.

- The ideal MHD stability of highly elongated plasmas determines the experimentally achievable operational limits, the latter can be predicted by means of numerical calculations. This has confirmed the predictive calculations performed earlier and it shows the value of ideal MHD calculations for designing experiments.

Chapter 6. The ideal MHD stability of the reversed shear TCV plasmas

This chapter is devoted to a very promising kind of tokamak equilibrium: the reversed shear configuration. The experiments on the TCV tokamak are described and then the ideal MHD stability of such plasmas is discussed in detail on the basis of numerical calculations. Infernal and external kink modes are discussed. On the basis of this analysis, possibilities of obtaining better plasma performance, while avoiding disruptions caused by ideal MHD instabilities, are proposed.

6.1 The reversed shear plasmas: why create and study them?

The search for plasma configurations, which provides better confinement conditions, is one of the major research areas of modern tokamak physics. One of promising directions is the creation of plasmas with an inverted q profile. In such plasmas, internal transport barriers (ITB) can be formed, leading to improved plasma performance [94, 95, 96, 97]. The so-called advanced regimes, with inverted q profiles, are very interesting for future thermonuclear reactors. In particular, such scenarios are of interest for steady state operations in the ITER reactor. These plasmas are investigated both experimentally and theoretically throughout the world. The TCV tokamak, because of its unique capability of modification of plasma current and pressure profiles by adjustment of its six independent EC-wave launchers, is an excellent tool for such studies [98, 99, 100, 101].

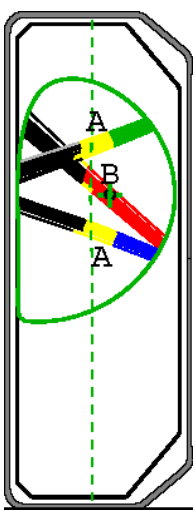## *6.2 Fully non-inductive current sustainment and eITB creation in TCV*

Figure 6.1
The EC-power launch geometry

The reversed shear plasma studies are intensively studied in CRPP and represent one of main objects of experimental studies on TCV tokamak [19, 20, 21, 22, 102, 103] experimental program. In Ref. [102, 104, 105, 106, 107] TCV experiments are described where the full replacement of the plasma current by non-inductive current was achieved. The plasma current was sustained by the bootstrap current and by the EC-driven current. Two independent EC waves launchers were adjusted so that most of the EC-power was absorbed off-axis (beams A in Figure 6.1). The non-inductive current j_{CD} generated in the off-axis area of the EC power deposition led to a very broad current density profile [23]. The third gyrotron was turned on later and its power was absorbed on the plasma axis (beam B). The toroidal injection angle φ of this third EC-waves beam was changed between shots, so the influence of the pressure profile and on-axis plasma current modification to the confinement properties was studied, as shown in Figure 6.2.
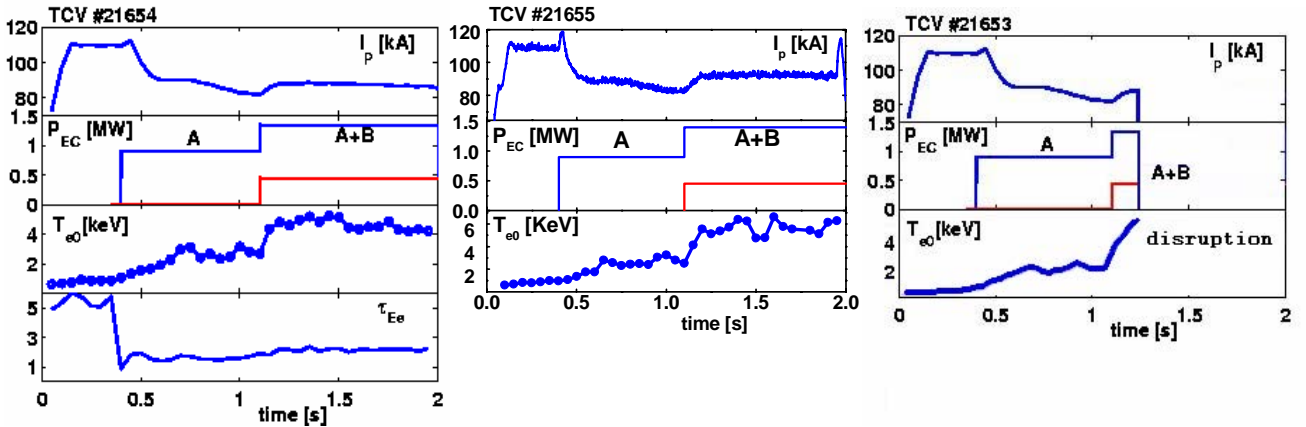
Figure 6.2 TCV reversed shear discharges with different toroidal injection angle φ of the central beam: #21654, φ= 0°; #21655, φ = -5°; #21653, φ= -15°;

The hollow current density profiles in these experiments correspond to inverted q profiles (Figure 6.5). The confinement enhancement over the standard RLW scaling [108] $H_{RLW} \equiv \tau_{Ee}/\tau_{RLW}$, where τ_{Ee} is the electron energy confinement time and τ_{RLW} is the RLW scaling is presented in Figure 6.3. Values of H_{RLW} above 2 indicate the formation of an electron internal transport barrier (eITB) in these plasmas. It is clearly seen that counter current drive on the plasma axis leads to a confinement improvement. However, too much increase in the on-axis counter-current (by increasing the toroidal injection angle) leads to a disruption (#21653).
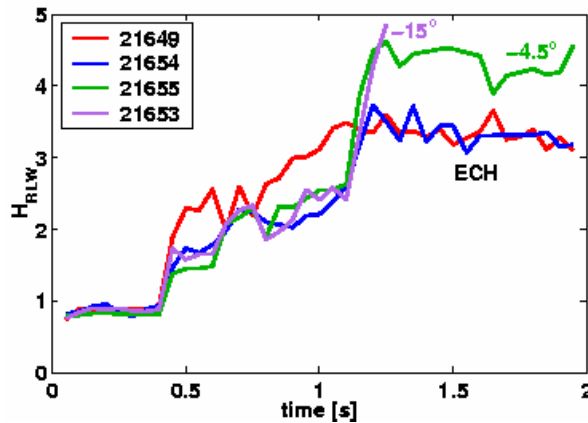

Figure 6.3 The confinement enhancement factor for different on-axis toroidal injection angles

The changes of the on-axis toroidal injection angle lead not only to modifications of the q profile (the stronger the counter-current, the deeper is the q profile inversion), but also to the pressure profile, as seen in Figure 6.4.

The $m/n = 3/1$ and 2/1 components in the edge magnetic signal were observed during the disruption in the shot #21653 with the characteristic growth time of ~ 20 μs, which is a typical growth rate for ideal instabilities. It indicates the presence of $m/n = 3/1$ and 2/1 modes during the disruption. For this reason the main attention was devoted to the $n = 1$ stability, although for some cases the $n = 2$ stability was also examined.
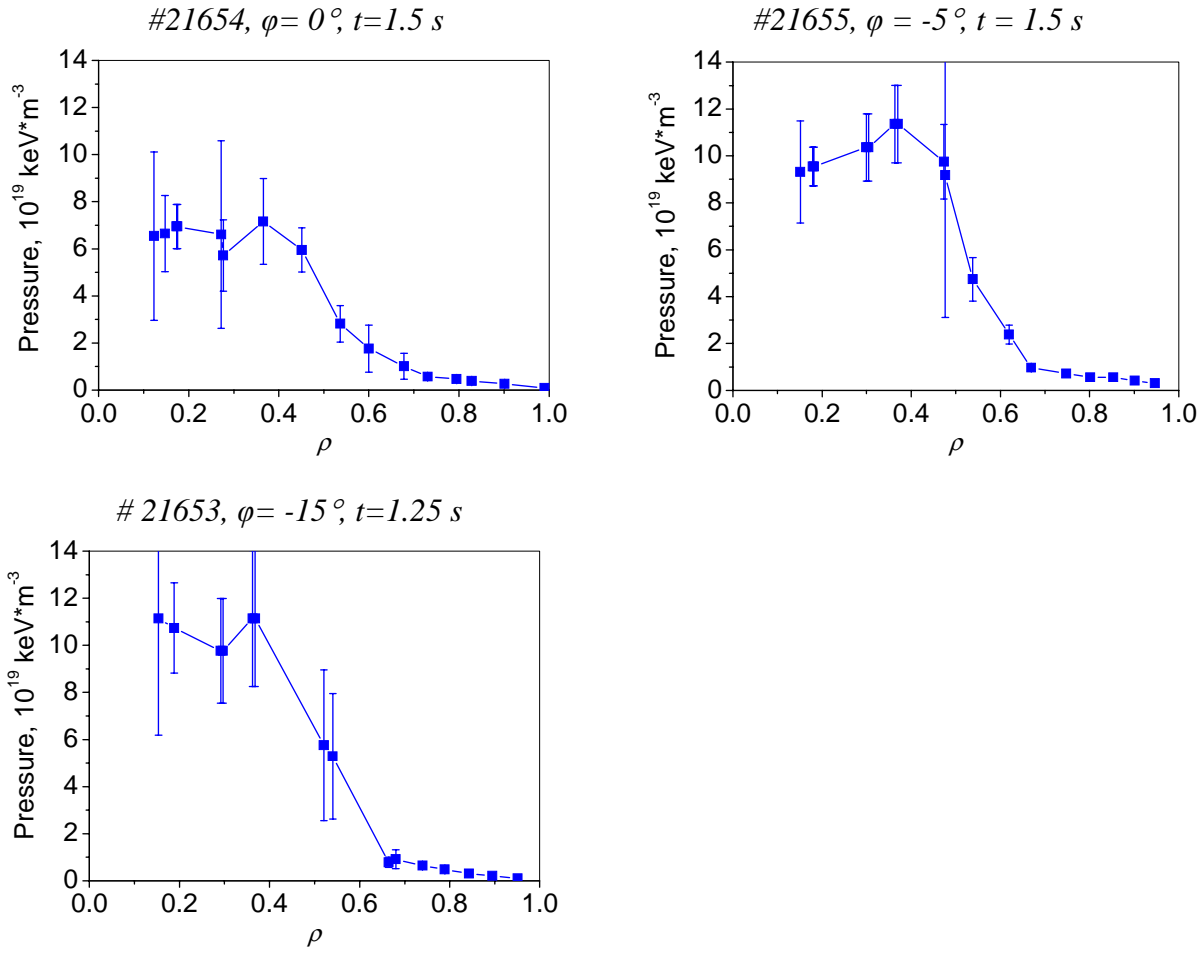
74

Figure 6.4 The pressure profiles (Thomson scattering) for different toroidal injection angles, t = 1.25 - 1.5 s, corresponding to the discharges shown in Figure 6.2. For the discharge #21653 the profile corresponds to the last measurement about 20 ms before the disruption.

In Figure 6.4 and below in this chapter

$$\rho \equiv \frac{\sqrt{\psi - \psi_0}}{\sqrt{\psi_a - \psi_0}} \tag{6.1}$$

where ψ is the poloidal flux (2.28), ψ_a is the value of ψ at the plasma edge and ψ_0 – on the axis.

6.3 Numerical MHD stability analysis

The TCV shot #21655 was used for the MHD analysis because it is situated in between two extreme cases, the shot #21654 with zero on-axis toroidal injection angle and shot #21653, for which the high toroidal injection angle caused a disruption. By varying the pressure and current profiles for shot #21655, it is possible to simulate both cases.

The Thomson scattering data of the pressure profile and the q profile for the shot #21655 are shown in Figure 6.5. Note that $q_{min} \approx 2.7$ is close to 3. This q profile corresponds to the basic results obtained with the bootstrap current density and the EC current density j_{CD} under assumption of a constant radial diffusion profile [109, 110]. The profile j_{CD} is obtained using the Fokker-Planck code CQL3D [111]. It depends on the effective profile of the radial diffusion coefficient. If better confinement is assumed in the centre, even more reversed q profile is obtained [109, 110]. The effect of varying q_{min} and of the degree of current inversion will be discussed in Sections 6.3.5 and 6.3.6.
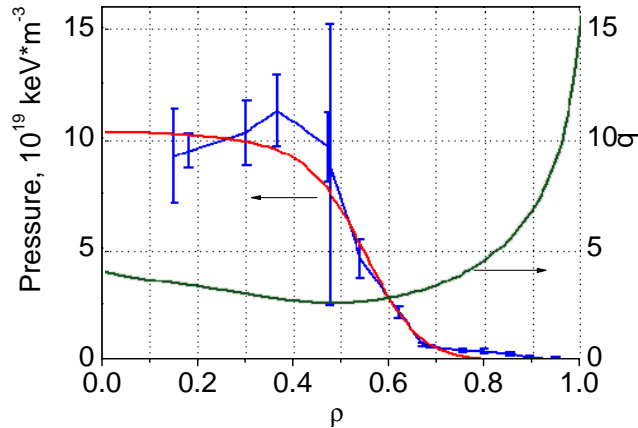

Figure 6.5 The Thomson scattering pressure profile with error bars (blue), its basic fit (red) and the q profile (green) for the TCV shot #21655

6.3.1 Stability analysis of the shot #21655. Infernal mode. Stability dependence on q_{min}.

For the experimental conditions of the TCV shot #21655 the KINX code calculations assuming fixed boundary conditions have revealed an unstable ideal mode $m/n = 3/1$, with the growth rate dependence on β_N as shown in Figure 6.6 ($\beta_N^{exp} \approx 1.0$):
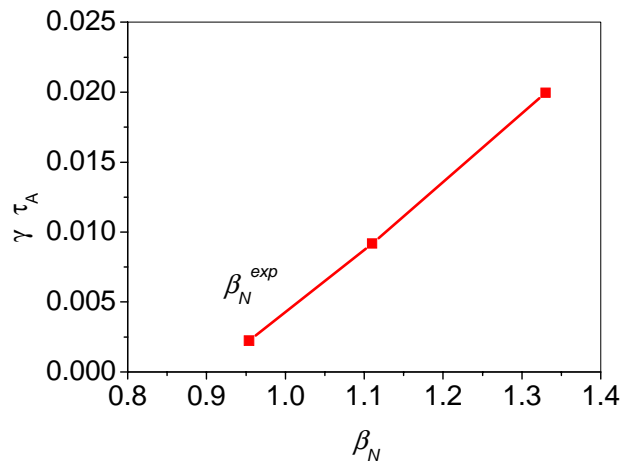

Figure 6.6 The dependence of the 3/1 ideal mode growth rate on β_N for the shot #21655

The shot #21655 is close to the stability threshold, with the $m/n=3/1$ ideal mode close to the stability limit. The instability is possibly caused by a very high pressure gradient at $\rho \approx 0.5$, where the eITB is formed. The value of q_{min} is also of great importance. The role of q_{min} can be seen in Figure 6.7, where the different q profiles analyzed are presented. Here the analytical pressure profile from Figure 6.5 and the experimental value of $\beta_N \approx 1.0$ were used. The profiles that proved to be stable are shown in green, whereas those with unstable modes are in red.
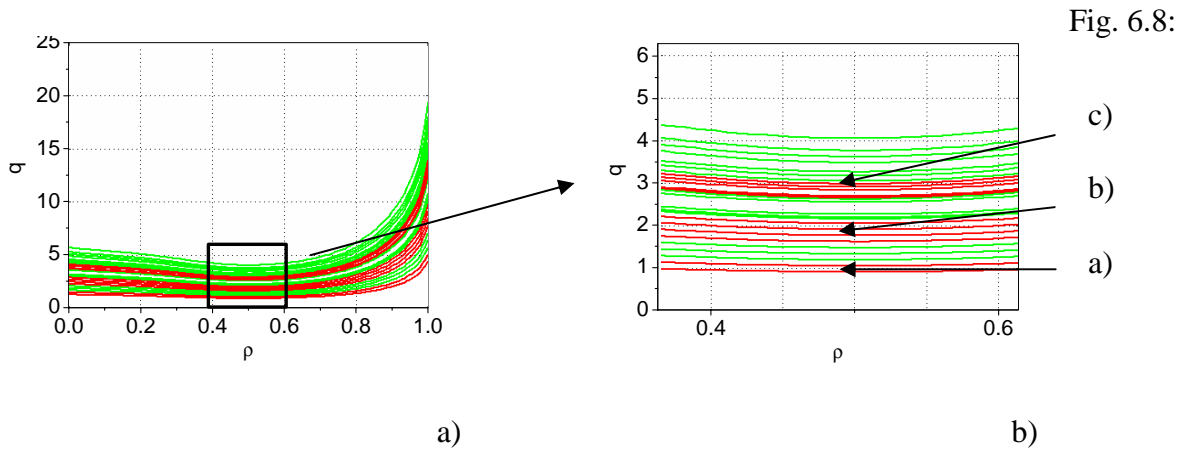

Fig. 6.8:

a)   b)

Figure 6.7 The q profiles, for which the ideal modes are stable (green) and unstable (red) for the shot #21655: a) whole profiles, b) profiles near q_{min}. The correspondence of subfigures of Figure 6.8 to unstable zones is shown on the right.

It is clearly seen that the "red" unstable profiles correspond to values of q_{min} close to integer values 1, 2 and 3. The mode structures for these instability regions are presented in Figure 6.8.

The mode, presented in Figure 6.8 is known as the infernal mode. This mode appears in the area of the low positive shear (just outside the minimum q surface for non-monotonic q profiles). In this area the ballooning theory breaks and the low-n ballooning instability becomes possible. This mode was first described in [23] for monotonic q profiles and then in [24] for reversed shear profiles.
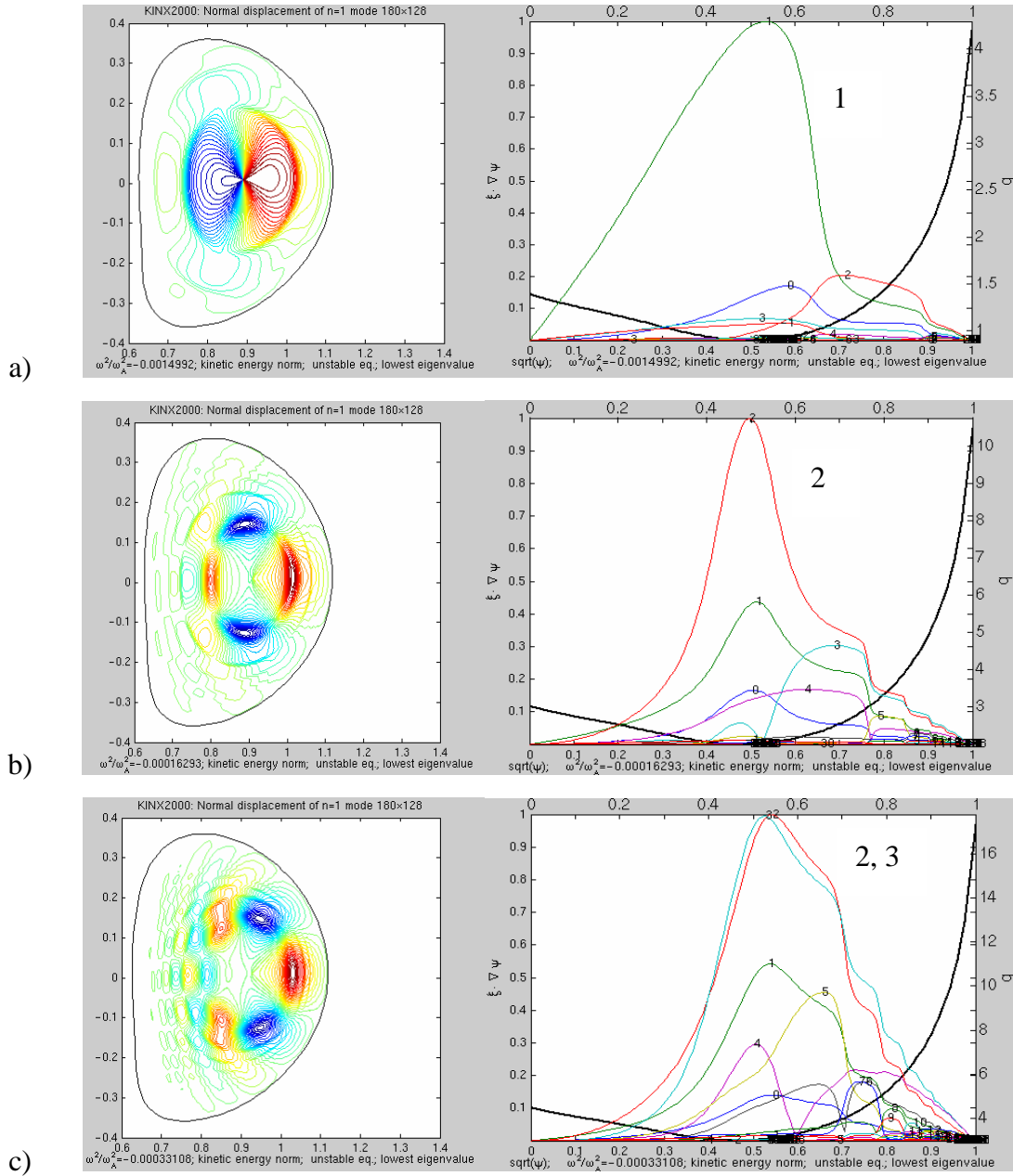
Figure 6.8 The mode structure for unstable q profiles in Figure 6.7: poloidal cross-section and radial structure of $\xi \cdot \nabla \psi$ Fourier harmonics with different m: a) $q_{min} \approx 1.0$, most unstable mode is m/n=1/1, b) $q_{min} \approx 2.0$, m/n=2/1, c) $q_{min} \approx 3.0$, m/n=2/1 and 3/1

The influence of the q_{min} value and of the normalized beta β_N can be seen together, by following the "stability-instability" boundary in the q_{min} - β_N space, calculated by a specially developed Perl script using the following scheme: the pressure and current profiles are given as input. Starting at some values of q_{min} and β_N (q_{min} = 0.8 and β_N = 0.7 in the case presented in Figure 6.9) the script calculates the equilibrium by means of the CHEASE code, using iterations in order to obtain the prescribed values of q_{min} and β_N and then the equilibrium stability is analyzed by the KINX code. If the

78

configuration is stable, then the pressure is increased at fixed $q_{\min}$ until the unstable equilibrium is found. Then $q_{\min}$ is increased again and the procedure repeated until the maximum prescribed $q_{\min}$ is achieved. It is important to note that the current profile, and not the q profile, is kept constant, so the q profile is modified by changing $q_{\min}$ and the plasma pressure. The stability boundary is presented in Figure 6.9 for the same pressure profile as in Figure 6.5.
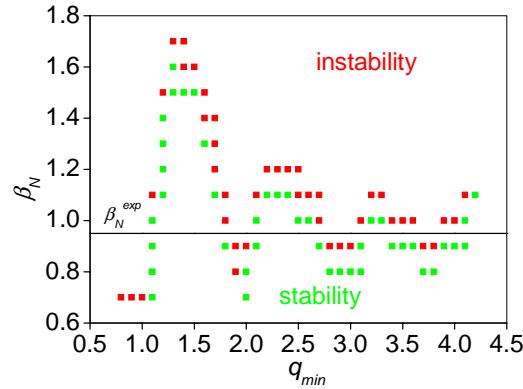

Figure 6.9 The n=1 mode stability boundary plotted in q_{min} - β_N space. Green and red squares correspond to ideally stable and unstable configurations, respectively. Pressure and q profiles of the shot #21655.

It is seen that at $q_{min} \approx 1.0$ the instability begins at very low β_N, because of the m/n=1/1 internal kink mode. In most TCV reversed shear experiments q_{min} does not reach such low values and the internal kink mode is not dangerous. Nevertheless, the internal and external modes with m=2, 3, 4 etc, develop when q_{min} is close to corresponding integers. Between these zones "stability windows" are seen, where the ideally stable plasma can be obtained at relatively high β_N. These "stability windows" correspond to q_{min} values between integers. Thus, one way of improvement of the reversed shear plasma performance is to avoid the integer values of q_{min} by fine adjustment of the current drive and plasma heating. At increasing $q_{min} > 3-4$, the infernal mode is stabilized or becomes an external kink mode, which is less sensitive to the value of q_{min}.

The *m/n = 2/1* and 3/1 components were measured just before the disruption for the shot #21653 [112]. This would correspond to the $q_{\min}$ value near 3, as shown in Figure 6.8c. This is compatible with the slightly more reversed q profiles obtained assuming a lower radial diffusion coefficient in the CQL3D simulations [111]. This is also in agreement with more recent transport simulations using the ASTRA code [113].

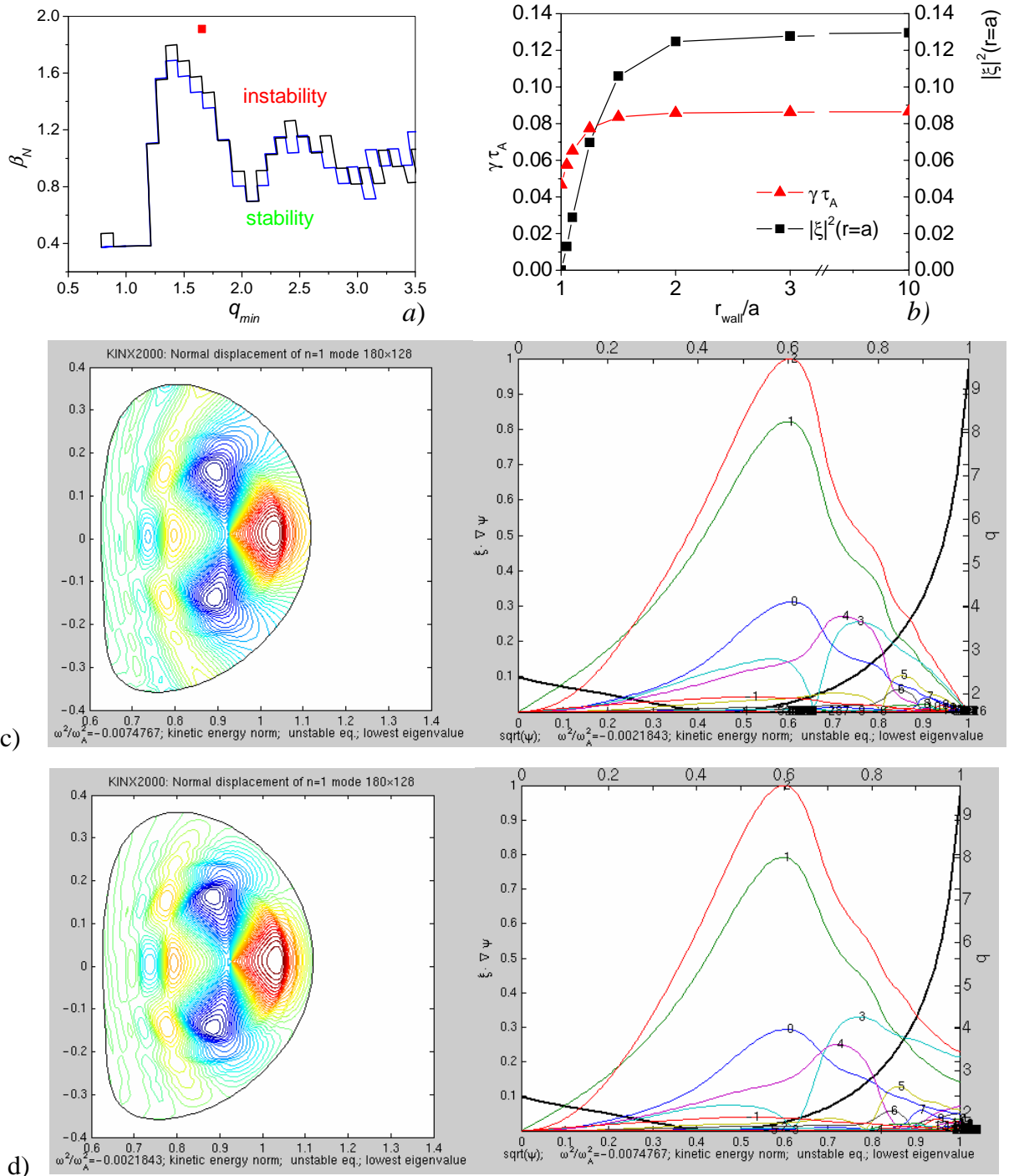## 6.3.2 Fixed and free boundary. External kink mode.

Figure 6.10 The role of the plasma boundary in the infernal mode stability: a) stability-instability boundary with fixed plasma boundary (black) and free plasma boundary at $r_{wall}/a=10.0$ (blue) regimes, b) dependence of the mode growth rate and of the square of the normal displacement. At the plasma boundary on the distance of the wall from the plasma boundary for $q_{min} =1.6$ and $\beta_N = 1.9$ (red square in (a)); The normal displacement in the cases: c) $r_{wall}/a=1.0$, d) $r_{wall}/a=10.0$

As seen in Figure 6.10, the infernal mode stability limit does not depend substantially on the boundary conditions, although the growth rate varies between the fixed boundary and free boundary cases. Figure 6.11 illustrates this.
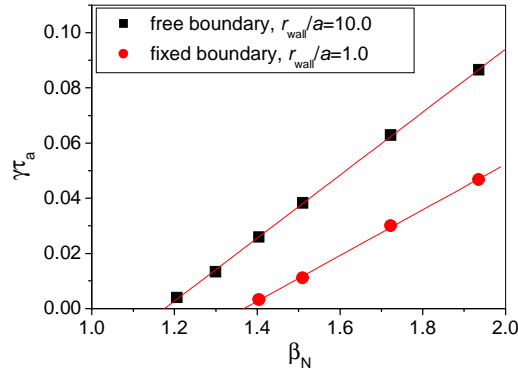

Figure 6.11 The dependence of the infernal mode growth rate on β_N in similar conditions in fixed boundary and free boundary conditions.

The difference of the β_N limit for the fixed and free boundary cases is around 0.2 and is not substantial in comparison with variations of the β_N limit with q_{min}, for example.

With free boundary conditions and at $q_{min} > 3$ another ideal MHD mode becomes unstable: the external kink modes with different m, described in the Section 2.4.2. These modes are localized close to the plasma edge and their existence is not directly connected with the non-monotonic character of q profiles. The external kink mode is mainly a current driven mode, while the infernal mode is mainly pressure driven. However in a real configuration both drives are effective and the modes are not always distinguishable. The structure of the external modes is presented in Figure 6.12, which shows that the maximum amplitude of the radial displacement is more off-axis as compared to Figure 6.10. This is why the fact that q_{min} is integer does not play a role any longer.
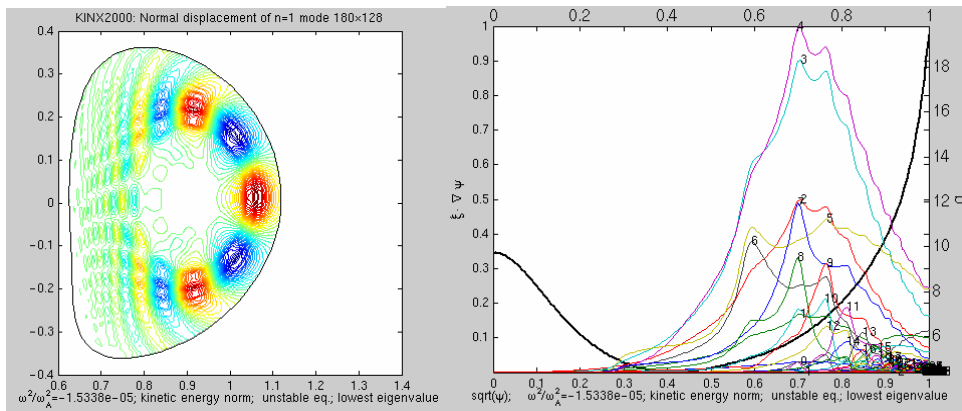

Figure 6.12 An external kink modes at $q_{min} \approx 4.4$ with free plasma boundary: the plot of the radial displacement in the poloidal cross-section and the radial displacement of Fourier harmonics with different m.

At $q_{min} < 3$, the large pressure gradients in regions with small shear, particularly when q_{min} is an integer, are the main drive and can lower the β_N limit significantly. At intermediate $q_{min} \approx 3$ to 5, both pressure and current density drives are important, while at larger q_{min} the external kink is more important.

The infernal modes are more localized in the plasma core and this could explain the minor disruptions, leading to a loss of the core transport barrier, but not of the whole plasma confinement [114].

6.3.3 The role of the pressure gradient

The pressure gradient in the low shear region is considered as one of the main free energy sources of the ideal instability in the reversed shear plasma [23]. Several pressure profiles were studied: one broad profile with parabolic P' profile, typical for standard L-mode plasmas and three profiles with steep and localized pressure gradient, similar to the profile presented in Figure 6.5 and characteristic for plasmas with an internal transport barrier. These profiles and corresponding stability limits are presented in Figure 6.13.
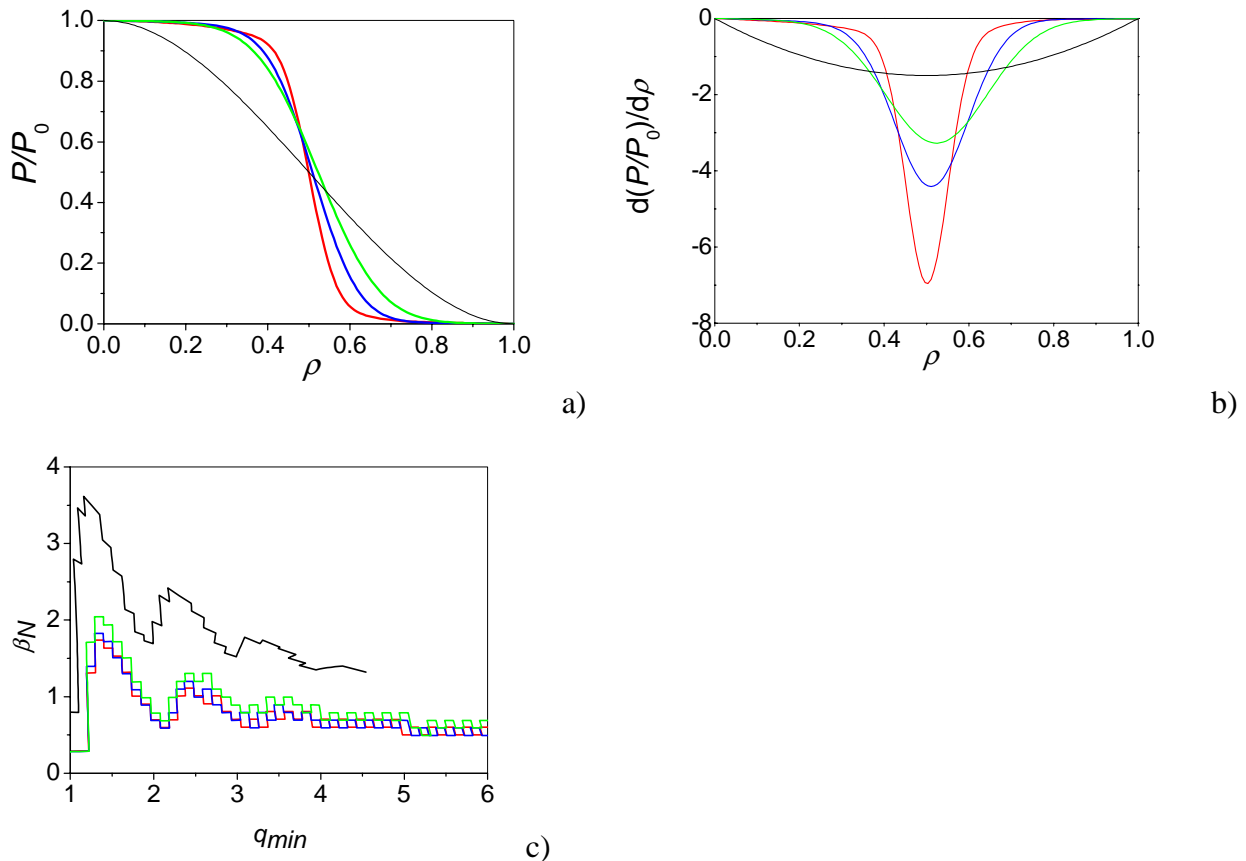

a)

b)

c)

Figure 6.13 Four pressure profiles(a) and corresponding pressure gradients (b) at the low shear region and corresponding stability-instability boundaries in the q_{min} - β_N space (c).

The stability limit in case of the wide "parabolic" pressure profile, reaching the Troyon limit $\beta_N \approx 3.0$, is substantially higher than in the case of eITB profiles. Evidently, the steepness of pressure profiles plays an important role for the infernal mode stability. The formation of eITB, while improving plasma confinement in the core region, leads to an increase of the pressure gradient in the barrier zone near q_{min}, thus lowering the ideal stability limit. This also causes an even higher current density inversion. As a result, the Troyon limit $\beta_N \approx 3.0$ can hardly be obtained in reversed shear plasmas without wall stabilization, unless the possibility to avoid the infernal mode development by profile optimization is found.

The role of pressure profiles and of the type of q profiles can be seen in Figure 6.14. The pressure profiles from Figure 6.13a and the q profiles, presented in Figure 6.14a are of three types: monotonic, flat and reversed.
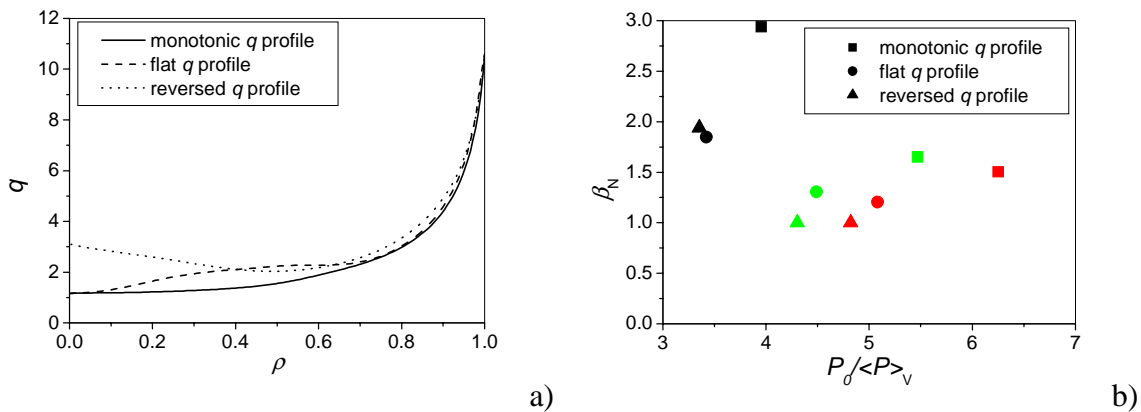

a)   b)

Figure 6.14 a) Different types of q profiles and b) β_N limit dependence on the pressure profile peaking factor for monotonic (squares), flat (circles) and reversed (up triangles) q profiles. Colors correspond to colors of pressure profiles in Figure 6.13a, used for calculations.

The highest ideal stability limit corresponds to the monotonic q profile, while flat and reversed q profiles are more exposed to ideal MHD modes because in the low shear zone the conditions for the infernal mode development appear, especially in case of high pressure gradient or peaked pressure profile. This also explains why fully sustained scenarios with too peaked pressure profile can disrupt even at relatively low β_t values [104, 106].

Another way to see the effect of the localized pressure gradient is in the value of the pressure peaking factor $P_0/\langle P \rangle_V$. It was shown that in reverse shear plasmas this parameter is very important [25], and high β_t values can be obtained only at low peaking values, without wall stabilization. This is also seen in Figure 6.14b where β_N limit almost doubles for the reversed shear case for peaking values between 4.5 and 3. It is interesting to note that this is also the case for a monotonic q profile which has a β_N limit about half the Troyon limit for peaking values greater than 5 (squares in Figure 6.14b). The l_i

variation between the cases in Figure 6.14b are negligible, $l_i \approx 1.3$ in all these cases, thus the l_i variation cannot explain the stability limit changes as equation (5.6) would indicate. This is related to the low shear in the core which gives this sensitivity to the pressure drive, similarly to infernal modes.

6.3.4 The *q* profile

The *q* profiles in the reversed shear plasma can be very different. It is important to define, which parameters of the *q* profiles are important for the mode stability and have to be controlled, and which parameters can be left unattended, because they do not substantially influence the mode stability.

To define the *q* profile parameters, a number of substantially different current profiles were studied at two values of $q_{min} = 2.2$ and 4.4 with different pressure profiles (Figure 6.14). The current profiles were chosen so that a wide range of profile shapes and values of ρ_{qmin}, q_0 and q_a were covered, also at the same ρ_{qmin} different q_0 and q_{min} values were represented.
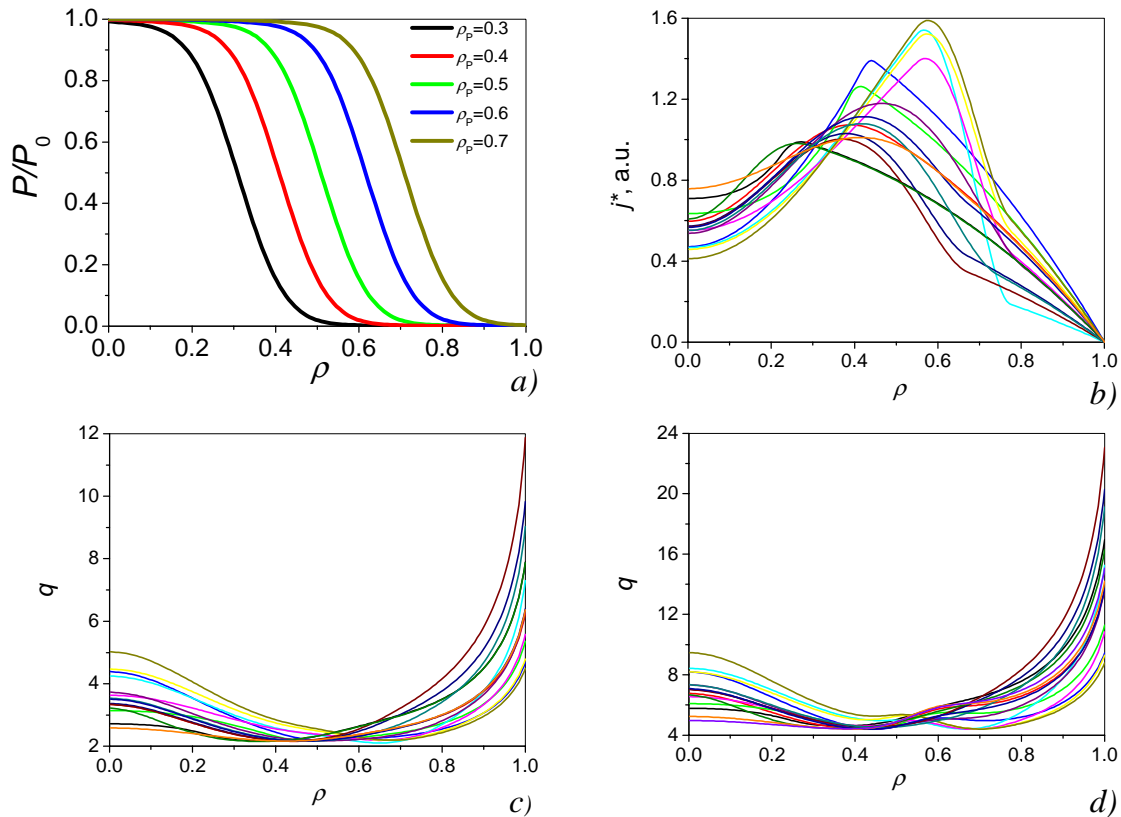
Figure 6.15 a) The pressure and b) the surface averaged current profiles studied for the ideal MHD stability, and corresponding q profiles at c) $q_{min} \approx 2.2$, and d) $q_{min} \approx 4.4$. Note the different scale in c) and d)

The basic parameters of the *q* profiles for the case with $q_{min} \approx 2.2$ varied in the following limits: q_0 between 2.6 and 6.0, q_a between 4.5 and 12. At $q_{min} \approx 4.4$ they varied as follows: q_0 between 4.9 and 9.5, q_a between 8.8 and 23. ρ_{qmin} in both cases varied between 0.35 and 0.66.

Note that in both cases, same plasma current profiles were used, but the corresponding q profiles are different. In some cases at $q_{min} = 4.4$ a second minimum appears in the q profiles.

The pressure profiles, as shown in Figure 6.15a, varied by shifting the pressure gradient zone between $\rho = 0.3$ and 0.6, the position of the gradient zone remained unchanged.

The β_N limit for the pressure and q profiles in Figure 6.15 is presented in Figure 6.16. The dependencies of β_N on ρ, on $\varepsilon_{qmin}/\varepsilon_a$ and on the square root of the volume within the surface of minimum q, relative to the total plasma volume, are shown. In the case of $q_{min} \approx 2.2$ the infernal modes dominate, and at higher $q_{min} \approx 4.4$ the external kink modes are most important.
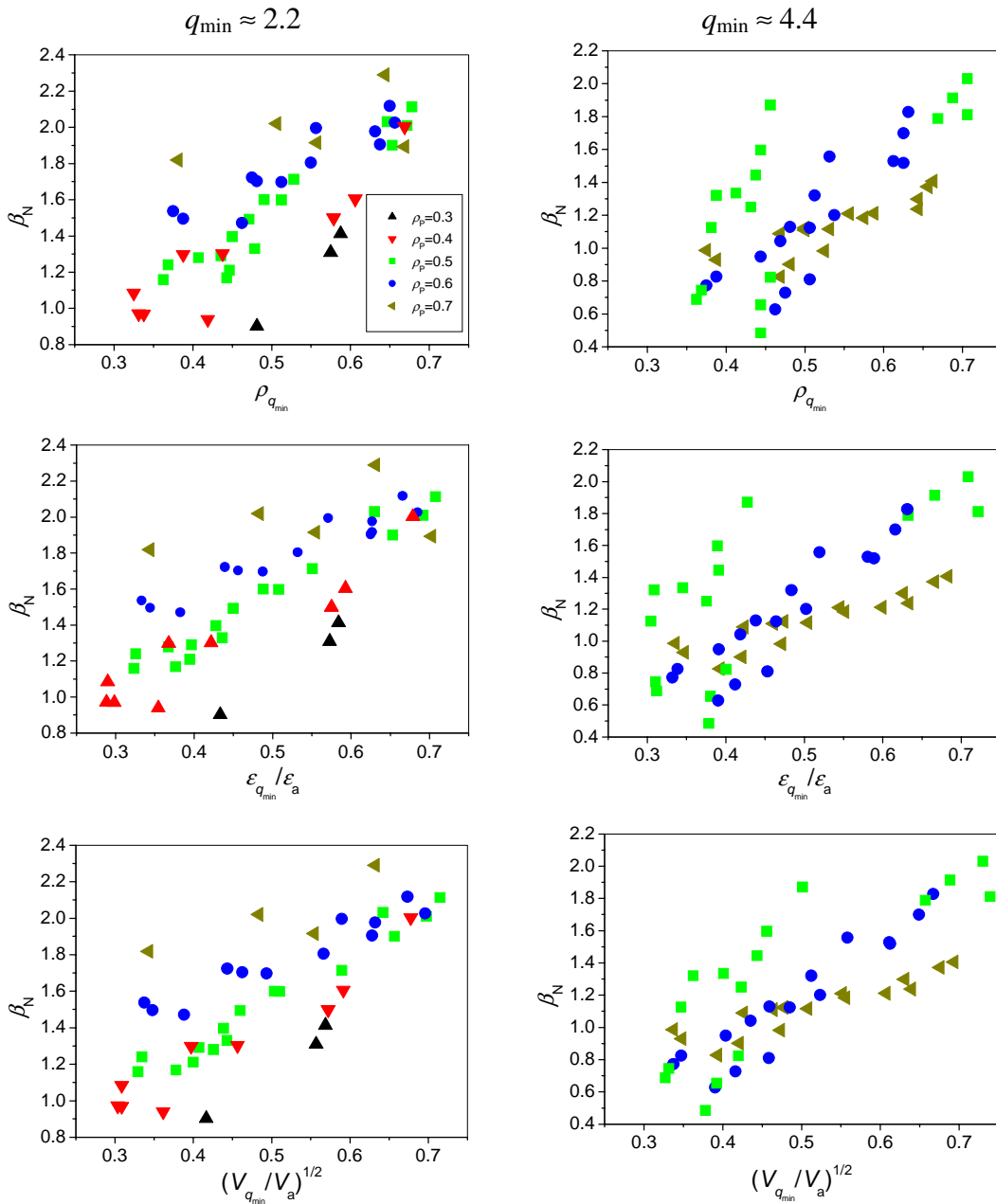

Figure 6.16 The dependence of the β_N limit on ρ, $\varepsilon_{qmin}/\varepsilon_a$ and $\sqrt{V_{q\,min}/V_a}$ at $q_{min} \approx 2.2$ and $q_{min} \approx 4.4$ for different q profiles and pressure profiles , shown in Figure 6.14. The colors correspond to the colors of pressure profiles in Figure 6.14 a.

It is seen in Figure 6.16 that at $q_{min} = 2.2$ and 4.4 the dependence of β_N on $\varepsilon_{qmin}/\varepsilon_a$ and on $\sqrt{V_{q_{min}}/V_a}$ is close to linear. The linear dependence of β_N on $\varepsilon_{qmin}/\varepsilon_a$ and on $\sqrt{V_{q_{min}}/V_a}$ in the case of q profiles with one minimum allows to suppose that the basic parameters that define the infernal mode stability in the reversed shear configuration are the minor radii of q_{min} and of the maximum of P'. On the contrary, q_0, q_{min} and the shape of the q profiles in some limits are not so important for the infernal mode stability. The stability of infernal modes increases with the radius of the pressure gradient and with the radius of the minimum q.
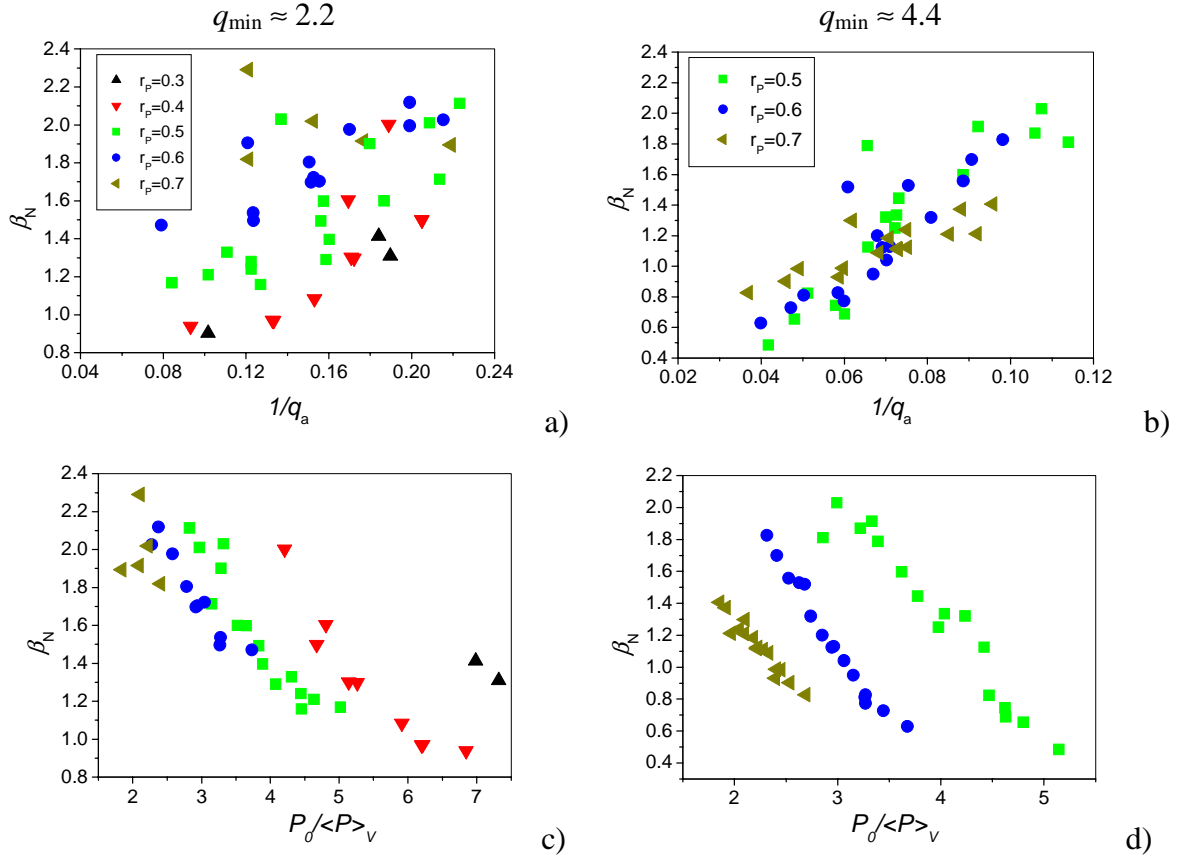

Figure 6.17 The dependence of the ideal MHD stability limit on $1/q_a$ at a) $q_{min} \approx 2.2$. and b) $q_{min} \approx 4.4$, on the pressure peaking factor (c,d)

At $q_{min} \approx 4.4$, when the external kink modes start to dominate, at large radius of pressure gradient the dependence on ρ_{qmin} also appears to be linear. In addition we clearly see in this case an ideal mode stability dependence on $1/q_a$, as shown in Figure 6.17b. At $q_{min} \approx 2.2$ the relation to $1/q_a$ depends more on the radius of the pressure gradient zone ρ_P, thus on the pressure peaking factor (Figure 6.17a,c). The dependence on the plasma pressure peaking factor $P_0/<P>_V$ is linear in both cases (Figure 6.17c,d). Note that the variations of the peaking factor for the same pressure profiles are due to the equilibrium difference at different q profiles. Therefore there is always a link between the q profile and the pressure profile which are difficult to separate.

In order to better understand the apparent dependence of β_N on q_a in Figure 6.17a,b, we show in Figure 6.18 the dependence of β_t on I_N for both of these profiles. We see that in fact we recover the "Troyon curve", except that the β_t limits are slightly lower than $\beta_N \approx 3.0$ because of the high value of the peaking factor and of the reversed shear. The solid symbols ($q_{min} \approx 4.4$), at small I_N, have a quadratic dependence on I_N which explains the linear dependence of β_N on $1/q_a$ in Figure 6.17b. However we see that both groups of profiles are in fact not so different from the normal external kink β limit.
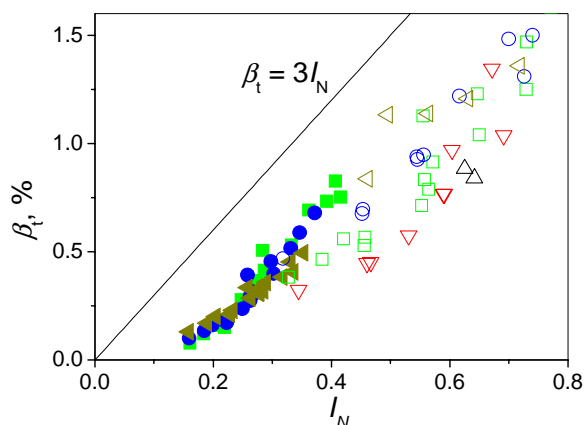

Figure 6.18 The dependence of β_t limit on the normalized current I_N for cases shown in Figures 6.16 and 6.17. Open symbols correspond to $q_{min} = 2.2$, solid symbols correspond to $q_{min} = 4.4$ cases. The Troyon limit $\beta_N = 3.0$ is also shown

6.3.5 The position of q_{min} and of the plasma pressure gradient

The flexible system of EC current drive and plasma heating of TCV allows the creation of a wide range of reversed shear plasma configurations. The current and pressure profiles can be varied substantially and relatively independently. On the basis of the analysis of the stability of plasmas with various current and pressure profiles the configurations with enhanced ideal stability can be proposed for future experiments. Thus, it is important to study the role of the current and pressure profiles and of their combined influence on the ideal stability of such plasmas.

The stability limit behavior in the space q_{min} - β_N was studied for several current profiles, Figure 6.14, and for different pressure profiles with different ρ_{qmin} from Figure 6.14a. The results are presented in Figure 6.19.

In most cases, the calculations started at $q_{min} = 1.5$, because at lower q_{min} the behavior of the stability limit was similar. At q_{min} below 4 to 5 one can see the resonant structure, characteristic of the infernal modes with "stability windows" between the integer values of q_{min}. At higher q_{min} in many cases the stability limit can go up, signifying the stabilization of the infernal mode. This happens mostly at low

ρ_{qmin} and at low ρ_P, whereas at high ρ_{qmin} and/or high ρ_P the external kink mode becomes unstable and the stability limit depends on $1/q_a$ and not on q_{min}. The calculations aborted by β_N increase because of convergence problems, appearing in equilibrium calculations by CHEASE. It is seen in Figure 6.19c,d that at high ρ_{qmin} the mode, localized near the plasma edge, remains unstable at higher q_{min} than at lower ρ_{qmin}, probably because of interaction with the external kink modes. One can also see in Figure 6.17a that at very low ρ_{qmin} and at high ρ_P the external mode dominates the ideal MHD stability, starting from $q_{min} \sim 1.6$. The calculations in the fixed boundary regime have shown that for $\rho_{qmin} = 0.4$ the infernal modes are stable with $\rho_P = 0.6$ and 0.7, that is when there is little pressure gradient in the low shear region.
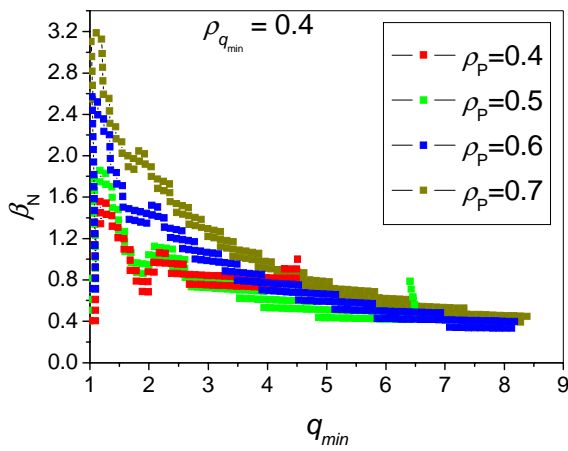
a)
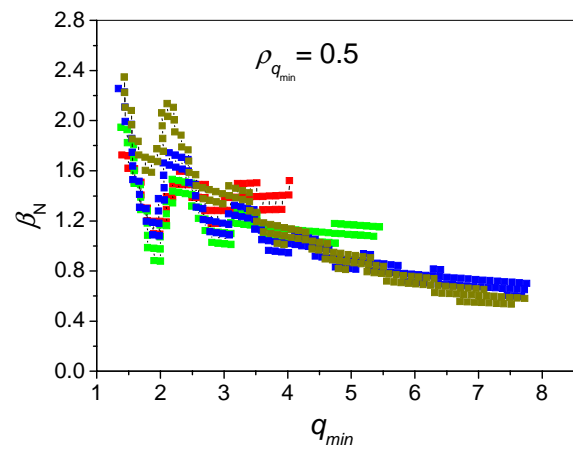
b)
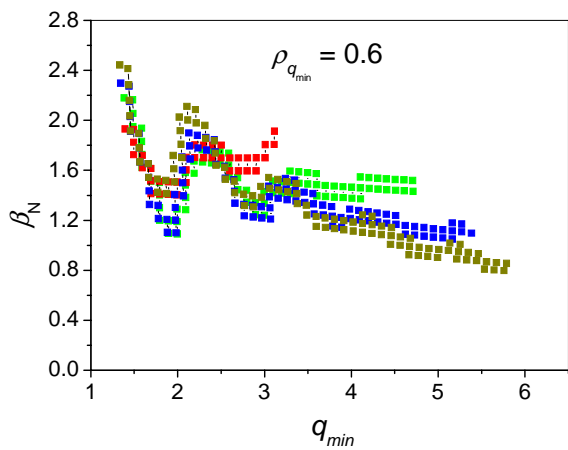
c)

d)

Figure 6.19 The dependence of β_N limit on q_{min} for different q and pressure profiles. Free boundary case.

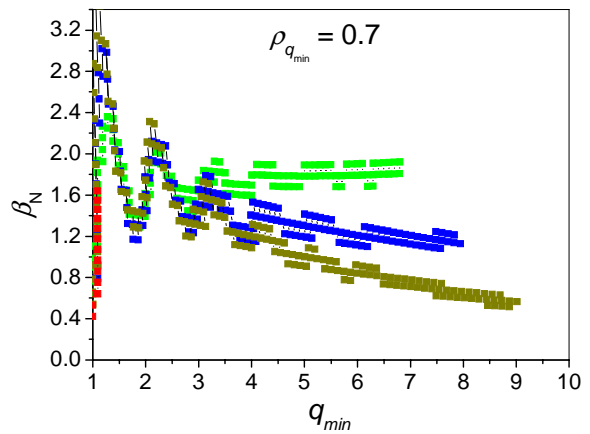These specific features of the ideal MHD modes in the reversed shear plasmas can be used for optimization of the plasma pressure and current profiles in the TCV experiments in order to obtain better plasma performance.

Possible ways of profiles optimization are:

1. q_{min} in "stability windows" close to 1.5, 2.5 or 3.5;

2. The pressure profiles with high radius of ρ_P, flat in the plasma center;

3. Very high (~0.7) or very low (~0.3 - 0.4) radius of q_{min}.

In this case the external kink modes are weak, and the ideal MHD stability is dominated by the infernal modes.

Another way of optimizing the profiles is the high $q_{min} > 6.0$ and moderate or low ρ_{qmin} and ρ_P. In these conditions the infernal mode is stabilized and the external modes are not developed.

Optimization of q and pressure profiles can probably allow to increase β_N, achievable in the TCV reversed shear experiments, to $\beta_N \sim 2.0$, two times higher than the values obtained in described TCV shots.

6.3.6 The $n = 2$ stability

As it was mentioned, in TCV reversed shear experiments the modes with $m/n = 2/1$ and $3/1$ were observed during the plasma disruption. The $n = 1$ modes are considered as the most dangerous ones and the above analysis is devoted to the stability of these modes. It can be useful, however, to consider the stability of modes with higher n, especially with $n = 2$. The $m/n = 3/2$ mode can become unstable at q_{min} close to 1.5, where the "stability window" exists in the case of $n = 1$ mode. The analysis of $n = 2$ mode stability in comparison with $n = 1$ mode is shown in Figure 6.20 for the same conditions as in Figure 6.19a.

The $n = 2$ mode has a resonance at $q_{min} = 1.5$, thus reducing the stability window between $q_{min} = 1$ and 2. Nevertheless, this stability window remains interesting for profiles optimization, because it still allows to reach higher β_N than at q_{min} close to integer values.
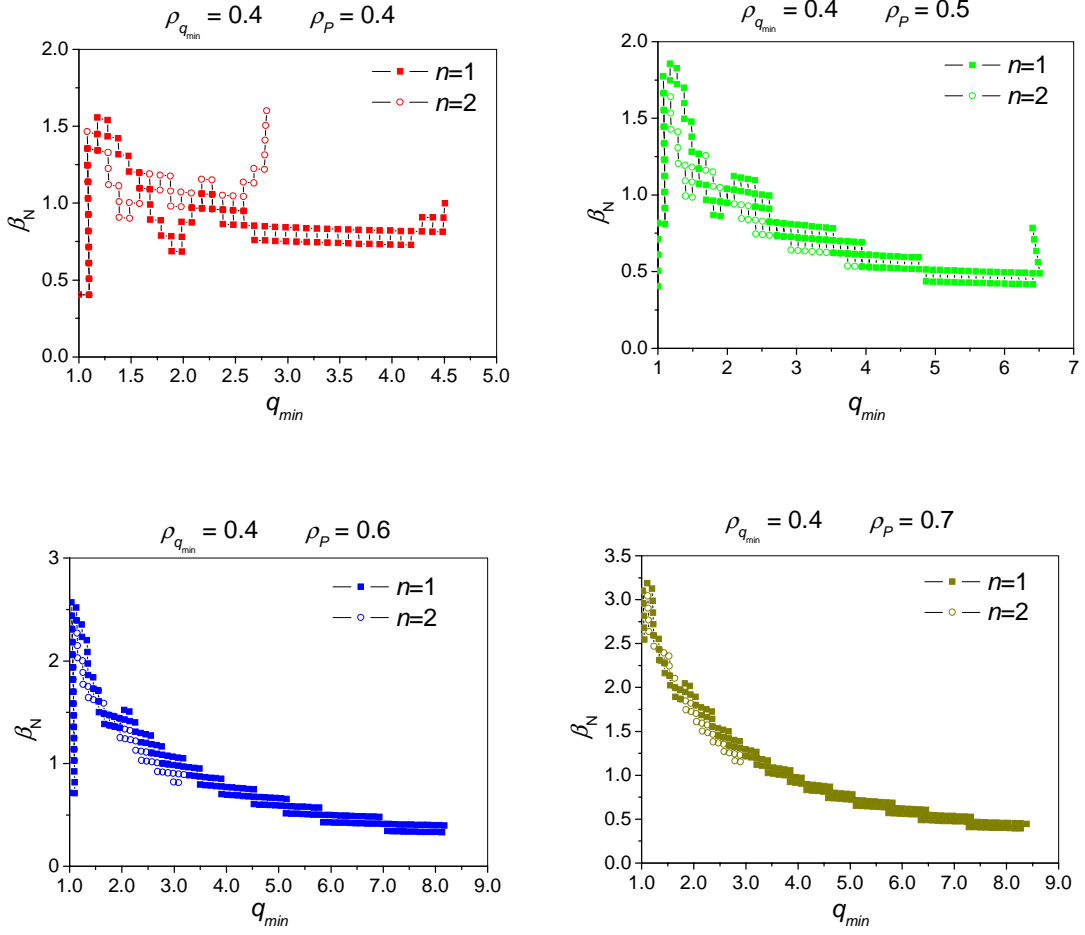
Figure 6.20 The n = 1 (solid squares) and n = 2 (open circles) stability limits at different pressure profiles for the case shown in Figure 6.19a

6.4 Conclusions

- A series of TCV experiments with reversed shear profiles and internal transport barriers have been analyzed. The increase of the current inversion leads to a confinement improvement within the eITB zone and the local pressure gradient increases. The profiles just before the disruption are marginal with respect to the $n = 1$ mode.

- The $m/n = 3/1$ and 2/1 components observed experimentally, are consistent with numerically calculated ideal modes with q_{min} near 3. The characteristic time of the disruption, $\sim$ 20 μs, is consistent with the ideal growth rate. Thus it is shown that reversed shear scenarios with internal transport barrier are limited by ideal modes. The unstable mode is identified as an infernal mode, localized near the q_{min}, low shear region. This mode is mainly pressure driven. The marginal β_N stability limit for the infernal mode is not very sensitive to the presence of an ideal wall on the plasma boundary, but it is very sensitive to integer q_{min} values.

- By increasing the position of the maximum pressure gradient, the mode is localized in the positive shear region and close to the edge. The transition to the external kink mode occurs. It becomes less sensitive to the actual q_{min} value, as expected for external kink modes.

- The β_N limit increases with increasing radius of the position of q_{min} and of the maximum pressure gradient.

- The strong dependence on the pressure peaking factor is confirmed in these reversed shear scenarios. The localized pressure gradient due to the internal transport barrier reduces the β_N limit with respect to the Troyon limit. This is also true for monotonic q profile with similar l_i if $P_0/<P>_V \geq 4\text{-}5$.

- The $n = 2$ mode, although not observed in disruptions of TCV reversed shear plasmas, decreases the β_N limit near the resonance $q_{min} \approx 3/2$, if the position of q_{min} and of the pressure gradient is close to the plasma centre.

- By current and pressure profile optimization it is possible to obtain better plasma performance. Several ways of the profile optimization are proposed.

Chapter 7. Summary and conclusions

Internal kink

- The ideal MHD stability of modern tokamak plasmas has been examined by means of analytical and numerical calculations. The validity limits of the analytical approximations of the internal kink mode growth rate, based on an expansion on the inverted aspect ratio ε, have been analyzed. It has been established that the analytical approach cannot be used in the case of present tight aspect ratio tokamaks, due to the size of ε. This is true even though the value of ε at the $q = 1$ radius, which determines the internal kink growth rate, is significantly smaller than the plasma boundary ε_a. Numerical corrections to inaccuracies, incurred by expansion in ε, are due to the combined treatment of toroidicity and plasma shaping.

- The dependence of the ideal internal kink mode growth rate on the aspect ratio and on plasma shape parameters has been studied in detail, with an emphasis on the effects of elongation and triangularity. It is found in particular that the growth rate has a minimum at slightly negative triangularity, which does not depend on the plasma elongation. The dependence on beta Bussac at moderate and low ε was found to be essentially linear and not quadratic, as predicted analytically. It can even have a dependence on β_{bu}, which is weaker than linear when ε is large

- The critical value of β_{bu}, β_{bu}^{crit} above which the internal kink mode is unstable depends mainly on elongation for $\varepsilon_a \geq 0.2$. It is found that $\beta_{bu}^{crit} = 0$ for $\kappa_a \geq 1.5$. That is, flat pressure profiles inside $q = 1$ are unstable at high elongation. This is in agreement with experimental measurements, which show that pressure profiles are not peaked just before sawtooth crashes when the crash is triggered by an ideal internal kink mode [80].

- Experiments with a variation of plasma triangularity were performed on the TCV tokamak including discharges with very negative triangularity. The experimental dependence of sawtooth oscillations on the plasma triangularity agrees well with the dependence of the numerically obtained results of the ideal internal kink mode growth rate on triangularity. Thus it is consistent with the sawtooth crash being triggered by the ideal internal kink mode in these experiments. The significant stabilization at positive triangularity explains why the resistive internal kink is more relevant for triggering sawtooth crashes in present experiments with $\delta_a > 0.3$.

- On the basis of the numerical calculations a new formula is proposed, describing the dependence of the ideal internal kink mode growth rate on basic plasma parameters. This formula differs substantially from analytical formulae and is intended for the use at moderate and high values of ε, which is characteristic for modern tokamaks. The importance of self-consistent variation of

equilibrium parameters with the variation of each single parameter is highlighted, in particular in order to compare with experimental results.

External kink at high elongation

- The ideal MHD stability analysis of TCV plasmas with high elongation has been performed, using the numerical codes. This work has contributed to the experimental studies of high current plasmas on TCV. The calculations of the $n = 1$ external kink mode stability dependence on plasma shape have been carried out, and the optimum shape found. Some unusual plasma shapes have also been analyzed and possible candidates for experimental studies determined. The results of the experiments on TCV are in good agreement with the ideal stability analysis, which can be used for prediction and optimization of high elongation plasma beta limits.

Reversed shear profiles

- The stability of plasmas with non-monotonic current density profiles have been studied and the role of pressure and current profile parameters was examined. A series of TCV experiments with reversed shear profiles and internal transport barriers have been analyzed. With increasing reversed shear, the confinement is improved and the local pressure gradient increases. It was shown that the profiles just before the disruption were marginal with respect to the $n = 1$ mode.

- The mode structure, with dominant 3/1 and 2/1 components observed experimentally, is consistent with an ideal mode with q_{min} near 3. The characteristic time of the disruption, ~ 20 μs, is consistent with the ideal growth rate. Therefore the study shows that reversed shear scenarios with internal transport barrier are limited by ideal modes. The unstable mode is identified as an infernal mode, localized near q_{min}, low shear region, and is mainly pressure driven. The marginal stability limit for this mode is not very sensitive to the presence of an ideal wall on the plasma boundary. The β_N limit for the infernal mode is very sensitive to integer q_{min} values.

- It has been shown that by increasing the position of the maximum pressure gradient, the mode is localized in the positive shear region and close to the edge. It becomes less sensitive to the actual q_{min} value, as expected for external kink modes.

- It is found that the β_N limit increases with increasing radius of the position of q_{min} and of the maximum pressure gradient.

- The strong dependence on the pressure peaking factor is confirmed in these reversed shear scenarios. It was shown that the localized pressure gradient due to the internal transport barrier reduces the β_N limit with respect to the Troyon limit. It has been shown that this is also true for monotonic q profile with similar l_i if $P_0/<P>_V \geq 4\text{-}5$.

Bibliography

Note: To be distinguished from Dr. Martynov A.A. from Keldysh institute in Moscow, Russia, the name of Andrey Martynov is written as Martynov An. in all publications.

[1] Lawson J. D. (1957) *Proc. Phys. Soc. London, Sec*. B *70,* 6

[2] Aymar R. *et al* (2001) *Nucl. Fusion* **41** 1301-1310

[3] Williams L. P. (1965) *Michael Faraday - A Biography,* Basic Books inc., New York

[4] Grad H. and Rubin H (1958) in *Proceedings of the Second United Nations International Conference on the Peaceful Uses of Atomic Energy*, United Nations, Geneva, Vol. **31**, 190

[5] Shafranov V. D. (1960) *Sov. Phys. – JETP* **26**, 682

[6] Laval G., Mercier C., Pellat R.M. (1965) *Nuclear Fusion* **5**, 156

[7] Bernstein I. B., Frieman E. A., Kruskal M. D., Kurlsrud R. M. (1958) *Proc. R. Soc. London, Ser. A* **244**, 17

[8] Turnbull A.D., Roy A., Sauter O., Troyon F. (1988) *Nuclear Fusion* **28** 1379

[9] F. Porcelli, Boucher D., Rosenbluth M.N. (1996) *Plasma Phys. Control. Fusion* **38,** 2163

[10] Sauter O. et al (2002) *Phys. Rev. Lett*. **88**, 105001

[11] ITER Physics Expert Group on Disruptions, Plasma Control, and MHD (1999) *"ITER Physics Basis, Chapter 3" Nuclear Fusion* **39** 2251

[12] Bussac M. N., Pellat R., Edery D., Soule J. L. (1975) *Phys. Rev. Lett.* **35**, 1638

[13] Wahlberg C. (2004) *Phys. Plasmas* **11**, 2119

[14] Edery D et al. (1976) *Phys. Fluids* **19**, 260

[15] Eriksson H. G. and Wahlberg C. (2002) *Phys. Plasmas* **9**, 1606

[16] Connor J. W. and Hastie R. J. (1985) *The Effect of Plasma Cross Sections on the Ideal Internal Kink Mode in a Tokamak*, Rep. CLM-M-106, Culham Laboratory, Abingdon, OXON

[17] Connor J. W. et al. (2004) *Nuclear Fusion* **44** R1

[18] Wolf R. C. et al, (2003) *Plasma Phys. Contr. Fus.* **45** R1

[19] Henderson M. et al. and Martynov An. (2003) *Phys. Plasmas* **10** 1796

[20] Goodman T. et al. (2003) *Nuclear Fusion* **43** 1619

[21] Henderson M. et al (2005) submitted to *Phys. Rev. Lett.*

[22] Sauter O. et al (2005) *"Inductive current density perturbations to probe electron internal transport barriers in tokamaks"*, accepted to *Phys. Rev. Lett.*

[23] Manickam J., Pomphrey N., Todd A.M.M. (1987) *Nuclear Fusion* **27** 1461

[24] Ozeki T., Azumi M., Tokuda S., Ishida S. (1993) *Nuclear Fusion* **33** 1025

[25] Chu M.S. et al. (1996) *Phys. Rev. Lett*. 77 2710

[26] Freidberg J. P. (1987) *Ideal Magnetohydrodynamics* , Plenum Press, New York and London

[27] Lutjens H. et al. (1996) *Comp. Phys. Comm*. **97,** 219

[28] Soloviev L. S (1968) *Sov. Phys. – JETP* **26**, 400

[29] Berge G., Freidberg J. P. (1975) *Phys. Fluids* **18**, 1362

[30] Grad H. (1973) *Proc. Natl. Acad. Sci. USA* **70**, 3277

[31] Goedbloed J.P. (1975) *Phys.Fluids* **18**, 1258

[32] Goedbloed J.P. (1979) *Lecture Notes on Ideal MHD*, Fom-Institut voor Plasmafysica, Neiwegein, Netherlands

[33] Furth H. P., Killeen J., Rosenbluth M. N., Coppi B. (1964) In *Plasma Physics and Controlled Nuclear Fusion Research* IAEA, Vienna, v. **1**, 103

[34] Greene J. M., Johnson J. L. (1968) *Plasma Phys.* **10**, 729

[35] Rosenbluth M. N., Dagazyan R. Y., Rutherford P. H. (1973) *Phys. Fluids* **11**, 1984

[36] Kruskal M. D., Schwarzschild M. (1954) *Proc. R. Soc. London, Ser. A* **223**, 348

[37] Shafranov V. D. (1956) *At. Energy* **5**, 38

[38] Bondeson A., Bussac M.-N. (1992) *Nuclear Fusion* **32** 513

[39] Krymskii K. M. and Mikhailovskii A. B. (1978) *Fiz. plazmy* **4**, 888.

[40] Lütjens H., Bondeson A. and Vlad G. (1992) *Nuclear Fusion* **32**, 1625

[41] Martynov An. et al, (2004) *submitted to Plasma Phys. Contr. Fus.*

[42] Graves J.P., (1999) *"Kinetic Stabilisation of the Internal Kink Mode for Fusion Plasmas"* PhD thesis, University of Nottingham

[43] Ara G., Basu B., Coppi B. et al. (1978) *Annals of Physics* **112**, 443

[44] Kadomtsev B. B., (1975) *Fiz. Plasmy* **1** 710; *Sov. J. Plasma Phys.* **1** 389

[45] Mirnov S.V. (1969) *Nuclear Fusion* **9**, 57

[45] Connor J.W., Hastie R.J., Taylor J.B (1978) *Physical Rew. Lett.* **40** 396

[46] Connor J.W., Hastie R.J., Taylor J.B (1979) *Proc. R. Soc.* **A365**, 1

[47] Hastie R.J., Taylor J.B (1981) *Nuclear Fusion* **21** 187

[48] Dewar R.L., Manickam J., Grimm R.C., and Chance M.S. (1981) *Nucl. Fusion* **21**, 493; Corrigendum (1981) *Nucl. Fusion* **22**, 307

[49] Philips M.W, Zarnstoff M.C., Manickam J., Levinton F.M., Hudges M.H (1996) *Phys. Plasmas* **3** 1673

[50] Holties H.A., Huysmans G.T.A., Goedbloed J.P., Kerner W., Parail V.V., Soeldner F.X. (1996) *Nuclear Fusion* **36** 973

[51] Connor J.W., Hastie R.J. (2004) *Physical Rew. Lett.* **92** 075001-1

[52] Connor J.W., Hastie R.J. (2004) Phys. of Plasmas **11** 1520

[53] Degtyarev L, Martynov A. A., Medvedev S. et al. (1997) *Comput. Phys. Commun*. **103**, 10

[54] Gruber R, Troyon F, Berger D. et al. (1981) *Comput. Phys. Commun*. **21**, 323

[55] Bernard L.C. et al. (1981) *Comput. Phys. Commun*. **24**, 377

[56] Grimm R.C., Greene J.M., Johnson J. L. (1976) *Methods Comput. Phys*. **9**, 253

[57] Grimm R.C., Dewar R.L., Manickam J. (1983) *J. Comput. Phys* **49**, 94

[58] Glasser A.H. and Chance M.S. (1997) Bull. Am. Phys. Soc. **42**, 1848

[59] Mikhailovskii A.B. et al. (1997) *Plasma Physics Reports* **23**, 844

[60] Ward D.J., Jardin S.C., Cheng C.Z. (1993) *J. Comput. Phys*. **104,** 221

[61] Ward D.J., Bondeson A. (1995) *Phys. Plasmas* **2,** 1570

[62] Gruber R., Cooper W.A., Beniston M. et al. (1991) *Phys. Rep.* **207** 167

[63] Degtyarev L.M., Medvedev S.Yu. (1986) *Comput. Phys. Commun.* **43**, 29

[64] Gruber R. (1978*) J. of Comput. Physics* **26**, 379

[65] Press W.H., Teukolsky S.A., Vetterling W.T. and Flannery (1997) *Numerical recipes in FORTRAN* B.P. Univ. of Cambridge Press, 2nd edition

[66] Noble B., Daniel J.W. (1977) *Applied Linear Algebra* Prentice-Hall, 2nd edition

[67] Ostrowsky A.M. (1959) *Proc. N.A.S.* **45**, 740

[68] Medvedev S.Yu., Villard L., Degtyarev L.M., Martynov A.A., Gruber R. and Troyon F. (1993) *20th EPS Conf. on Controlled Fusion and Plasma Phys., Lisbon, Proc. Contrib. Papers*, **17C**, part IV, 1279

[69] Hofmann F., Tonetti G. (1988) *Nuclear Fusion* **28,** 1871

[70] Martynov An., Sauter O. (2002) *ISPP-20 Theory of Fusion Plasmas, Varenna*, SIF, Bologna, 297

[71] Martynov An., Sauter O. (2000) *ISPP-19 Theory of Fusion Plasmas, Varenna*, SIF, Bologna, 387

[72] Hofmann F., Behn R., Martynov An. et al. (2001) *Plasma Phys. Control. Fusion* **43** A161

[73] Hofmann F., Coda S., Martynov An. et al. (2002) *Nuclear Fusion* **42** 743

[74] Moret J.-M. et al and Martynov An., (2004) *In proceedings of the 20th IAEA Fusion Energy Conference, Portugal (2004): Progress in the understanding and the performance of ECH and plasma shaping on TCV*

[75] von Goeler S., Stodiek W., Sauthoff N. (1974) *Physical Review Letters* **33,** 1201

[76] Itoh K., Itoh S.-I., Fukuyama A. (1997) *Plasma Phys Control. Fusion* **37** 1278

[77] Gimblett C. G., Hastie R.J. (1994) *Plasma Phys. Contr. Fus* **36** 1439

[78] Pochelon A. et al and Martynov An., (2001) *Nucl. Fus.* **41** 1663

[79] Pochelon A. et al and Martynov An., (1999) *Nucl. Fus.* **39** 1807

[80] Reimerdes H. et al and Martynov An. (2000) *Plasma Phys. Control. Fusion* **42** 629

[81] Weisen H. et al and Martynov An., (2002) *Nucl. Fus.* **42** 136

[82] Campbell D.G. et al. (1986) Nucl. Fusion **26**, 1085

[83] Alladio F., Ottaviani M., Vlad G. (1988) *Plasma Phys Control. Fusion* **30** 597

[84] Sauter O., Angioni C. et al. (1998) *ISPP-18 Theory of Fusion Plasmas, Varenna*, SIF, Bologna, 403

[85] Pochelon A. et al. (1999) *Nuclear Fusion* **39**, 1807

[86] Angioni C. et al. (2003) *Nuclear Fusion* **43**, 455

[87] Porcelli F. et al and Martynov An., (2001) *Nucl. Fus.* **41** 1207

[88] Boucher D. et al. (1997) *"Predictive Modeling and Simulations of Energy and Particle Transport in JET", Proc., 16th Int. Conf. Montreal, 1996* (IAEA, Vienna 1997) **2**, 945.

[89] Pereverzev G. et al. (1991) *Report IPP* 5/42

[90] Reimerdes H. (2002) *PhD Thesis*, EPFL

[91] Troyon F. et al. (1984), *Plasma Physics and Controlled Fusion* **26 (1a)** 209

[92] Troyon F. et al. (1988) *Plasma Phys. Control. Fusion* **30** 1597

[93] Hofmann F. et al. (1998) *Nuclear Fusion* **38** 1767

[94] Levinton F. M. et al. (1995) *Phys. Rev. Lett.* **75** 4417

[95] Rice B.W. et al. (1996) *Phys. Plasmas* **3** 1983

[96] Fujita T et al. (1997) *Phys. Rev. Lett* **78** 2377

[97] Soeldner F. X. et al. (1999) *Nucl. Fusion* **39** 407

[98] Moret J. M. et al and Martynov An., (2002) *Plasma Phys. Contr. Fus.* **44** B85

[99] Henderson M. A. et al and Martynov An., (2004) *Plasma Phys. Contr. Fus.* **46** A275

[100] Sauter O. et al and Martynov An., (2005) *Phys. Rev. Lett.* **94**, (2005) 105002

[101] Coda S. et al and Martynov An., *to be published in Phys. Plasmas,* May, **2005**

[102] Sauter O. et al. (2002) *29th EPS Conference Montreux (Switzerland), June 17-21 2002,* poster P-2.087 http://crppwww/conferences/EPS02/os_paper.pdf

[103] Coda S. et al (2005) submitted to *Phys. Plasmas*

[104] Sauter O. et al and Martynov An., (2000) *Phys. Rev. Lett.* **84** 3322

[105] Coda S. et al and Martynov An., (2000) *Plasma Phys. Contr. Fus* **42** B311

[106] Sauter O. et al and Martynov An., (2001) *Phys. Plasmas* **8** 2199

[107] Weisen H. et al and Martynov An., (2001) *Nucl. Fus.* **41** 1459

[108] Rebut P. H. et al. (1989), *Proc. 12th IAEA conf., Nice 1988*, IAEA, Vienna, **12** 191

[109] Nikkola P., Sauter O., et al. (2003) *Nucl. Fusion* **43** 1343

[110] Nikkola P. (2004) *PhD thesis* LPR 793/04 CRPP EPFL

[111] Harwey R.W., McCoy M.G. (1992) *Proc. IAEA/TCM/Advances in Simulation and Modeling in Thermonuclear Plasmas* (Montreal 1992)

[112] Scarabosio A., private communication

[113] Fable E., Sauter O. (2004) *ISPP-21 Theory of Fusion Plasmas, Varenna*, SIF, Bologna, 443

[114] Zhuang G., Scarabosio A. et al. (2004) *31th EPS Conference London (United Kingdom), June-July 2004,* poster P2-143; CRPP preprint LPR 795/04 67

Acknowledgements

I am grateful to all people who have helped me during the work on the present thesis.

Firstly, to Dr. Olivier Sauter, my thesis supervisor, who guided me during these years and supported me in numerous difficult situations. His extremely effective way of working, his motivation for research work and especially his endless patience will be for me an example to imitate and to follow in my further activity.

I would like to thank Dr. John Graves, whose assistance in the elaboration of theoretical aspects of the work can not be overvalued.

My sincere gratitude to Dr. Antoine Pochelon, who supported and encouraged me in my first contacts with CRPP and during all these years.

I thank Prof. C. Wahlberg, Prof. T. Schietinger, Dr. H. Lutjens and Dr. J. Graves for their kind agreement to examine this work as experts and jury members and to Prof. V. Savona, the jury President.

It was a pleasure for me to work in the hearty atmosphere of CRPP, so I thank all CRPP members and its direction for excellent working conditions, created there.

My stay in Switzerland could end in a different, rather mournful way, if not the brilliant work of Dr. A.P. Fischer from Centre Hospitalier Universitaire Vaudois in Lausanne, who has performed the cardiosurgery in September 2004, having completely eliminated the serious heart disease, discovered by occasion a few months earlier.

And, of course, I must express my sincere gratefulness to my wife Tatiana for her love and patience and to my son Dmitry, who came into being in May 2002 and who infinitely enriches our life since that time.

Curriculum vitae

Andrey MARTYNOV

Born in Moscow, Russia the 7th of November 1972.

1979-1989	Elementary, then secondary schools n° 52 and n° 999 in Moscow, Russia. Graduated from the secondary school n° 999 of the city of Moscow with the secondary education certificate.
1989-1995	Moscow Engineering and Physics Institute (Technical University), Moscow, Russia. Graduated with the diploma of engineer-physicist with specialization in nuclear physics.
1995-1999	Russian Research Center "Kurchatov Institute" Moscow, Russia Engineer, Institute of Nuclear Fusion.
1999-2005	Swiss Federal Institute of Technology in Lausanne (EPFL). Assistant-doctorant, Center of Plasma Physics Researches (CRPP)

List of publications

Martynov An., Graves J., Sauter O. *" The stability of the ideal internal kink mode in realistic tokamak geometry"* submitted to *Plasma Phys. Contr. Fusion*

Sauter O. et al and Martynov An., (2005) *Phys. Rev. Lett.* **94**, (2005) 105002

Coda S. et al and Martynov An., *to be published in Phys. Plasmas,* May, **2005**

Henderson M. A. et al and Martynov An., (2004) *Plasma Phys. Contr. Fus.* **46** A275

Moret J.-M. et al and Martynov An., (2004) *In proceedings of the 20th IAEA Fusion Energy Conference, Portugal (2004): Progress in the understanding and the performance of ECH and plasma shaping on TCV*

Henderson M. et al. and Martynov An. (2003) *Phys. Plasmas* **10** 1796

Martynov An., Sauter O. (2002) *ISPP-20 Theory of Fusion Plasmas, Varenna*, SIF, Bologna, 297

Hofmann F., Coda S., Martynov An. et al. (2002) *Nuclear Fusion* **42** 743

Weisen H. et al and Martynov An., (2002) *Nucl. Fus.* **42** 136

Porcelli F. et al and Martynov An., (2001) *Nucl. Fus.* **41** 1207

Pochelon A. et al and Martynov An., (2001) *Nucl. Fus.* **41** 1663

Sauter O. et al and Martynov An., (2001) *Phys. Plasmas* **8** 2199

Weisen H. et al and Martynov An., (2001) *Nucl. Fus.* **41** 1459

Hofmann F., Behn R., Martynov An. et al. (2001) *Plasma Phys. Control. Fusion* **43** A161

Martynov An., Sauter O. (2000) *ISPP-19 Theory of Fusion Plasmas, Varenna*, SIF, Bologna, 387

Sauter O. et al and Martynov An., (2000) *Phys. Rev. Lett.* **84** 3322

Coda S. et al and Martynov An., (2000) *Plasma Phys. Contr. Fus* **42** B311

Reimerdes H. et al and Martynov An. (2000) *Plasma Phys. Control. Fusion* **42** 629

Alikaev V.V. et al and Martynov an. (2000) *Plasma Physics Reports* **26** 177

Pochelon A. et al and Martynov An., (1999) *Nucl. Fus.* **39** 1807

Alikaev et al and Martynov An. (1998) *25th EPS Conference, Prague (Czech Republic), June 29 – July 3 1998,* poster P2.088; http://epsppd.epfl.ch/Praha/WEB/98ICPP_W/E083PR.PDF

Esipchuk Yu.V., Kirneva N.A, Martynov An., Trukhin V.M. (1995) *Plasma Physics Reports* **21** 543